# Dissertation

submitted to the
Combined Faculties for the Natural Sciences and for Mathematics
of the Ruprecht-Karls University of Heidelberg, Germany
for the degree of
Doctor of Natural Sciences

presented by

**MSc. Xinyu Cao**

**born in Hebei, China**

Oral examination: Oct 17, 2008

# Antifouling Properties of Smooth and Structured Polyelectrolyte Thin Films

Referees

**Prof. Dr. Michael Grunze**

**Prof. Dr. Motomu Tanaka**

## Abstract

The goal of this thesis is the development of smooth and structured polyelectrolyte surfaces and to correlate the surface properties with their antifouling performance. Strategies in antifouling are focused on two aspects: surface chemistry and surface topography. Therefore, two types of surfaces, polysaccharide coatings with different chemistries and poly(acrylic acid)/polyethylenimine multilayers with different topographies, have been studied in this thesis.

Three polysaccharides, hyaluronic acid (HA), alginic acid (AA) and pectic acid (PA), were covalently coupled on glass or silicon surfaces. The results of protein adsorption tests on these coatings indicate that surface charge, molecular conformation and reaction with calcium play important roles in the interactions between polysaccharides and proteins. The settlements of bacteria (*Pseudomonas fluorescens*, *Vibrio alginolyticus*, *Cobetia marina* and *Marinobacter hydrocarbonoclasticus*), algae (*Navicula perminuta* and *Ulva linza*) and invertebrate cyprids (*Balanus amphitrite*) on polysaccharide coatings reveal that surface properties such as wettability, swelling in water and interactions with ions have great influence on biofouling.

Polyelectrolyte multilayers were applied to study the effect of topography on marine biofouling. These multilayers were constructed by the deposition of the oppositely charged polyelectrolytes, poly(acrylic acid) (PAA) and polyethylenimine (PEI) through a layer-by-layer spray coating method. Hierarchical surface structures with different texture sizes and roughnesses were obtained by adjusting the pH of the polyelectrolyte solutions. Settlement of Ulva spores and barnacle cyprids was remarkably reduced by the multilayers with large texture size and high roughness. The effect of topography on biofouling is related to the attachment points between the surface and the fouling organisms.

Surface modifications on polyelectrolyte multilayers with fluorinated silane and poly(ethylene glycol) (PEG) combined topography and chemistry. The antifouling performance of modified multilayers was determined by both the topography of the multilayer film and the chemistry of the surface.

Several techniques were applied to analyze the surface properties of the coatings, including contact angle measurement, spectral ellipsometry, X-ray photoelectron spectroscopy (XPS), scanning electron microscopy (SEM) and atomic force microscopy (AFM).

## Zusammenfassung

Das Ziel dieser Arbeit ist die Entwicklung glatter und strukturierter Polyelektrolyt-Oberflächen zur Erforschung der Korrelation von Oberflächeneigenschaften und Antifouling Potential. Strategien in Antifouling wurden auf zwei Aspekte konzentriertet: Oberflächenchemie und Oberflächentopographie. Deshalb wurden in dieser Arbeit zwei Oberflächenarten, Polysaccharidschichten mit unterschiedlicher Oberflächenchemie und Polyacrylicsäure/Polyethylenimin Multilagen mit verschiedenen Topographien, untersucht.

Drei Polysaccharide, Hyaluronsäure, Alginsäure und Pectinsäure, wurden kovalent an Glas beziehungsweise Silizium gebunden. Die Ergebnisse von Proteinadsoptionstests mit diesen Oberflächen zeigen, dass die Oberflächenladung, die molekulare Konformation sowie Reaktionen mit Kalzium eine wichtige Rolle für die Wechselwirkungen zwischen Polysacchariden und Proteinen spielen. Die Anlagerung von Bakterien (*Pseudomonas fluorescens*, *Vibrio alginolyticus*, *Cobetia marina* und *Marinobacter hydrocarbonoclasticus*), Algen (*Navicula perminuta* und *Ulva linza*) und Larven von Wirbellosen (*Balanus amphitrite*) auf den Polysaccharidbeschichtungen hat gezeigt, dass Oberflächeneigenschaften wie Benetzbarkeit, Quellverhalten in Wasser und Wechselwirkungen mit Ionen großen Einfluss auf das Biofouling haben.

Um die Effekte der Oberflächentopographie zu untersuchen, wurden Polyelektrolytmultischichten angewendet. Diese Multischichten wurden durch eine layer-by-layer Anlagerung der gegensätzlich geladenen Polyelektrolyte Polyacrylsäure und Polyethylenimin mittels Sprühbeschichtung hergestellt. Hierarchische Oberflächenstrukturen mit unterschiedlichen Texturgrößen und Rauhigkeiten konnten durch die Einstellung des pH-Wertes der Elektrolytlösungen erhalten werden. Eine bemerkenswerte Verringerung der Anlagerung von Sporen der Alge Ulva und von Seepockenlarven zeigte sich auf den Multischichten mit großen Oberflächenstrukturen und hoher Rauhigkeit. Die Auswirkung der Topographie auf das Biofouling steht in engem Zusammenhang mit den Kontaktpunkten zwischen Oberfläche und anhaftenden Meeresorganismen.

Durch chemische Modifizierung von Polyelektrolytmultischichten mit Fluor-Silan und Polyethylenglykol (PEG) wurden Oberflächenchemie und Topographie kombiniert. Die Antifouling-Eigenschaften der modifizierten Oberflächen wurden dabei sowohl von Chemie als auch Topographie der Oberfläche beeinflusst.

Zur Bestimmung der Oberflächeneigenschaften der Schichten wurden verschiedenste Techniken angewendet, unter anderem Kontaktwinkelmessungen, spektrale Ellipsometrie, Röntgen-Photoelektronenspektroskopie, Rasterelektronenmikroskopie und Rasterkraftmikroskopie.

# Contents

# Chapter 1

# Introduction

The phenomena of biological adhesion can be found at the microscopic level in processes such as protein adsorption, bacteria and cell attachment, but also on the macroscopic level with settlement of algae and invertebrates. The adhesion is very important in the life-cycle of some organisms. But on the other hand, uncontrolled adhesion on man-made surfaces can have adverse consequences. For example, adsorption of proteins and attachment of cells onto medical implant surfaces may cause detrimental clinical complications, an increased risk of infection and poor device performance [1]. Also, settlement of algae and invertebrates increases the roughness of ships' hulls, which in turn leads to a higher hydrodynamic drag as the vessel moves through water [2]. This biofouling problem generates large economic costs due to increased fuel consumption, hull cleaning, paint removal and repainting [2]. It is estimated that the world fleet consumes an additional 300 million tons of fuel annually as a result of hull fouling [3]. Therefore, the control of unwanted biological adhesions is an interesting topic and also a challenging task in the fields of surface chemistry, nanotechnology and biomaterials.

The traditional technique to minimize or prevent biofouling was to use paints with toxic constituents or biocides to kill colonizing organisms [4]. But due to the diffusion of these toxic components from the paints into the ocean, marine environment has been adversely polluted. Therefore, environmentally friendly antifouling coatings have to be developed.

The work presented in this thesis is funded by the integrated european project AMBIO ('Advanced Nanostructured Surfaces for the Control of Biofouling'). This project combines surface chemistry and marine biology, environment and nanotechnology, and is devoted to the knowledge-based development of antifouling coatings that function through their nano- and microscale physico-chemical properties and which do not involve the release of biocides damageable for the environment [2].

Two types of surface coatings, surface grafted polysaccharides and polyelectrolyte

multilayers, were studied in this work to find the correlations between surface properties and biological adhesion, especially with regard to the settlement of marine organisms. Contact angle measurement, spectral ellipsometry, X-ray photoelectron spectroscopy (XPS), scanning electron microscopy (SEM), and atomic force microscopy (AFM), were applied to qualitatively and quantitatively analyze the surface properties of the coatings.

Polysaccharide coatings which are covalently coupled on the surface have been found to markedly reduce the adhesion of cells and bacteria [5, 6]. It is interesting to investigate whether these anti-adhesive properties of polysaccharide coatings in medical application can be transferred to the marine environment. In this work, three polysaccharide coatings, hyaluronic acid (HA), alginic acid (AA) and pectic acid (PA), were prepared. Their performances in protein adsorption, cell adhesion and settlement of marine organisms were tested and the results are discussed based on their surface properties, such as wettability, molecular conformation and interactions with ions.

The unique micro-structures on the lotus leaf and the corresponding self-cleaning phenomenon have inspired many scientific researches on surface topography [7]. Recent studies have demonstrated that topography has strong influences on biological adhesion [8, 9, 10, 11]. In this work, polyelectrolyte multilayers with nano- and microscale hierarchical surface structures were constructed by the newly developed layer-by-layer spray coating method. Many parameters were considered to control the morphology such as the feature size, film roughness and thickness. These structured polyelectrolyte films were further chemically modified to tailor their surface chemistry. Marine organisms settlement assays were performed on these surfaces to study the effects of surface topography and surface chemistry.

# Chapter 2

# Biofouling Background

## 2.1 Biofouling

All man-made structures in marine and freshwater environments suffer from the problem of biofouling, which is the unwanted aggregation of microorganisms (bacteria), plants (algae) and invertebrate animals on the surfaces. When a surface is immersed in freshwater or seawater within a few minutes, it becomes 'conditioned' through the adsorption of macromolecules (e. g. proteins and tannins) [2]. Bacteria, many unicellular algae, protozoa and fungi adhere to the surface within hours. These early attached microorganisms aggregate together and form a biofilm, which is often referred to as *microfouling* or *slime* [2]. The settlement of larger algae and invertebrates on artificial surfaces is usually named as *macrofouling*. Figure 2.1 shows a submarine hull heavily fouled by green seaweed *Ulva linza* [2].

Figure 2.1: Example of biofouling of surfaces with the unwanted growth of the green algae *Ulva linza* on a submarine hull [2].

In the AMBIO project, the selection of the test fouling organisms is based on two

requirements. First, they must represent the major fouling groups including microfoulers (comprising bacteria and microscopic unicellular algae), soft macrofoulers (e. g. macroalgae, anemones and hydroids), and hard macrofoulers (e. g. barnacles, mussels and tubeworms) [3]. Second, the chosen organsims must represent a range of colonization and adhesion strategies and a range of length scales [3].

Based on these requirements, a freshwater bacterium (*Pseudomonas fluorescens*), three marine bacteria (*Vibrio alginolyticus*, *Cobetia marina* and *Marinobacter hydrocarbonoclasticus*) and diatom (*Navicula perminuta*) are chosen as representatives for microfoulers. Soft macrofouler is represented by macroalga (*Ulva linza*) and hard macrofouler is represented by barnacles (*Balanus amphitrite*). Some useful information about these organisms and their adhesion behaviors are shortly introduced in the following sections.

### 2.1.1 General Properties of Biological Adhesives

Marine organisms attach to the surfaces through the secretion of polymeric adhesives. The adhesives have remarkable properties to enable the organisms rapidly and firmly attach to the surfaces. In the first step of settlement, an adhesive must be discharged quickly from the attaching organism in order to secure the propagule [12]. In order to spread over to 'wet' the surface, the adhesive must be a fluid in the initial phase, and it must be insoluble in water. Having wet the surface, the adhesive must bond to that surface in a process that must involve the exclusion of water molecules [12]. Finally, the adhesive must 'cure' quickly to achieve a cohesive strength sufficient to bond the organisms under turbulent conditions [12].

### 2.1.2 Bacterial Biofilms

Bacteria are widely existed in natural environments and colonize the submersed surfaces by forming dense, slimy biofilms. Bacteria are transported toward the substrate through diffusion, convection, sedimentation, or by their intrinsic motility [13]. Most bacteria can move along chemical gradients due to their chemo-receptors.

After the reversible initial attachment phase, the bacteria become strongly and irreversibly attached to the surface through the production and secretion of extracellular polymeric substances (EPS) [14]. Growth of the established biofilm involves the division of adhered cells, continuous EPS production, and settlement of new bacterial cells.

The contents of EPS secreted by bacteria include water and many kinds of macromolecules such as polysaccharides, proteins, humic substances, nucleic acids and lipids. The adhesion of bacteria is based on the hydrophobic and electrostatic interactions between the carbohydrate and protein components in the EPS and the

substrate [15]. The amount of EPS produced can exceed the mass of the bacterial cell by a factor of 100 or more [16]. The rate of the fouling process, the composition of the biofilm and the adhesion strength are strongly influenced by the physical and chemical characteristics of the surface.

Bacterial biofouling occurs within a few minutes up to several hours. Due to the complexity of the mixed bacterial biofilms with different species, they are often difficult to remove from the surface [17].

### 2.1.3 Algae Adhesion

**Unicellular Algae Diatom: *Navicula perminuta***

Diatoms such as *Navicula perminuta* are unicellular brown algae with complicated silica cell walls composed of two overlapping halves or 'valves' (Figure 2.2A)[1]. Diatoms are classified as centric (radial) or pennate (bilateral) by their valve symmetry. The centric forms are mostly planktonic, whereas the pennate forms are mostly benthic and capable of attachment and motility on natural or artificial substrates [18].

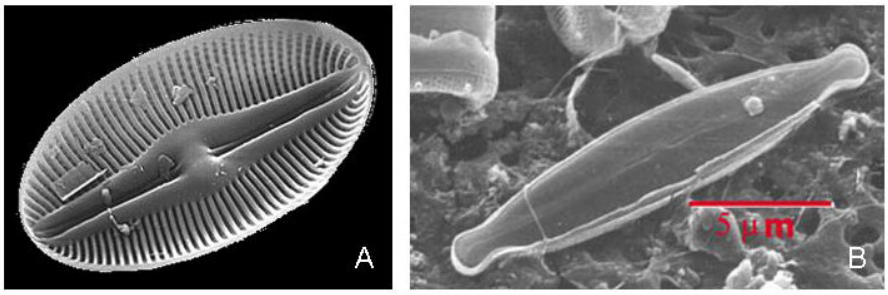


Figure 2.2: SEM images of diatom *Navicula perminuta* (A)[1] and a settled *Navicula perminuta* on a surface (B)[2].

Diatoms are the most common microalgal foulers of the submerged artificial structures through the formation of biofilms. Diatom cells are passively carried to surfaces by the action of water movement and currents or by settling under gravity [18]. They may search the surface through the actin filaments inside the cell membrane or remain stationary for an extended period [19, 20, 21].

For both motile and sessile adhesion strategies, cell-substratum adhesion is mediated by the secretion of sticky EPS [19, 22] through one or two slits in the silica cell wall called raphes (Figure 2.2A), which are in contact with the substratum (Figure 2.2B)[2] [20, 23]. Adhesion of raphid diatoms is also strongly influenced by surface wettability and friction [24, 25, 26].

[1] Picture taken from http://www.chemistry.lakeheadu.ca/personal/kinrade/diatdip.gif.
[2] Picture taken from http://hypnea.botany.uwc.ac.za/phylogeny/groworg/images/Navicula1_SEM.jpg.

Diatom EPS are complex, multi-component materials mostly dominated by carbohydrates and proteins [22]. Further studies on the EPS chemistry of unicellular diatoms [27, 28] indicate that the carbohydrates constitute complex, anionic polysaccharides with heterogeneous monosaccharide compositions, sulfate ester and uronic acid. The composition and properties of the adhesives vary not only between diatom species but also at different sites of the same diatom cell [18].

Division of attached diatom cells rapidly gives rise to colonies that eventually associate to form a compact biofilm that may achieve a thickness of up to 500 $\mu$m [2]. Although slime may appear insignificant compared to macrofouling, the increase in surface roughness still imposes a substantial hydrodynamic drag [17].

**Macro Algae: *Ulva linza***

The green seaweed *Ulva linza* is the slippery grass-like plant that can be found on the surface of rocks at the seashores. It is the major macroalgal fouler of ships and other man-made structures in marine environment [17]. Ulva reproduces by the production of large amount of microscopic, 'naked'(i.e. without a cell wall) zoospores, 5-7 $\mu$m in length, which swim through the water using four flagella (as shown in Figure 2.3A).

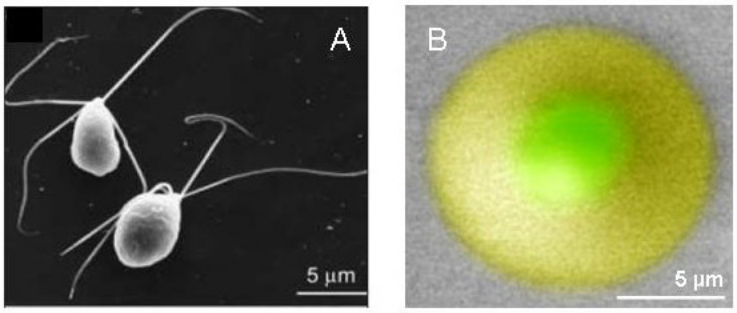


Figure 2.3: SEM image of zoospores of *Ulva linza* (A) and false color environmental-SEM image of a settled *Ulva linza* spore (B) [12].

In order to complete their life cycle, the zoospores need to locate a surface, settle on it and then firmly adhere to it. Having located a suitable surface, the zoospore undergoes 'settlement' and permanent attachment, involving loss of motility and the four flagella, secretion of adhesive which anchors the spore to the substrate, and the production of a new cell wall (as shown in Figure 2.4) [12, 18]. The adhesive secreted by Ulva spores is a polydisperse, self-aggregating hydrophilic glycoprotein, resembling the group of hydroxyproline-rich extracellular matrices of both plants and animals [18]. The adhesive is already present in the swimming spore inside membrane-bound vesicles. On discharge, it swells around 300 times and forms a pad around the spore (as shown in Figure 2.3B) and starts to 'cure' immediately to

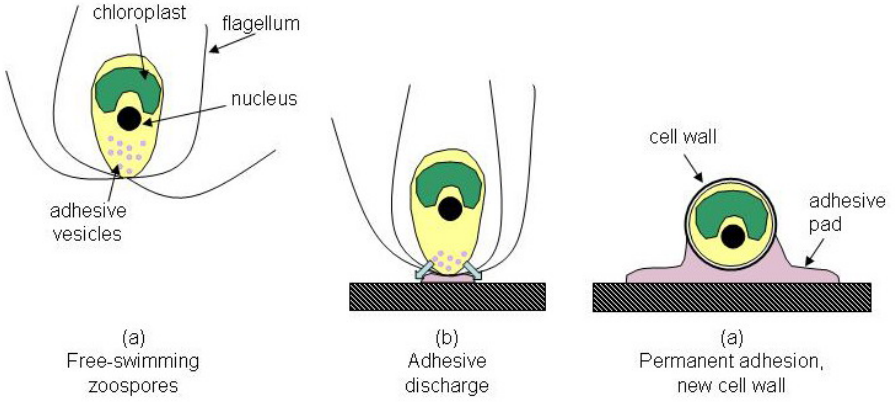


Figure 2.4: The steps involved in the settlement and adhesion of *Ulva* spores [12].

firmly fix the spore on the surface [12].

Spores germination occurs within a few hours, then cell division and growth give rise to sporelings (young plants) that are also firmly attached to the substratum through adhesive secreted by rhizoids (rootlets) [12].

Settlement is selective, swimming zoospores respond to a range of chemical, physical, topographic and biological cues [10, 29, 30]. Once settled, the adhesion of the attached spores is also influenced strongly by wettability and surface friction [24, 25].

### 2.1.4 Invertebrates: Barnacle *Balanus amphitrite*

The tropical/semitropical barnacle, *Balanus amphitrite*, is a major macrofouler of ships and other immersed artificial surfaces in marine environment (Figure 2.5A)[3]. The attachment strength of barnacles is remarkably high. Once attached, neither the juvenile nor the adult barnacle moves or self-detaches [31].

There are three attachment stages in the barnacle life cycle. First, barnacle cyprid larva explores a surface by 'walking' with its paired antennules (Figure 2.5B) and secrets mucous material from the tips of the antennules for temporary attachment [17]. When a larva has located a suitable place for settlement, it secrets cyprid cement to embed the attachment organs to the substrata [17]. This event is commonly regarded as marking the onset of metamorphosis to the juvenile barnacle. The cyprid cement fixes the juvenile to the surface until finally the adult cement apparatus begins to produce cement for permanent fixation (Figure 2.5C)[4] [17, 31].

[3]Picture taken from http://www.ambio.bham.ac.uk/images/text%20images/barnacle2.jpg.
[4]Picture taken from http://www.roulletdivingservices.com/yahoo_site_admin/assets/images/barnacles.jpg.

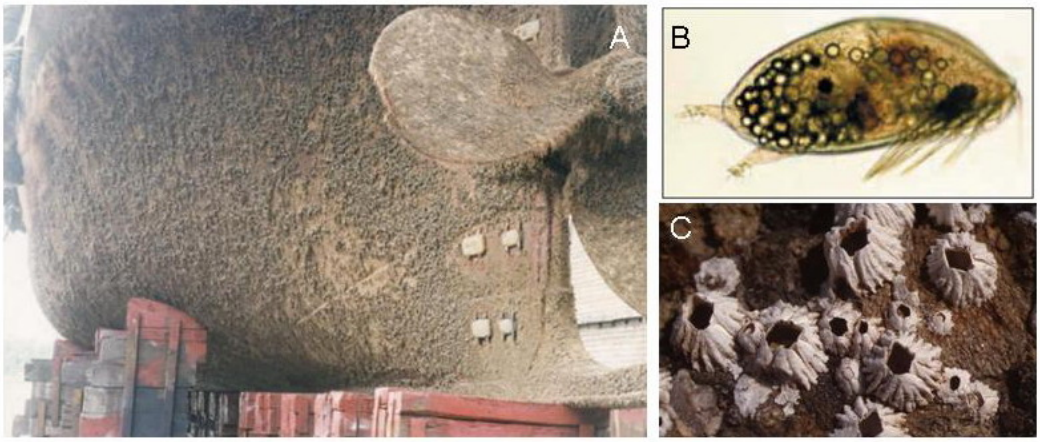


Figure 2.5: Ship hull showing extensive fouling by barnacles (A)[3]; the cyprid larva of barnacle (B) [2] ; adult barnacles on a fouled surface (C)[4].

## 2.2 Antifouling

Marine biofouling results in great operational and maintenance costs, therefore effective antifoulants capable of preventing the settlement and growth of marine organisms are required. Biofouling has been controlled traditionally through the use of antifouling paints with toxic constituents or biocides [4]. As a result, important levels of contamination have been observed in the aquatic environment worldwide, especially in coastal areas and harbors [32]. Therefore, toxic constituents, such as tributyltin (TBT), have already been banned for use in antifoulants by the International Maritime Organization (IMO) and Marine Environment Protection Committee (MEPC). The use of biocides in antifouling paints is also highly restricted [32].

The economic costs of fouling and stricter global regulations on the use of biocidal antifouling paints have led to an increasing demand for environmentally benign solutions to fouling control over the last few years. Research has focused on surfaces that minimize settlement and/or adhesion of fouling organisms. However, in order to design effective coatings, it is essential to understand which properties of surfaces directly influence settlement and adhesion in the colonizing stages of these organisms [2, 7]. Numerous studies about the adhesion of the marine organisms mentioned in section 2.1 have already proved that the interactions between surfaces and organisms are greatly influenced by surface properties, such as wettability, molecular conformation, surface charge, topography and roughness.

Due to their chemical and physical properties, polysaccharide surfaces and polyelectrolyte multilayers were studied as candidates for antifouling coatings in the work of this thesis. Their antifouling or foul-release performances against freshwater bacterium (*Pseudomonas fluorescens*), marine bacteria (*Vibrio alginolyticus*, *Cobetia*

*marina* and *Marinobacter hydrocarbonoclasticus*), diatom (*Navicula perminuta*), algae (*Ulva linza*) and barnacles (*Balanus amphitrite*) were evaluated.

### 2.2.1 Polysaccharide Surfaces: the effect of surface chemistry

As already introduced above, the primary mechanism in the attachment of marine organisms to surfaces involves secretion of adhesives mainly containing proteins or glycoproteins. Since protein-resistant and cell-resistant surfaces such as oligo- or poly(ethylene glycol) self-assembled monolayers (SAMs) and polysaccharides (especially hyaluronans) have been extensively studied and used in biomedical application, we developed the hypothesis that they are potential candidates for marine antifouling coatings.

Polysaccharides are known as an important class of polymers which fulfill a variety of purposes in the living world. The roles of polysaccharides range from human and animal nutrition over adhesive of cells [12, 33], toward being central components of DNA, the carrier of our genetic information. Due to the large number of stereocenters in the carbohydrate molecular backbone, a wide range of monosaccharides exist which can occur substituted with different end groups. The observable functional variety of polysaccharides is further extended by the different possible combinations of the existing monosaccharides into polysaccharides with varying chain lengths.

As known from cell biology, hyaluronans (or hyaluronic acid) are important components of the extracellular matrix secreted by adhering cells [33]. Hyaluronans are negatively charged at physiological pH and their viscosity in solution shows a polyelectrolyte behavior [33]. A surface-grafted hyaluronan layer is hydrophilic and by absorbing water it can swell within seconds to 2.4-times its initial thickness [34]. Due to the water affinity and the charge repulsion hyaluronans are considered as biological lubricants [33, 35].

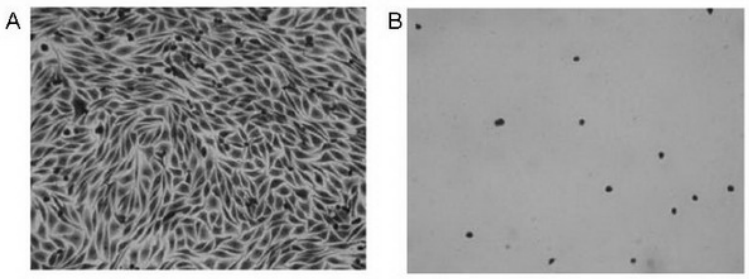


Figure 2.6: Adhesion of L929 fibroblast cells on PEI-coated glass (A) and covalently coupled HA (B) [6].

It is noticeable that covalently immobilized HA surfaces are resistant to the adhesion of mammalian cells such as L929 fibroblasts [6], as shown in Figure 2.6. Meshes coated with HA are resistant to attachment of cells as tested with implants in the

rabbit model [6]. Applied as covalently coupled coating, HA also significantly reduces bacterial adhesion [6]. Interestingly the covalent linkage is very important as physically adsorbed HA does not exhibit these cell resistant properties [6].

Besides HA, AA and PA have also been widely studied to investigate the interactions between surfaces and proteins and cells [5, 36, 37, 38].

With being hydrophilic, having a negative charge and revealing a high degree of affinity to bind water, polysaccharides fulfill previously discussed properties which were connected to inhibition of biofilm formation and protein resistance [29, 39, 40, 41]. Surface coatings produced by natural polysaccharides are expected to be highly environmental friendly.

In chapter 4, biological adhesion on polysaccharide coatings (HA, AA and PA) is discussed in details.

### 2.2.2 Polyelectrolyte Multilayers: the effect of topography

In addition to various chemical approaches, surface topography has also been shown to play a role in mechanical defense against macrofouling on large scale, which may be hindered by certain surface structures [7]. Some recent studies demonstrated that engineered topographically corrugated surfaces are capable of reducing biofouling [10, 11].

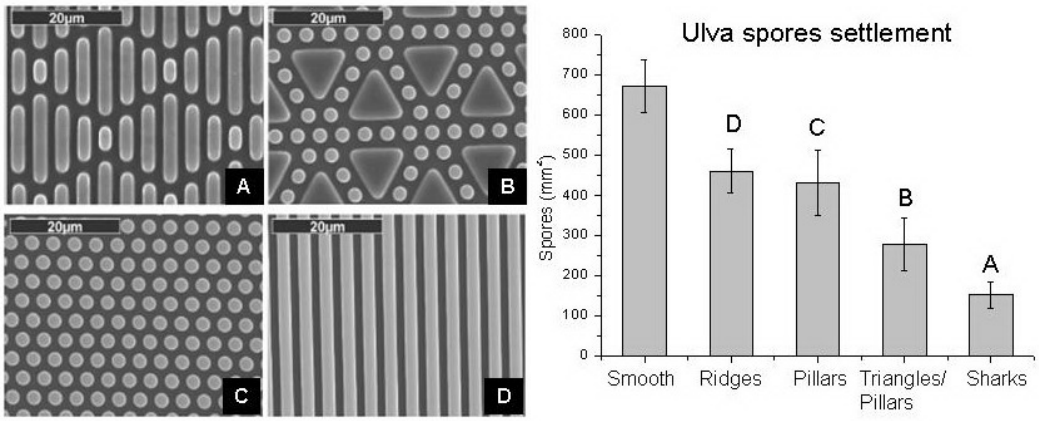


Figure 2.7: SEM images of engineered topographies on a PDMS surface [11].

In Carman and Schumacher's work [10, 11], four different micro-topographies were designed and patterned on polydimethylsiloxane (PDMS) elastomer surfaces. The pattern designs included the biomimetic skin of shark (Figure 2.7A) with 2 $\mu$m wide ribs of various lengths (4, 8, 12, and 16 $\mu$m), 10 $\mu$m equilateral triangles together with 2 $\mu$m diameter pillars (Figure 2.7B), 2 $\mu$m diameter pillars (Figure 2.7C) and 2 $\mu$m wide ridges (Figure 2.7D). The distance between two adjacent features was 2 $\mu$m and the height of these features was approximately 3 $\mu$m.

Settlement of Ulva spores on these surfaces was tested and the results are shown in Figure 2.7. Compared to the flat PDMS surface, settlement of spores can effectively be reduced by surfaces with patterned micro-topography [10, 11]. Although the distance between the features and the height of the features are similar in all the four patterns, structure in Figure 2.7A reduces the settlement of Ulva spores more remarkably. The results suggest that the adhesion of spores is influenced strongly by the feature size, roughness and the geometry of the surfaces. The precise mechanism causing this inhibitory effect in not yet fully understood but nanoforce gradients are currently discussed as possible reason [42].

Because biofouling involves a very diverse range of marine organisms which differ greatly in size, a topographical pattern having a single length scale will not likely perform as a general antifouling surface. Rather, surface structures having multiple length scales should be more promising in the design of an effective antifouling surface [7].

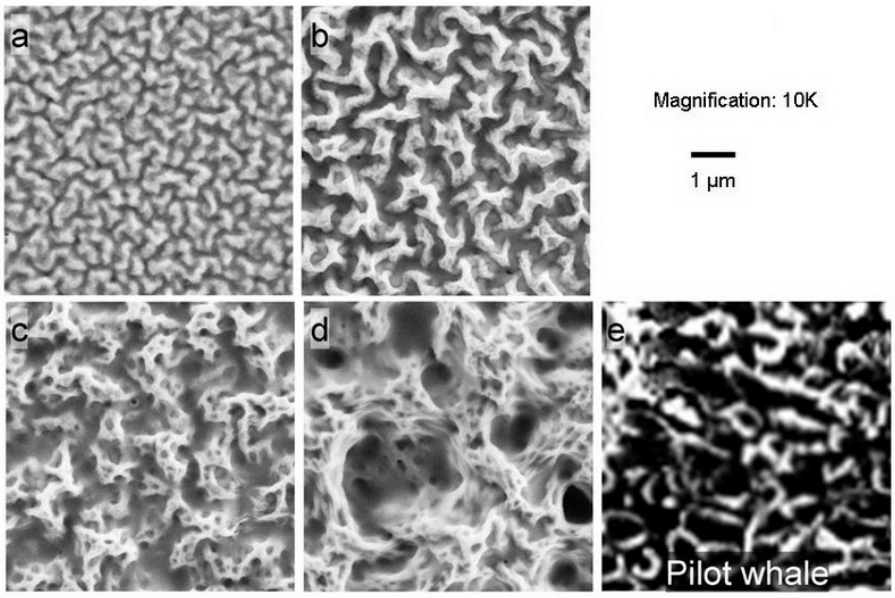


Figure 2.8: SEM images of polyelectrolyte multilayers topography (a-d) and comparison with the skin of pilot whale (e)[43].

Thin films constructed from oppositely charged polyelectrolytes by using a sequential deposition technique are widely studied in recent years. Surface properties such as the topography of polyelectrolyte multilayers can be controlled chemically (e.g. different polyelectrolyte pairs, pH and ionic strength of the polyelectrolyte solution [1]) and technically (e.g. dip or spray deposition, deposition time [44]). In this work, polyelectrolyte multilayers with different morphologies were prepared. The topographies are shown in Figure 2.8. The feature sizes range from several hundred nanometers (Figure 2.8a) to 2 $\mu$m (Figure 2.8d). Structures having multiple

length scales are observed in Figure 2.8c and 2.8d.

The self-cleaning ability of the skin of the pilot whale (Figure 2.8e) is related to its nano-roughness [43]. The structure in Figure 2.8b is highly similar with the skin of the pilot whale. Therefore, polyelectrolyte multilayers can be considered as a biomimetic system suited to study the influence of topography on marine fouling.

Topography is also closely related to the wettability of the surface. By combining chemistry with the effect of the substratum topography, superhydrophobic or non-wettable surfaces can be prepared [7]. Surface modification by various chemicals can change the wettability of polyelectrolyte multilayers and therefore regulate their antifouling or foul-release properties.

The abilities of polyelectrolyte multilayers against the settlement of marine organisms were evaluated. Detailed discussions about the polyelectrolyte multilayers can be found in chapter 5.

# Chapter 3

# Analytical Techniques

Many analytical techniques, such as X-ray photoelectron spectroscopy (XPS), contact angle measurement, spectral ellipsometry, scanning electron microscopy (SEM), atomic force microscopy (AFM) and Fourier transform image analysis, were applied to analyze the chemical and physical properties of the surface coatings. These techniques and the biological evaluation assays are introduced in this chapter.

## 3.1 X-ray Photoelectron Spectroscopy (XPS)

X-ray photoelectron spectroscopy (XPS), which is also called ESCA (Electron Spectroscopy for Chemical Analysis), is currently the most widely used surface analytical technique. In the work of this thesis, numerous XPS measurements were performed and the spectra were applied for qualitative and quantitative surface analysis. Therefore, the fundamental theory of this technique is introduced here.

### 3.1.1 Principles of XPS

The XPS technique is based on the photoemission process. When a surface is irradiated by X-rays, the core level electrons of surface atoms absorb the X-ray photon energy $hv$, overcome their binding energy $E_B$ and are emitted out of the surface with a certain kinetic energy $E_{kin}$. This process is described by the Einstein equation [45]:

$$E_{kin} = hv - E_B - \Psi \tag{3.1}$$

In this equation, $hv$ is the energy of the X-ray source. Mg $K_\alpha$ and Al $K_\alpha$ are the two universally used sources because of their relatively high energy and narrow width (Table 3.1). $\Psi$ is the work function of the instrument. The kinetic energy $E_{kin}$ of the emitted electron is measured by an analyzer. Therefore, the binding energy $E_B$ of the core level electron can be determined.

| X-ray Source | Energy(eV) | Width(eV) |
|---|---|---|
| Mg $K_\alpha$ | 1253.6 | 0.70 |
| Al $K_\alpha$ | 1486.6 | 0.85 |

Table 3.1: General properties of Mg $K_\alpha$ and Al $K_\alpha$ X-ray radiation sources [45].

### 3.1.2 XPS Spectral Features

**Photoelectron Peaks**

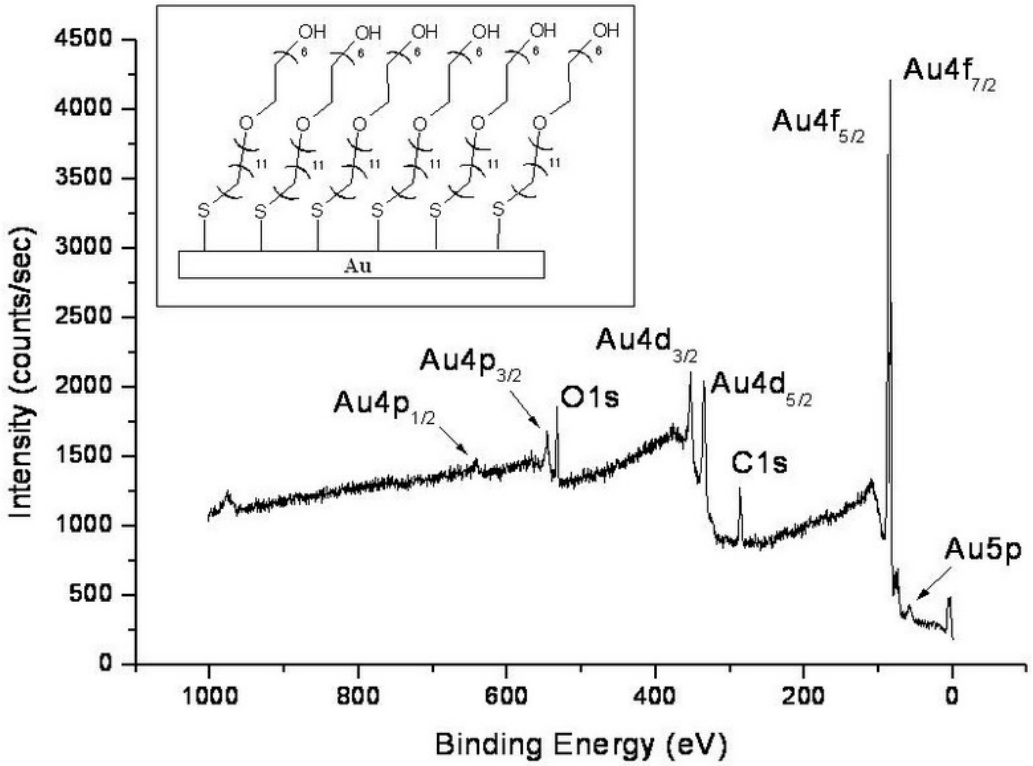


Figure 3.1: XPS survey spectrum of $EG_6OH$ SAMs on Au surface.

Obviously the sharp photoelectron peaks are the most prominent features in the XPS spectra. Figure 3.1 shows a wide scan or survey scan XPS spectrum of an OEG-terminated alkylthiol SAM. $EG_6OH$ ($HS(CH_2)_{11}(OCH_2CH_2)_6OH$) molecules are coupled on the gold surface through the S-Au covalent bond and form polymeric brushes on the substrate surface (as shown in inset of Figure 3.1).

The photoelectrons from C1s and O1s orbitals generate two peaks at about 285 eV and 532 eV, respectively. These peaks indicate the presence of the $EG_6OH$ polymeric brushes on the surface. Since the SAM is only several nanometers thick, photoelectrons from the Au substrate can penetrate the organic thin film and be detected by the analyzer.

### Chemical Shift

The binding energy of a particular peak depends not only on the element but also on the chemical environment and energy state of the atoms. Any change of the chemical environment and state, which perturbs the energy level of the atom, will cause a corresponding variation in the XPS spectrum [45]. This variation in binding energy is called chemical shift. Figure 3.2 shows the C1s XPS spectrum of $EG_6OH$ SAMs. It can clearly explain the chemical shift.

In the spectrum, the observed C1s peak is a combination of two symmetric photoelectron peaks. The photoelectrons emitted from carbon atoms in the alkyl chain generate a peak at 285 eV, while the photoelectrons emitted from carbon atoms in the ethylene glycol groups generate a peak at 286.8 eV. Oxygen is more electronegative than carbon. When a carbon atom is bound to an oxygen atom, the electron density around the carbon atom decreases and the effective nuclear charge increases. Therefore, the core level electrons are more strongly attracted by the nucleus, resulting in a higher binding energy.

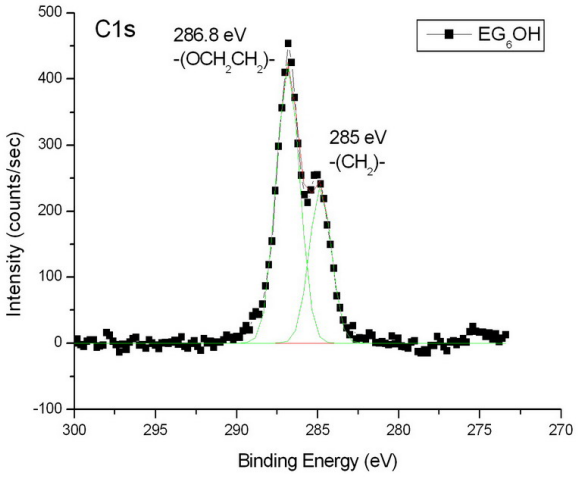


Figure 3.2: C1s XPS spectrum of $EG_6OH$ SAMs.

There are 12 carbon atoms in the ethylene glycol groups and 11 in the alkyl chain, but the intensities of the two peaks are obviously different. In Figure 3.2, the peak intensity of ether carbon (in $-OCH_2CH_2-$) is about two times stronger than alkyl carbon (in $-CH_2-$). The reason is that in the SAMs, the ethylene glycol groups are on top, while the alkyl chains are at the bottom (see inset of Figure 3.1). Therefore, the signal from the alkyl chain is attenuated by the topmost ethylene glycol groups. More details about the intensity of the XPS signals will be discussed in section 3.1.3.

### Multiplet Splitting

Spin-orbital coupling (or $j-j$ coupling) of p, d and f orbitals leads to doublet XPS peaks. For example, the Au4f signal splits as a doublet in Figure 3.3.

The total angular momentum ($j$) of an electron is found by summing the individual electron angular ($l$) and spin ($s$) momenta, $j = l + s$ [46, 47]. For the Au4f orbital, the principal quantum number $n$ equals 4 and the angular momentum quantum number $l$ equals 3. The electron spin momentum quantum number can

be $+1/2$ or $-1/2$, depending on whether the spins of the two electrons are parallel or anti-parallel. Therefore, $j$ can be $j_+ = 7/2$ or $j_- = 5/2$. In this way, the Au4f orbital splits as two different energy states, $4f_{7/2}$ and $4f_{5/2}$.

The separation of the two energy states is about 3.7 eV, which is exactly the distance between the two peaks. The signals of Au4d and Au4p also split into doublets as shown in Figure 3.1. In some cases, the separation of the energy states can be so small that the doublet peaks are not resolved.

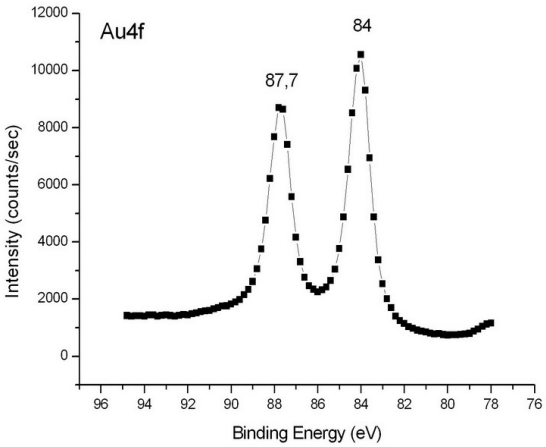


Figure 3.3: Au4f XPS spectrum.

The intensity of the doublets is determined by the occupation probability of the two different energy states, which can also be expressed as the multiplicity, $M = 2j + 1$ [45, 46]. Therefore the intensity ratio of $Au4f_{7/2}$ to $Au4f_{5/2}$ can be calculated as 4/3.

#### Other Features

There are some other features that can be observed in XPS spectra, for example, X-ray satellite peaks, inelastic scattering background, photon-induced Auger electron peaks, shake-up satellites, and valence band features (binding energy $< 30$ eV) [45]. Some of them are also important for interpreting the spectra and understanding the examined surfaces.

### 3.1.3 Quantitative Analysis

#### Chemical Composition

The XPS spectrum of a material contains peaks of various elements (except H and He) present on the surface of that material. The area under these peaks, or the intensities of these peaks, are related to the amount of each element. So the concentration of each detected element can be determined by measuring the intensity of the peaks [45]. The equation for these calculations is:

$$I_{ij} = KT(KE)L_{ij}(\gamma)\sigma_{ij}\int_0^d n_i(z)\exp\left(\frac{-z}{\lambda_{ij}(KE)\cos\theta}\right)\mathrm{d}z \tag{3.2}$$

where $I_{ij}$ is the area of peak $j$ from element $i$, $K$ is an instrumental constant, $T(KE)$ is the transmission function of the analyzer, $L_{ij}(\gamma)$ is the angular asymmetry

factor for orbital $j$ of element $i$, $\sigma_{ij}$ is the photoionization cross-section of peak $j$ of element $i$, $n_i(z)$ is the concentration of element $i$ at a distance $z$ below the surface, $\lambda_{ij}(KE)$ is the inelastic mean free path length of the photoelectron emitted from orbital $j$ of element $i$ with a certain kinetic energy, and $\theta$ is the take-off angle of the photoelectrons measured with respect to the surface normal [45].

If we assume that the elemental concentrations are homogeneous within the XPS sampling depth (from 0 to $d$), which means the distance $z$ has no effect on the concentration $n_i$, Equation 3.2 can be integrated to obtain:

$$I_{ij} = KT(KE)L_{ij}(\gamma)\sigma_{ij}n_i\lambda_{ij}(KE)\cos\theta\left(1-\exp\frac{-d}{\lambda_{ij}(KE)\cos\theta}\right) \tag{3.3}$$

XPS measurements are normally performed with a take-off angle of zero degree, thus $\cos\theta$ equals one. The XPS sampling depth $d$ is about 10 nm, which is usually 3 to 5 times bigger than the $\lambda$ of most photoelectrons with a kinetic energy in the range from 10 to 1000 eV, therefore, the value of $\exp(-d/\lambda)$ is very small and can be neglected. Thus, Equation 3.3 is further simplified as:

$$I_{ij} = KT(KE)L_{ij}(\gamma)\sigma_{ij}n_i\lambda_{ij}(KE) \tag{3.4}$$

Typically, either elemental ratios (e.g., C/O atomic ratio) or atomic percentages are calculated. Thus, it is only necessary to determine the relative relationships, not the absolute values of the quantities in Equation 3.4.

The instrumental constant $K$ is assumed not to vary over the time period and conditions used to acquire the XPS spectra for quantification. It cancels when either elemental ratios or atomic percentages are calculated. The angular asymmetry factor $L_{ij}(\gamma)$ accounts for the type of orbital the photoelectron is emitted from and the angle $\gamma$ between the incident X-rays and the emitted photoelectrons. If only $s$ orbitals as C1s or O1s orbitals are used for quantification, $L_{ij}(\gamma)$ will be the same and therefore cancel. This makes the calculation much easier, especially for the organic polymeric samples. Even for samples where different types of orbitals are used for quantification, the variation of $L_{ij}(\gamma)$ is very small and is usually neglected [45].

Our XPS instrument MAX200 operates in a constant energy analyzer (CAE) mode. In this data acquisition mode, the initial kinetic energy of the emitted electrons is reduced down to a constant pass energy due to the retardation in the lens system of the analyzer [45]. In this case, the only variation in the transmission function $T(KE)$ is due to the retardation in the lens system, which can be determined experimentally [45]. The transmission function setup has been performed by former

colleagues following the instructions in the user manual [48] and the transmission functions of signals with different kinetic energies are stored in the data acquisition program. After recording the spectra, the signals (peaks) are normalized according to their transmission function and therefore their intensities are comparable.

For example, if C1s and O1s peaks are used to calculate the C/O elemental ratio on the sample surface, $K$ and $L_{ij}(\gamma)$ in Equation 3.4 cancel. The peak intensity (normalized with $T(KE)$) ratio can be expressed as:

$$\frac{I_{C_{1s}}}{I_{O_{1s}}} = \frac{\sigma_{C_{1s}}}{\sigma_{O_{1s}}} \times \frac{n_C}{n_O} \times \frac{\lambda_{C_{1s}}}{\lambda_{O_{1s}}} \tag{3.5}$$

In Equation 3.5, the peak area $I$ can be calculated from XPS spectra and the photoionization cross-section $\sigma$ and the inelastic mean free path $\lambda$ can be obtained from literature or database [45, 49]. Thus, the elemental ratio, $n_C/n_O$, can be calculated. Some frequently used values are listed in Table 3.2.

| **Orbitals** | **O1s** | **N1s** | **C1s** | **Si2p** | **F1s** | $Au4f_{7/2}$ |
|---|---|---|---|---|---|---|
| $\sigma$ | 2.93 | 1.80 | 1.00 | 0.54 | 4.43 | 9.58 |
| $\lambda$**(Å)** | 20.3 | 21.5 | 24.0 | 35.2 | - | 36.9 |

Table 3.2: Cross section $\sigma$ and inelastic mean free path $\lambda$ of the photoelectrons [45, 49].

**Layer Thickness**

Lambert-Beer's law is an empirical relationship between the adsorption of electromagnetic radiation and the properties of the material through which the radiation is traveling. It is usually expressed as follows:

$$I_i = I_i^0 \times \exp(-\epsilon c d) \tag{3.6}$$

where $I_i$ is the intensity of the radiation after transmission through the material and $I_i^0$ is the intensity of the radiation before the transmission. $\epsilon$ is the adsorption constant of the material. $c$ is the concentration of the material, and $d$ is the thickness of the material [45].

If a thin film (thickness $<$ 10 nm) is deposited on a substrate, the thickness of the thin film $d$ can be calculated by the attenuation of the signal from the substrate caused by the overlayer. In this case, Lambert-Beer's law (Equation 3.6) can also be applied and expressed as:

$$I_i = I_i^0 \times \exp(-d/\lambda(KE)\cos\theta) \tag{3.7}$$

The signal intensity $I_i$ is obtained from the substrate with a thin film deposited on its surface (Figure 3.4a). The signal intensity $I_i^0$ is obtained from the substrate

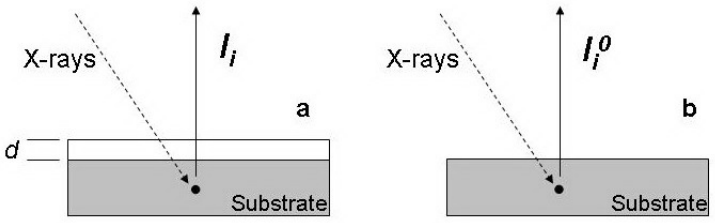


Figure 3.4: Application of Lambert-Beer's law in XPS.

without any overlayer (Figure 3.4b). $d$ is the thickness of the overlayer, $\lambda(KE)$ is the attenuation length of photoelectrons with a certain kinetic energy, and $\theta$ is the take-off angle. Here it must be emphasized that the attenuation length is not exactly the same as the inelastic mean free path. There are detailed discussions about these two parameters in the literature [50]. However, recent work has shown that, for XPS, the inelastic mean free path should be used in preference to the attenuation length when quantifying spectra using simple methods based on intensity ratios [50].

To calculate the thickness of the thin film $d$, Equation 3.7 can be transformed as:

$$d = \lambda \times \cos\theta \times \ln \frac{I_i^0}{I_i} \tag{3.8}$$

For the calculation of film thickness, XPS measurements are performed with a take-off angle of zero degree.

### 3.1.4 XPS Measurements

XPS measurements in this work were performed with the spectrometer MAX200 (Leybold-Heraeus). A non-monochromatic dual anode X-ray source was used. One anode face is coated with magnesium and the other one with aluminum. The design makes the quick switch between the two types of X-ray radiation possible. A concentric hemispherical electron-energy analyzer is used as detector.

All the XPS measurements were performed by first taking a survey scan spectrum covering a range of 1000 eV, and then scanning the individual peaks in more detail over a smaller range of 20-40 eV. These detailed scans with high resolution were used for quantitative analysis. In order to compare the results obtained from measurements made on different days, all the important measurement parameters (such as the scanning steps, the dwell time for each step, the pass energy, and the amount of scans) were kept constant. The parameters used for all the measurements are listed in Table 3.3.

In order to calculate the film thickness by Equation 3.7, a spectrum of a cleaned reference surface was measured. The reference sample is first loaded into the ultra-

| Orbitals | Start(eV) | End(eV) | Step(eV) | Dwell(s) | Pass Energy (eV) | scans |
|---|---|---|---|---|---|---|
| **Survey** | 1000 | -5 | 0.4 | 0.01 | 96 | 3 |
| **Au4f** | 95 | 75 | 0.2 | 0.04 | 48 | 12 |
| **C1s** | 300 | 270 | 0.2 | 0.10 | 48 | 15 |
| **O1s** | 545 | 520 | 0.2 | 0.12 | 48 | 15 |
| **Si2p** | 114 | 95 | 0.2 | 0.10 | 48 | 15 |
| **N1s** | 420 | 395 | 0.2 | 0.25 | 48 | 20 |
| **Ca2p** | 360 | 340 | 0.2 | 0.20 | 48 | 20 |
| **F1s** | 695 | 675 | 0.2 | 0.10 | 48 | 15 |

Table 3.3: Parameters for XPS measurements.

high vacuum chamber and the XPS measurement is performed at a certain spot on the surface of the sample. Due to a small amount of contamination on the surface, a weak C1s signal is always visible. After that, the measured spot is focused under a fine-focus ion gun integrated on the spectrometer (IQE-12/38, Leybold-Heraeus). Ar atoms are ionized and accelerated by high voltage and bombarded onto the surface with high speed. Consequently, the contaminations are removed. A XPS measurement is taken at the same spot again and a reference spectrum for the pure substrate surface can be obtained. The instrumental parameters for argon sputtering are listed in Table 3.4.

| **Ar Pressure** (mbar) | **Emission Current** (mA) | **Voltage** (V) | **Sputter Area** ($mm^2$) |
|---|---|---|---|
| $5 \times 10^{-4}$ | 10 | 4000 | $6 \times 6$ |

Table 3.4: Instrumental parameters for Ar sputtering.

### 3.1.5 XPS Spectral Analysis

The position of photoelectron peaks will shift by several eV when the tested surface is electrically isolated or the coatings is on an insulator. In this case, the binding energy scale of the spectrum has to be calibrated by the position of a standard peak. When the coatings are prepared on gold surface, the $Au4f_{7/2}$ peak serves as the standard and is set to 84 eV. In most cases, the binding energy of the C1s peak from alkyl carbon is set to 284.8 eV as standard. In this thesis, the C1s peaks are usually broad and asymmetric due to the chemical shift, therefore, the Si2p peak at 103.4 eV (from glass slides or $SiO_2$/Si wafers) serves as the standard to calibrated the peak position.

After the data acquisition in XPS measurements, spectra are normalized according to the transmission function in order to compare the intensities of individual peaks and quantify the data.

There are two main methods to obtain the intensity (peak area) of the photoelectron peak. The first is peak integration. Before integrating a curve and calculating the area under the peak, the background must be subtracted. Two kinds of back-

ground, Shirley and Tougaard [50], are commonly applied for quantification. In this work, the Shirley background was used for peak intensity calculation. The second method is peak fitting. Figure 3.2 shows an example for peak fitting. When a photoelectron peak of an element appears broad and asymmetric, it usually contains contributions from atoms in several different chemical environments. The asymmetric peak can then be fitted as a combination of several symmetric sub-peaks. In this thesis, Gaussian functions were used for fitting each sub-peak, and the position, height, width and area of the peak were thus obtained. In order to achieve a better peak fitting result, the background should also be subtracted.

## 3.2 Contact Angle Measurement

When a drop of liquid is placed on a solid surface, it makes a contact angle $\theta$ with the surface. The contact angle is defined as the angle between the tangent to the solid-liquid interface and the tangent to the liquid-vapor interface (as shown in Figure 3.5).

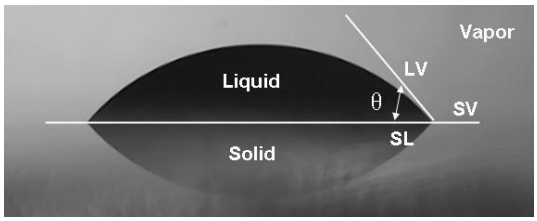


Figure 3.5: Water drop on a solid substrate.

If the solid surface is 'ideal', which is defined as smooth, rigid, chemically homogeneous, insoluble, and non-reactive [51], the contact angle is determined by the Young equation [52]:

$$\cos\theta_Y = \frac{\gamma_{SL} - \gamma_{SV}}{\gamma_{LV}} \tag{3.9}$$

where $\gamma_{SL}$, $\gamma_{SV}$ and $\gamma_{LV}$ are the solid-liquid, solid-vapor and liquid-vapor interfacial tensions. The Young contact angle $\theta_Y$ represents the physico-chemical nature of the wetting system. It is independent of either geometrical features or gravity [51]. But in the real case, both surface chemistry and topography have influences on the apparent contact angle on the surface.

The contact angle on a chemically heterogeneous surfaces is described by the Cassie equation [53], for the case of a surface with only two different chemistries:

$$\cos\theta_C = x_1 \cos\theta_{Y_1} + x_2 \cos\theta_{Y_2} \tag{3.10}$$

In this equation, $\theta_C$ is the Cassie contact angle, $x$ is the area fraction characterized by a given chemistry, and subscripts 1 and 2 indicate the two different surface chemistries. When the drop size is sufficiently large with respect to the scale of chemical heterogeneity, $\theta_C$ is a better approximation for the most stable apparent contact angle [51].

The contact angle on a rough surface is described by the Wenzel equation [54]:

$$\cos\theta_W = r\cos\theta_Y \tag{3.11}$$

In this equation, $\theta_W$ is the Wenzel contact angle, $r$ is the roughness ratio, defined as the ratio between the actual and projected solid surface area ($r = 1$ for a smooth surface and $> 1$ for a rough surface. The Wenzel equation predicts that hydrophobicity is enhanced by the roughness ($\theta_W > \theta_Y$) when $\theta_Y$ is larger than 90 °. Conversely, hydrophilicity is increased by the roughness when $\theta_Y$ is smaller than 90 °.

There are two commonly applied techniques to measure the contact angle. The first is the direct measurement by viewing through a microscope with a goniometer eyepiece. In this thesis, some measurements were performed on such a goniometer (Model:G1 Kruess, Germany). The second technique, which is nowadays also more widely applied, is computer-assisted analysis. The image of the liquid drop is recorded by a CCD camera and the picture is displayed on the computer screen as shown in Figure 3.5.

The contact angle is determined by analyzing the shape of the sessile liquid drop. The shape of a drop is determined by the balance between surface tension, gravity effects and the specific interactions between liquid and solid surface. The surface forces lead to a spherical shape of the liquid drop whereas gravity tends to flatten the sessile drop [55]. Experimentally an image of the sessile drop is recorded and the software identifies the contour of the drop and analyzes its shape. Mathematic calculation generates a curve to fit to the shape of the sessile drop. The contact angle is obtained at the point where the fit meets the shadow contour of the drop. The method is called aximetric drop shape analysis (ADSA) [55].

In my experiments, the static water contact angle on a surface was used to examine surface coatings. When the term 'contact angle' is mentioned in the following discussions, it means the contact angle of water on a surface. To get better statistic results, the contact angle was measured at three different spots on each surface and the average was calculated.

## 3.3 Spectral Ellipsometry

### 3.3.1 Fundamental Theory of Ellipsometry

Ellipsometry is a very sensitive surface and thin film measurement technique that uses polarized light [56]. When a polarized light is reflected from a surface deposited with a thin film, the polarization and intensity of the light are changed due to the properties of the thin film, such as the optical constants (complex refractive index and dielectric function tensor) and film thickness. By detecting and analyzing the changes in polarization and intensity of the light, optical constants and film thickness can be determined.

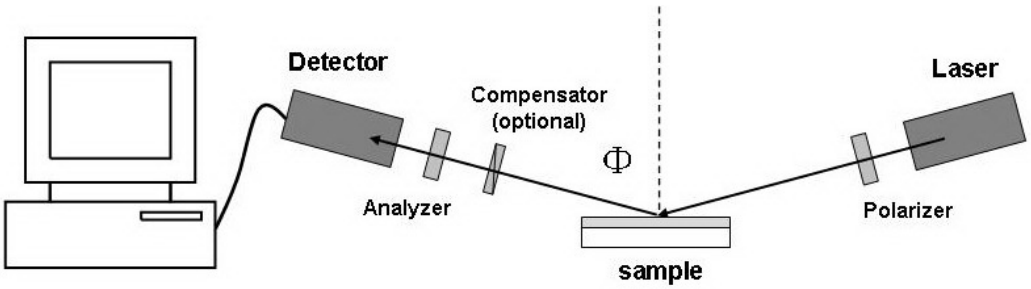


Figure 3.6: Schematic experimental setup of ellipsometry technique.

A schematic setup for a ellipsometry experiment is shown in Figure 3.6. Incident light from a source is linearly polarized to two polarization states by a polarizer. If the electric field of the polarization state is perpendicular to the plane of incidence, it is called *s-polarized*. If the electric field of the polarization state is parallel to the plane of incidence, it is called *p-polarized*. Due to the absorption of the sample (thin film), the reflected wave is not linearly polarized but elliptically polarized [57]. The changes in polarization of the reflected light are analyzed and detected by an analyzer and a detector, and the signals are converted for analysis and calculation by the computer. The parameters of the polarization ellipse are determined by the optical constants and the thickness of the thin film.

The amplitude of the wave changes after the reflection from the sample surface. The reflection coefficient ($r$) is used to define the ratio of the amplitude of the reflected wave $E_{r0}$ to the amplitude of the incident wave $E_{i0}$ as [57]:

$$r = \frac{E_{r0}}{E_{i0}} \tag{3.12}$$

Ellipsometry measures the ratio of the reflection coefficients of $p$- and $s$- polarization ($r_p$ and $r_s$). Conventionally, this ratio is represented in terms of the ellipsometric angles, $\Psi$ and $\Delta$, as [58]:

$$\rho = \frac{r_p}{r_s} = \tan(\Psi)\exp(i\Delta) \tag{3.13}$$

Because ellipsometry measures the ratio of two values it can be highly accurate and very reproducible. The ratio is a complex number, it also contains 'phase' information ($\Delta$), which makes the measurement very sensitive [56].

In general, the measured $\Psi$ and $\Delta$ cannot be converted directly into the optical constants of the sample. Normally, a model analysis must be performed which assumes a layer model. This model considers the optical constants and thickness parameters of all individual layers of the sample. Using an iterative procedure (least-squares minimization) unknown optical constants and/or thickness parameters are varied, and $\Psi$ and $\Delta$ values are calculated using the Fresnel equations [56]. The calculated $\Psi$ and $\Delta$ values which match the experimental data best provide the optical constants and thickness parameters of the sample.

In ellipsometry, a spectroscopic measurement is more sensitive and also provides more information than a single wavelength measurement. Ellipsometry works best for film characterization when the film thickness is of the same order as the wavelength of the incident light [56]. Therefore, it is more sensitive to characterize a thin film in the short wavelength region or a thick film in the long wavelength region. The optical constants of a sample can be correlated to the wavelength of the incident light by some empirical equations (such as the Cauchy equation). In this case, the spectral dependent equations can be applied to analyze the experimental data acquired over a certain region.

Surfaces with large roughness can cause non-specular scattering of the incident beam and depolarization of the specularly reflected beam [56], therefore they are not suitable for ellipsometry measurement. Thin films deposited on transparent substrates such as glass are also difficult to measure by ellipsometry, because the reflection from the backside of the glass strongly interferes with the reflection from the surface.

### 3.3.2 Ellipsometer Hardware

The ellipsometry measurements were performed on a fixed-angle M-44(TM) ellipsometer (J.A.Woollam, USA) [59]. The lamp housing and lamp power supply are integrated into one unit (LPS-400). The arc lamp, a high pressure Xe discharge point source lamp, serves as the light source. A fiber optic cable is used to couple the beam from the lamp housing to the input unit of the ellipsometer. The input unit conditions the beam before it encounters the sample. The output unit consists of an analyzer and a detector that further condition the beam and convert it into electrical signals. The main computer operates the WVASE32(TM) data acquisi-

tion and analysis software. The main function of this computer is to communicate with the remote computer located within the EC-120 electronics control box. It also analyzes all data acquired from the embedded computer and displays the results on the screen.

### 3.3.3 Ellipsometry Measurements

After sequentially switching on the arc lamp, the EC-120 electronics control box, and the computer, the hardware of the M-44(TM) system has to be initialized by the WVASE32(TM) software. Then a reference sample is placed on the sample stage for beam alignment. A good alignment can be achieved by adjusting the height and tilt of the sample stage to make sure that the reflection of the beam from the sample surface is centered on the detector aperture. After alignment, system calibration is performed with a standard sample (silicon wafer covered with 25 nm $SiO_2$) at 500 nm wavelength and 75 ° angle of incidence.

The sample is placed on the stage and the beam is properly aligned. Then experimental data is acquired and saved. Thereafter, a suitable model is established for the measured sample. The Cauchy model is usually applied for organic thin films. The Cauchy equation is an empirical relationship between the refractive index $n$ and the wavelength of light $\lambda$ for a particular transparent material. The general form of the Cauchy equation is [60]:

$$n(\lambda) = A + \frac{B}{\lambda^2} + \frac{C}{\lambda^4} \cdots \tag{3.14}$$

where A, B, C, etc., are coefficients that can be determined for a material by fitting the equation to measured refractive indices at known wavelengths. Usually, it is sufficient to use a two-term form of the Equation 3.14:

$$n(\lambda) = A + \frac{B}{\lambda^2} \tag{3.15}$$

For the ellipsometry measurements in this thesis, the default value of coefficient A is 1.45 and the default value of coefficient B is 0.01.

The optical constants or the thickness of the thin film on a non-transparent substrate can be obtained by the fitting between calculated data from the model and the measured experimental data. In our work, we are more interested in the film thickness. The thickness of the thin film coated on Si-wafers was obtained from the ellipsometry measurements. To have reliable statistical results, all the samples were measured three times at different spots and the averages were calculated.

## 3.4 Scanning Electron Microscopy

Scanning electron microscopy (SEM) is one of the most widely used electron microscopic techniques where images are obtained by focusing a high energy electron beam onto the surface of a sample and detecting signals from the interactions of the incident electrons with the surface.

The interactions between the electron beam and the sample result in the emission of electrons and electromagnetic radiation, such as primary backscattering electrons, secondary electrons, Auger electrons and X-rays. All these electrons and electromagnetic radiation can be appropriately detected by different kinds of detectors to produce an image [61]. Among all these detection modes, the secondary electron detector is the most commonly applied for topography imaging [61]. The mechanism of SEM topography imaging is shown in Figure 3.7.

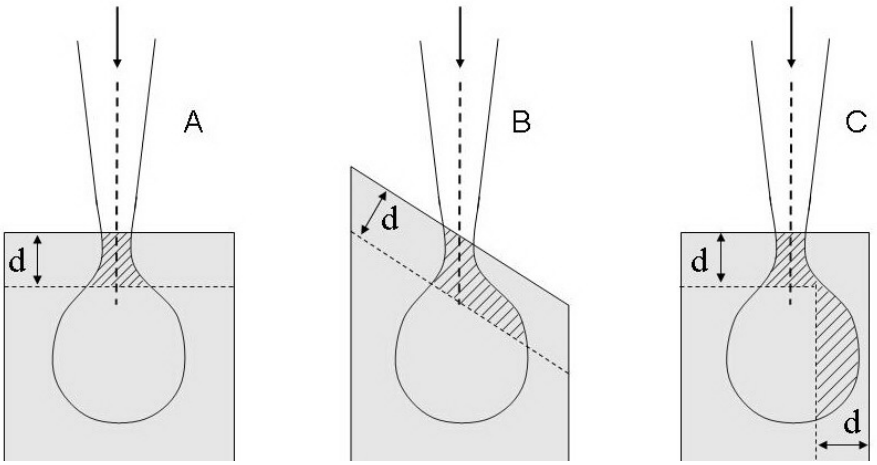


Figure 3.7: Effect of surface topography on SEM imaging.

The electron beam illuminates on the sample and generates a zone of interaction between the beam and the sample. Low energy secondary electrons can only escape from a limited depth ($d$, a few nanometers) below the surface. When the surface is flat, the beam enters the sample perpendicularly and the activated region from where the secondary electrons can escape (shadowed area in Figure 3.7A) is relatively small. In the case of a rough surface with steep structures, the beam enters the surface with a certain angle, resulting in a larger activated region (Figure 3.7B). If the beam is focused on the edge of the sample, the activated region is also larger (Figure 3.7C). The brightness of the signal depends on the number of secondary electrons reaching the detector. A larger activated region generates more secondary electrons, therefore, steep structures on the surface and the edge of the surface are brighter than the flat area on the surface, thus reflecting the topography of the surface.

Since SEM is based on the interactions of the electron beam with the surface, and in most cases emitted electrons from the surface are detected, a vacuum system is necessary to reduce their interactions with gas molecules.

In this thesis, numerous SEM images were used to display the topography of the polyelectrolyte multilayers. All these images were recorded with a LEO1530 Gemini electron microscope using the secondary electron detector. The EHT (Electron High Tension), which is the accelerating voltage, was set to 3 kV. Before imaging, the polyelectrolyte multilayer samples were coated with a very thin layer of graphite (Bal-Tec MED020 coating system) to make the surface electrically conductive.

## 3.5 Atomic Force Microscopy and Surface Roughness

In atomic force microscope (AFM), a cantilever is placed parallel to the surface. The cantilever has a sharp, force-sensing tip at its end, which interacts with the surface. As the interaction force between the cantilever tip and the surface varies, deflections are produced in the cantilever. The deflections are measured and used to compile a topographic image of the surface [45].

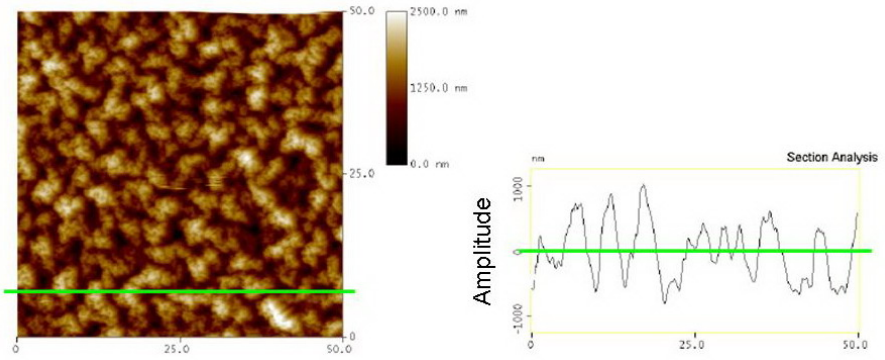


Figure 3.8: AFM image and its section analysis (linear scan) to show the vertical deviation of the polyelectrolyte multilayer surface.

The deflection of the cantilever also generates a depth profile (or height profile) to show the vertical deviations along the surface in the nanometer range (as shown in Figure 3.8). The amplitude of the vertical deviations is normally used to calculate the roughness of the surface. In this case, AFM is usually operated in the contact mode for topography imaging and height analysis.

$R_a$ and $R_{rms}$ are the two most commonly used amplitude parameters to describe the surface roughness. $R_a$ is the arithmetic average of absolute amplitude values and $R_{rms}$ corresponds to the root mean squared amplitude values. They are defined as [62]:

$$R_a = \frac{1}{n}\sum_{i=1}^{n}|A_i| \tag{3.16}$$

$$R_{rms} = \sqrt{\frac{1}{n}\sum_{i=1}^{n}A_i^2} \tag{3.17}$$

where $A$ is the amplitude value of the vertical deviations.

AFM topography imaging and roughness measurements on polyelectrolyte multilayer surfaces prepared in this work were performed in collaboration with Frank Leisten at the University of Hannover.

## 3.6 Fourier Transform Image Analysis

The Fourier transform (FT) is a mathematic method to decompose a function into its sine and cosine components, therefore a signal (usually in time-domain or spatial domain) can be transformed into frequency domain. This transformation is particularly useful for a periodic function. A digital image can be considered as a two-dimensional (2D) signal in spatial domain and therefore can be converted into frequency domain by 2D Fourier Transform (2D-FT). 2D-FT is widely used in image processing [63].

For numerical computations on a computer, discrete Fourier transform (DFT) has to be applied to deal with the discrete and finite signals, such as pixels in digital images [63]. The brightness of pixels can be considered as the amplitude of the signals.

For a two-dimensional function (e.g. an image) of size $N \times N$, the two-dimensional DFT is given in equation 3.18 for the spectral coordinates $m$ from 0 to $N-1$ and $n$ from 0 to $N-1$ [63]:

$$G(m,n) = \frac{1}{N}\sum_{u=0}^{N-1}\sum_{v=0}^{N-1} g(u,v)\cdot e^{-i2\pi(\frac{mu}{N}+\frac{nv}{N})} \tag{3.18}$$

The resulting Fourier transform is a two-dimensional function of the same size ($N \times N$) as the original signal. The number of frequencies corresponds to the number of pixels in the spatial domain image

In this work polyelectrolyte multilayers with different morphologies were prepared. The features on the multilayer surfaces show some kind of random arrangement. Fourier transform was applied to analyze the spatial texture size of the polyelectrolyte multilayer surfaces. The analysis procedure is shown in Figure 3.9.

From a square section of the SEM picture (Figure 3.9A) the power spectrum

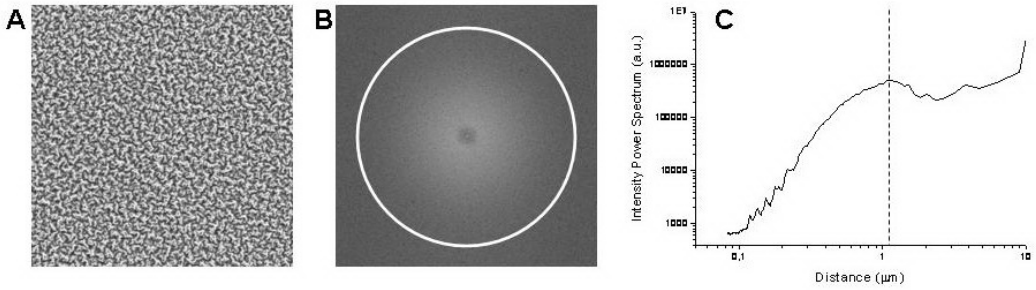


Figure 3.9: Fourier transform image analysis on the SEM photos of polyeletrolyte multilayers.

(Figure 3.9B) is calculated. Then, concentric fringes are used to determine the occurrence of specific frequencies in the power spectrum. One example for such a fringe is plotted into the power spectrum (Figure 3.9B). The mean intensity within this fringe is then plotted in a diagram against the peak to peak distance corresponding to the spatial frequency (radius of the fringe in Figure 3.9B). Such a diagram (Figure 3.9C) gives then the degree of occurrence of specific frequencies in the SEM image. As it can be seen in Figure 3.9C for the given example, the topography of the polyelectrolyte surface has a significant amount of peak to peak distances between 0.7-1.5 $\mu$m, centered around 1.1 $\mu$m.

In this thesis, Fourier transform image analysis is performed with a program edited by Dr. A. Rosenhahn (University of Heidelberg) using MATLAB.

## 3.7 Biological Evaluations

As mentioned in section 2.1, in order to represent the major fouling groups including microfoulers, soft macrofoulers and hard macrofoulers, freshwater bacterium (*Pseudomonas fluorescens*), marine bacteria (*Vibrio alginolyticus*, *Cobetia marina* and *Marinobacter hydrocarbonoclasticus*), diatom (*Navicula perminuta*), alga (*Ulva linza*) and invertebrates barnacles (*Balanus amphitrite*) were chosen as the fouling species to evaluate the antifouling and foul-release properties of the surfaces prepared in this work. The biological evaluation assays are performed in collaboration with AMBIO project partners. The methods are briefly introduced in this section.

### 3.7.1 Freshwater Bacterium

The freshwater bacterium *Pseudomonas fluorescens* is a typical fouling organism in piping systems, heat exchangers and membrane filters [17]. The antifouling and foul-release properties of the polysaccharide coatings with respect to *Pseudomonas fluorescens* were characterized by the project partners Y. Liu, S. Wang and Dr. Q. Zhao from the University of Dundee (UK).

After one hour of leaching in circulating deionized water, samples were immersed in a glass tank containing 500 mL suspension of *Pseudomonas fluorescens* with a concentration of $10^6$ cells/mL for bacterial adhesion. The tank was placed in a vibrate-incubator at 28 °C for one hour with a shaking speed of 20 rpm.

After the adhesion step, the samples were removed from the tank and rinsed in sterile distilled water at 28 °C. Each sample was first moved down-up 20 times vertically in glass tank A, which was filled with sterile distilled water, with a constant speed to detach adhered bacteria. Then it was immersed in sterile distilled water in glass tank B and sonicated in an ultrasonic bath to remove the remaining attached bacteria. The number of bacteria in tank A was counted as $De$ (detached cells) and the number of bacteria in tank B was counted as $Re$ (remained cells). Data were expressed as CFU (Colony-Forming Units).

Thus, the total amount of bacteria that adhered ($Ad$) on the sample surface is the sum of the detached cells ($De$) and remained cells ($Re$) [17].

### 3.7.2 Marine Bacterial Biofilm

The three bacteria *Vibrio alginolyticus*, *Cobetia marina* and *Marinobacter hydrocarbonoclasticus* are common marine biofilm bacteria. They form an early biofilm as starting point for biofouling in marine environment. Antifouling and foul-release effects of polysaccharide coatings on each single bacterium and the mixture of these three species were tested by project partners F. D'Souza, G. Donnelly and P. Willemsen from TNO (NL).

Samples were conditioned in artificial seawater (ASW) for one hour prior to the assay. The bacterial suspension used for the testing was obtained after the cells were repetitively washed and centrifuged to remove excess EPS for optimal adhesion.

Replicate slides were placed in quadriperm plates and immersed in 8 mL suspension of the bacterium (or bacterial mixture) with an optical density (OD) of 0.2 (at 595 nm) for one hour. Then slides were rinsed to remove non-adhered cells and incubated in 8 mL sterile filtered seawater with growth medium for four hours. After incubation and drying, 4 spots on each slide were subsequently stained with the fluorochrome Syto 13 for biomass quantification by fluorescent microscope. Data were expressed as RFU (Relative Fluorescence Units).

After the biofilm formation step, two replicates of each coating were rotated on a rotor for ten minutes at 12 knots in natural seawater. The remaining biofilm was then quantified as described above [17].

### 3.7.3 Algae: Ulva and Diatom

#### Ulva

*Ulva linza* is the most common ship-fouling alga and the colonization of *Ulva* starts by the settlement of motile zoospores on submersed surfaces. The settlement and strength of attachment of *Ulva* spores on the polysaccharide and polyelectrolyte multilayer surfaces were tested by project partners Dr. M. Pettitt and Dr. M. Callow from the University of Birmingham (UK).

Surfaces were equilibrated in ASW for one hour prior to the assay. 10 mL of freshly released spores in ASW ($1.5 \times 10^6$ spores/mL) were added to each test surface placed in a compartment of a sterile quadriperm dish. Six replicates of each test sample were immersed simultaneously. The slides were incubated in darkness for 45 mins and then washed gently in ASW to remove unsettled spores. Three replicates were fixed in glutaraldehyde, washed in deionized water and air-dried to determine the number of initially attached spores. Spores were counted using a Zeiss Kontron 3000 image analysis system attached to a Zeiss epifluorescence microscope. Spores were visualized by autofluorescence of chlorophyll and counts were recorded for 30 fields of view on each slide.

To determine the adhesion strength of attached spores the remaining three replicates were exposed to a shear stress in a calibrated water channel [64]. The apparatus was run at maximum velocity creating a wall shear stress of 51 Pa. The number of spores remaining after flow was compared to the unexposed samples [17].

#### Diatom: Navicula perminuta

Diatoms, such as *Navicula perminuta*, settle on the surface by gravity and form a compact biofilm which is difficult to be removed. The foul-release properties of polysaccharide surfaces with respect to diatom (*Navicula perminuta*) cells were also tested by project partners from University of Birmingham (UK).

The assay procedure was similar to that described for *Ulva* spores. After one hour equilibration in ASW, samples were incubated with a suspension of diatom cells for two hours in light. Cells were counted using image analysis similar as described above. For cell detachment studies, slides were exposed to 2.95 Pa wall shear stress in the water channel apparatus [17].

### 3.7.4 Invertebrates: Barnacle Cyprids

*Balanus amphitrite* is the major hard macrofouler of submersed artificial surfaces in marine environment. The settlement of barnacle (*Balanus amphitrite*) cyprids was evaluated by project partners R. Mutton, S. Conlan and Prof. A. Clare from

Newcastle University (UK).

Samples were equilibrated in ASW for one hour before the assay. Twenty 3-day-old barnacle cyprids were introduced to each slide contained within 1 mL ASW. The slides were incubated at 28 °C for 24 hrs in darkness. After this period, the attached cyprids were counted and expressed as percentage settlement. After a further period of 24 hours, the attached cyprids were counted again and the settlement data obtained for 48 hours in total [17].

# Chapter 4

# Polysaccharide Coatings

As mentioned in section 2.2, the studies of polysaccharide coating in biomedical application demonstrated that immobilized polysaccharides such as hyaluronan can effectively resist the adhesion of cells and bacteria [6]. Therefore, we developed the hypothesis that polysaccharides are potential candidates for marine antifouling coatings.

In this chapter we focus on three different acidic polysaccharides as coating materials: hyaluronic acid (HA), alginic acid (AA) and pectic acid (PA). HA is one of the major connective tissue polysaccharides (also named as 'glycosaminoglycans') which contain one or several types of amino sugar moieties [65]. The large linear polyanionic molecules of HA have repeating units of the disaccharide $\beta$-D-acetylglucosamine-glucuronic acid (Figure 4.1). Alginic acid and pectic acid are more common as constituents within plant cells. Alginate is a natural polymer that exists in many species of seaweed. It is composed of two repeating units with different stereochemistry, $\beta$-D-$(1 \rightarrow 4)$-mannuronate (M unit) and $\alpha$-L-$(1 \rightarrow 4)$ guluronate (G unit) as shown in Figure 4.1 [66]. In this study, straight-chain alginate mostly containing mannuronate units, or 'high M' alginate was used. Pectic acid (polygalacturonic acid), or pectin, is one of the major plant cell-wall polysaccharides. The main sources of commercial pectin are citrus peel and apple pomace. They are widely used in the food industry [67]. The pectic acid studied in this work consists of linear chains of $\alpha$-D-$(1 \rightarrow 4)$ galacturonic acid as shown in Figure 4.1 [66].

In this chapter, surface preparation and surface analysis of the polysaccharide coatings are discussed in detail. The adhesion and release properties of the three types of polysaccharide surfaces were tested towards a selection of marine bacteria (*Marinobacter hydrocarbonoclasticus*, *Cobetia marina*, *Vibrio alginolyticus*), freshwater bacterium (*Pseudomonas fluorescens*), algae (*Ulva linza*, *Navicula perminuta*) and barnacle cyprids (*Balanus amphitrite*). The goal of this work is to test if the

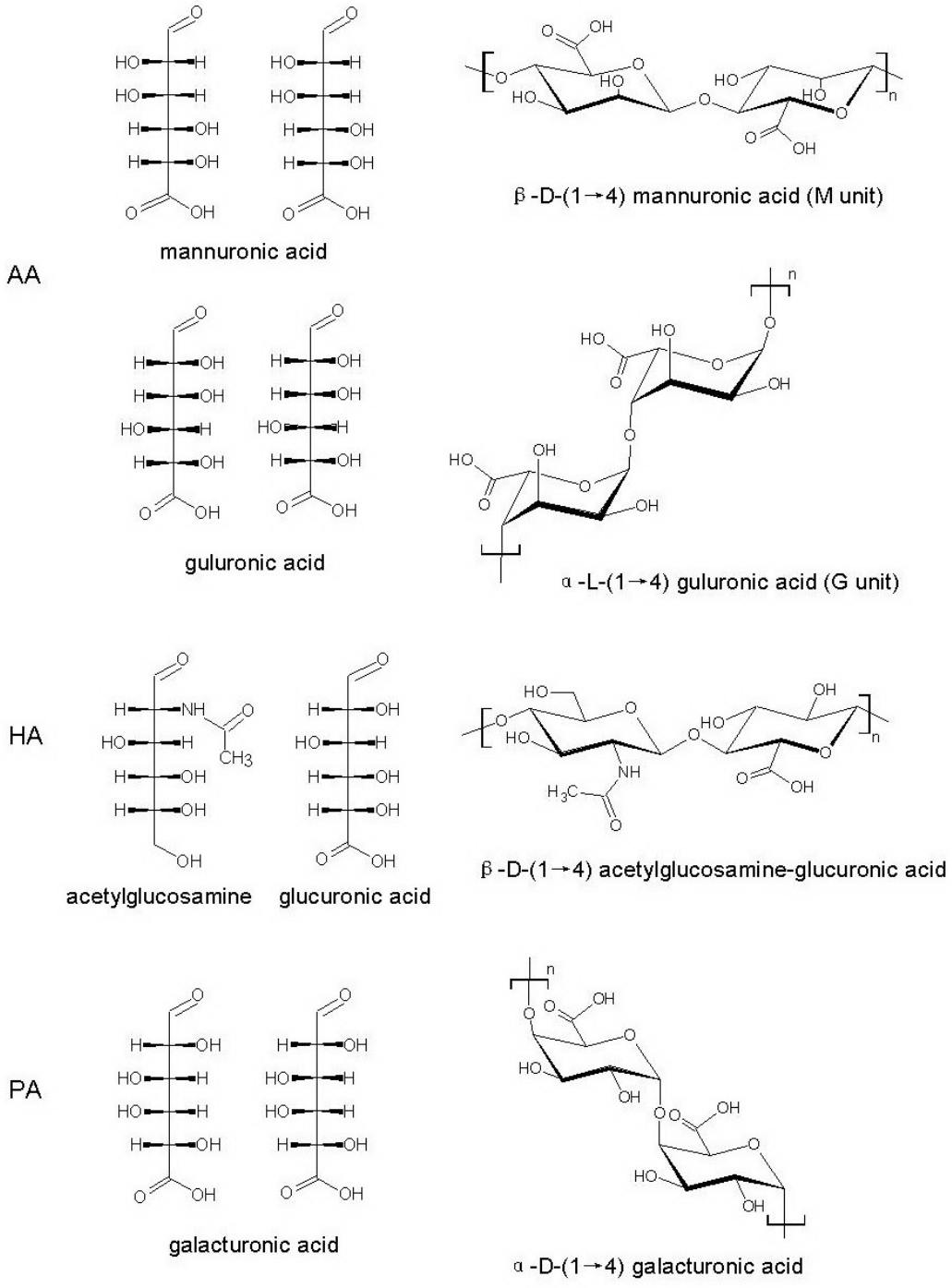


Figure 4.1: Molecular structures of the three polysaccharides: alginic acid (AA), hyaluronic acid (HA) and pectic acid (PA).

known resistant behavior of the polysaccharide surfaces against cell and bacteria adhesion in cell biology and tissue engineering [5, 6] is also valid for the marine environment.

Discussions about the influences of polysaccharide surfaces on biological adhesion are based on the surface properties, such as surface functional groups, molecular conformation, surface charge, wettability and interactions with cations.

## 4.1 Preparation of Polysaccharide Coatings

Preparation of polysaccharide coatings on solid substrates such as glass slides and silicon wafers includes four steps. First, the substrate surface must be thoroughly cleaned. Second, the cleaned surfaces are functionalized with amino groups by aminosilane coupling. After that, polysaccharide molecules are covalently linked to the surface. Finally, exceeding polysaccharide molecules that are only physically adsorbed on the surface are removed by a leaching step [68].

### 4.1.1 Surface Cleaning

The cleanness of the surface has extremely strong influence on the homogeneity and stability of the coatings. Therefore, a strict procedure was applied to clean the surfaces. First, glass slides were rinsed with deionized water, 96% ethanol and mechanically wiped using ethanol and tissue. Then the slides were cleaned in 20% extran solution bath with ultrasonic for 30 minutes. After that, they were rinsed with deionized water again and dried by $N_2$ gas. They were then soaked in piranha solution ($H_2SO_4 : H_2O_2 = 3 : 1$) for one hour. The glass surface are functionalized with hydroxyl groups in this step, which are important for the coupling of aminosilane. Finally, the slides were rinsed with millipore water and dried with $N_2$ gas.

### 4.1.2 Aminosilane Coupling

Silane coupling agents are generally considered to react chemically with both substrate and top-coating, forming covalent bonds across the interface that are both strong and durable. There are three widely used methods to immobilize alkoxy silane on the surfaces of glass, silicon wafers and silica particles. They are the organic solvent method [37], the wet chemistry method [69, 70] and chemical vapor deposition (CVD) [71, 72, 73]. The method of preparation has a remarkable effect on the coating properties, such as layer thickness, surface density and orientation of the surface molecules [72]. In order to find the most suitable method for our purpose, all three methods have been tested. 3-Aminopropyltriethoxysilane (APTES)

was used to silanize the glass or silicon wafer surface. The amino end-group in the APTES molecule is necessary for the following covalent coupling of polysaccharides.

#### Organic Solvent Method

In this method, alkoxy silane is dissolved in organic solvent like benzene, tetrahydrofuran (THF) or toluene. Then, the substrates are immersed in the solution for the immobilization of the silane molecules.

Toluene was used as the solvent in my experiments. Firstly, glass slides were cleaned and activated as described above and dried. They were placed vertically in a glass container (purchased from NeoLab). Secondly, 5%(vol) APTES/toluene solution was added in the container to completely cover the slides. To minimize the interference of humidity, the container was kept in an exsiccator and weak vacuum was applied. The APTES coverage of the surface depends on the deposition time. After the slides were removed from the solution, they were sonicated in toluene for three minutes, in absolute ethanol for another three minutes and dried by $N_2$ gas.

There are several obvious disadvantages in this organic solvent method. First, organic solvents, such as toluene, are highly toxic. Second, water strongly interferes the reaction, therefore the substrates must be dry and the solvent must be dehydrated. Additionally, humidity should also be avoided.

#### Wet Chemistry Method

The wet chemistry method is a 3-step reaction [70]. Initially, the $-OCH_2CH_3$ groups in the APTES molecules are hydrolyzed to $-OH$ groups. Oligomers are formed in the following condensation step, and the silanol oligomers are anchored on the surface by hydrogen bonding. A further heat treatment is applied to convert hydrogen bonds into covalent bonds. The reaction process is shown in Figure 4.2.

Firstly, a solution with 96% ethanol and 4% water was prepared. The pH value of the solution was adjusted to 5-6 with acetic acid. APTES was added to the solution to achieve a 2% (vol) concentration. The pre-cleaned glass slides (or silicon wafers) were immersed into this silane solution for 8 hours. After that, the slides were rinsed with ethanol and baked in the oven at 105 °C for 30 minutes.

Some early studies indicate that thinner layers of silane seem to give stronger and more durable adhesive bonds [74]. On the other hand, it is difficult to produce ordered single silane layers on substrates by this 'wet' coupling. The actual layer thickness can be up to 100 nm [75]. In order to obtain high quality APTES monolayers by the wet chemistry method, the pH value and amount of water in the solution must be precisely controlled [75]. The initial hydrolysis step is determined by the pH value. The absence of water results in incomplete monolayers, while

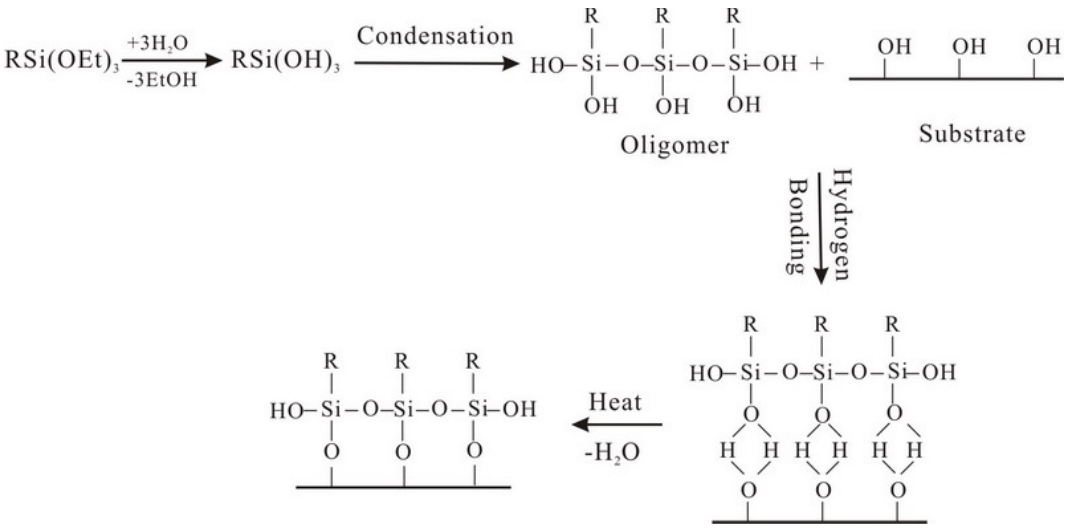


Figure 4.2: Reaction process of silane coating by the wet chemistry method.

excess water results in thicker layers or even unwanted polymerization in solution and physical deposition of polysiloxane on the surface, which makes the surface very inhomogeneous.

#### Chemical Vapor Deposition

As discussed above, water has great influence on the formation of the alkoxy silane layer. The disturbance of water can be avoided by using the chemical vapor deposition (CVD) method. The CVD method also eliminates many tedious operations in the alternative methods, such as the removal of toxic organic solvents and the control of the pH value.

First, an exsiccator and piranha activated glass slides were baked in an oven for 30 minutes at 105 °C, then the exsiccator was allowed to cool down in the extractor hood at room temperature. 1 mL APTES was added into a dried glass petri dish and placed at the bottom of the exsiccator. The activated glass slides, which were held vertically by a special glass holder (NeoLab), were put into the exsiccator, more than 5 cm above the liquid surface. After that, the exsiccator was tightly closed and $1 \times 10^{-2}$ mbar vacuum was applied in the chamber. After a certain deposition time at room temperature, the glass slides were removed from the exsiccator and were ultrasonicated in absolute ethanol for three minutes to remove the loosely physically adsorbed silane molecules. Finally, the slides were rinsed with absolute ethanol and dried by $N_2$ gas.

Three different deposition times, 1 hour, 5 hours and 24 hours, were tested to study the adsorption process. The surface analysis results from contact angle and XPS measurements are discussed in section 4.2.2.

### 4.1.3 Covalent Coupling of Polysaccharides

Glass slides coated with APTES are ready for the next polysaccharide coating step. This step is based on the formation of amide bonds between the amino groups on the substrate and the carboxyl groups in the acidic polysaccharide molecules. This covalent bonding is realized through the EDC (N-(3-Dimethylaminopropyl)-N'-ethylcarbodiimide, Hydrochloride) and NHS (N-Hydroxysuccinimide) chemistry. Carboxyl groups in the polysaccharide molecules first react with EDC to form the EDC-activated ester. But the disadvantage of this reaction is the fast hydrolysis of the EDC-ester. For this reason, NHS is added to form the NHS-ester. The NHS-ester is more stable in aqueous solution and also very active in coupling with amino groups [6]. The processes are shown in Figure 4.3.

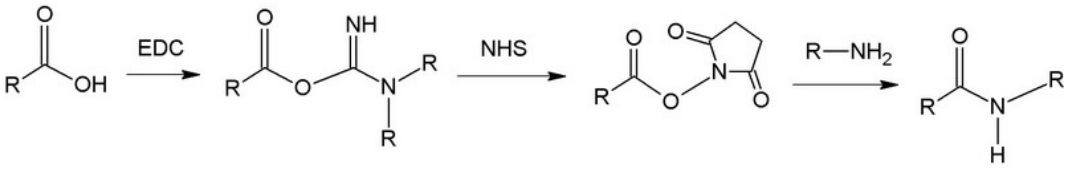


Figure 4.3: Covalent bonding between carboxyl group and amino group.

In the preparation, 0.1 M EDC and 0.05 M NHS were dissolved in 10 mM HEPES buffer solution (pH 6-7). Then the polysaccharide was dissolved in the solution to achieve a concentration of 1 mg/mL. The polysaccharides are very difficult to dissolve in buffer solution, especially AA and HA. When they are poured directly into the solution, the molecules quickly absorb water, swell and stick to each other, forming big clusters. These clusters are very difficult to break, even by ultrasonic treatment or heating. Therefore a special method was applied to dissolve the polysaccharides. First, polysaccharide powder was added into a dry beaker. Then a magnetic stir bar was put into the beaker and adjusted to a quite high rotation speed. Then the solution (HEPES buffer with EDC and NHS) was slowly added into the beaker while the stirrer bar was quickly stirring. In this way, the formation of big clusters can be effectively avoided. After 20 minutes of intensive stirring, a clear solution was obtained. Glass slides functionalized by APTES were soaked in the activated polysaccharide solution for 16 hours at room temperature while shaking on a vibrational table. Figure 4.4 shows the preparation process of polysaccharide coatings [76].

Finally, in order to remove the physically adsorbed polysaccharide molecules and the reactant such as EDC and NHS, the slides were rinsed and then immersed in millipore water while shaking on a vibrational table for five days. The water has to be exchanged every day.

Polysaccharides studied in this work are natural polymers, the molecular weights

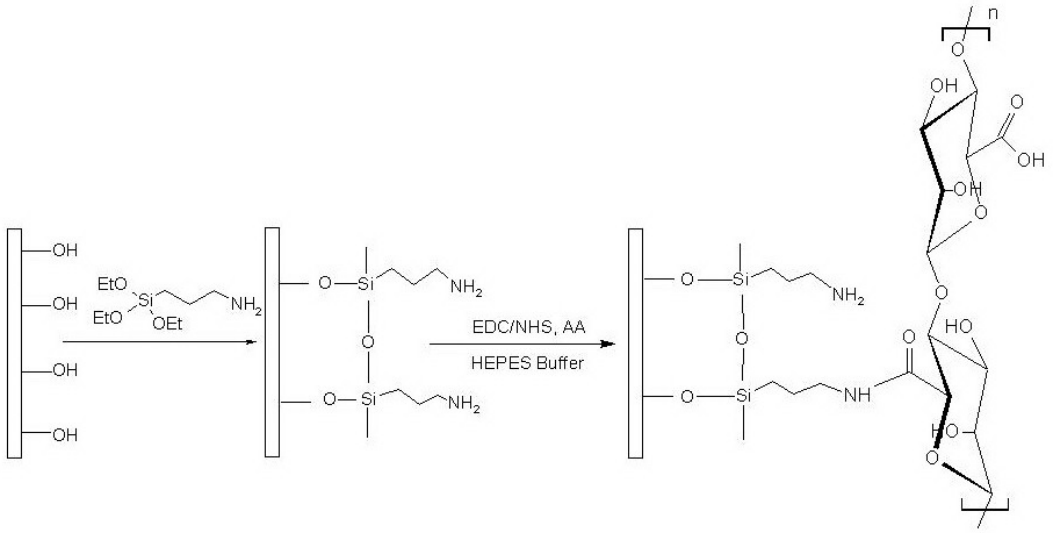


Figure 4.4: The process of polysaccharide coating.

range from tens to thousands kDa [5, 6, 77]. Due to the widely distributed and relatively long chain length, it is not possible to obtain highly ordered brushes of polysaccharides but rather a loose mesh or network of polymer strands. A lot of earlier studies reveal that inter- and intra-molecular hydrogen bonds are important in determining the structure and conformation of polysaccharides in solution [65]. Figure 4.5 shows the intramolecular hydrogen bonding in HA molecules. Due to these hydrogen bonds, a polysaccharide surface is probably a loose network of long chain molecules.

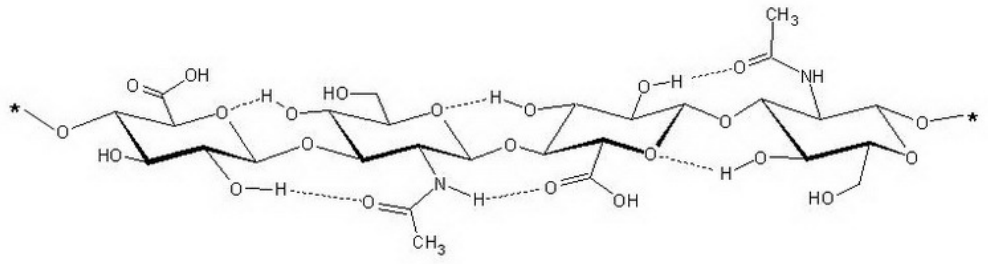


Figure 4.5: Hydrogen bonds within hyaluronic acid (HA) in solution (picture reproduced from [65]).

## 4.2 Surface Analysis of Polysaccharide Coatings

Several methods were applied to optimize the preparation of the polysaccharide coatings and the surface properties were analyzed qualitatively and quantitatively. The wettability of the silane layer and polysaccharide layers were characterized by

| Surface | Contact Angle(°) |
|---|---|
| Glass | $14.7 \pm 0.6$ |
| APTES | $53 - 63$ |
| AA | $20.4 \pm 1.8$ |
| HA | $< 10$ |
| PA | $18.2 \pm 0.5$ |

Table 4.1: Water contact angle of glass, APTES and polysaccharide surfaces.

contact angle measurements. The layer thickness was measured by ellipsometry and calculated from XPS data. The differences in the chemical composition of the silane and the three polysaccharides were also revealed in the XPS spectra.

### 4.2.1 Contact Angle Measurements

Contact angle measurement is a fast qualitative technique to investigate the formation of the aminosilane layer and the polysaccharide layer. After piranha cleaning, the surface is functionalized by hydroxyl groups, which make the surface very hydrophilic. When the APTES molecules are anchored onto the surface, the amino groups and the ordered alkane chain make the surface more hydrophobic and result in larger contact angles on the surface. After the polysaccharide is covalently coupled to the APTES layer, the surface is hydrophilic again due to the hydroxyl groups in the polysaccharide molecules. Comparing the three different polysaccharide coatings, HA yields the most hydrophilic surface. The contact angle of the HA coating is in agreement with former studies by Stile [78]. The measured contact angles of the glass, APTES and three polysaccharide surfaces are shown in Table 4.1.

### 4.2.2 Surface Analysis by XPS

#### Analysis of the APTES Layer

Three methods have been used to prepare the aminosilane layer. XPS analysis proved that all three methods were successful in forming a silane layer on the surface of glass and silicon wafers. Because of the simplicity and better reproducibility, the CVD method was applied as the standard method in the sample preparation.

Figure 4.6 and 4.7 shows the C1s and N1s XPS spectra of glass slides coated with APTES by CVD. The formation of the APTES layer can be clearly confirmed by the increase of the C1s peak and the N1s peak with increasing deposition time. The differences in peak intensity correspond to the different film coverage, which are related to the different deposition times. When the deposition time is longer, the APTES coverage on the surface is higher, which results in stronger C1s and N1s peaks. The contact angle of the surface increases from 42° (CVD 1h) to 57° (CVD 24h), which is also related to the coverage of the APTES molecules.

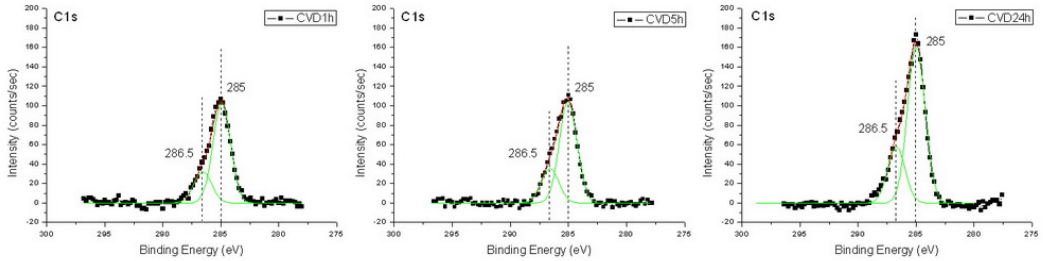


Figure 4.6: C1s XPS spectra for the APTES layers on glass, prepared by CVD.

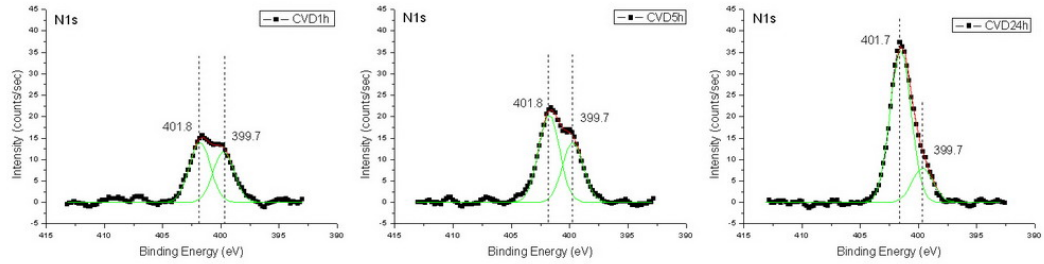


Figure 4.7: N1s XPS spectra for the APTES layers on glass, prepared by CVD.

The observed C1s peak of the APTES layer (Figure 4.6) consists of two sub-peaks at 285 eV and 286.5 eV, respectively. The peak at 285 eV comes from the alkyl carbon and the peak at 286.5 eV comes form carbon atoms in C-O or C-N bonds in the APTES molecules. The N1s peak is also a combination of two peaks as shown in Figure 4.7. According to the XPS handbook [79] and Stile's work [78], the peak at 401.7 eV comes from the protonated amines and the peak at 399.7 eV comes from the unprotonated amines.

The C/N elemental ratio can be calculated from C1s and N1s peak intensities through Equation 3.5. The peak intensities and the calculated C/N ratio of the APTES layer are shown in Table 4.2.

If the APTES molecules forms a monolayer as shown in Figure 4.8A, the C/N ratio should be about 3. But the calculated C/N ratio (in the range of 5-7) indicates that the APTES molecules are probably immobilized on the surface as shown in Figure 4.8B or 4.8C. Actually, after 24 hrs CVD at room temperature, the APTES layer coated on silicon wafer always shows a thickness in the range of 15-20 Å by ellipsometry measurement. The length of a APTES molecule is about 8 Å, therefore,

| Samples | C1s Intensity | N1s Intensity | C/N Ratio |
|---|---|---|---|
| **CVD1h** | 256.4 | 58.4 | 7,1 |
| **CVD5h** | 266.6 | 77.8 | 5.5 |
| **CVD24h** | 415.2 | 98.5 | 6.8 |

Table 4.2: C1s and N1s peak intensities and the calculated C/N ratio of the APTES layer on glass.

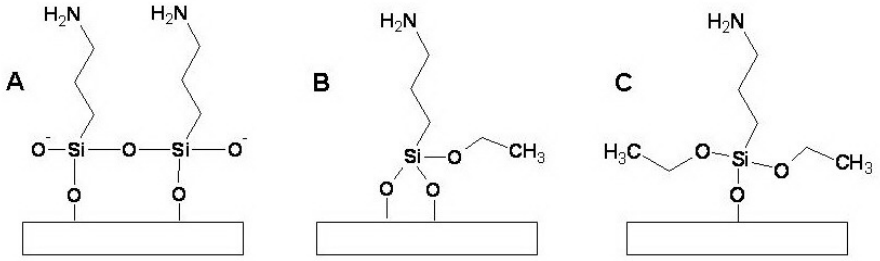


Figure 4.8: APTES molecules on a surface.

probably APTES multilayers are present.

The method to calculate the film thickness by the Lambert-Beer's law (Equation 3.8) is not suitable in this case. The glass substrate contains Si and O, and both elements are also presented in the APTES molecules. The Si2p and O1s peaks (Figure 4.9) consist of signals from both the substrate and the APTES layer, and they can not be distinguished. The deposition of APTES induces decrease of Si2p peak, because the atomic percentage of Si in the APTES molecules is much lower than in glass. For the same reason, the O1s peak also decreases due to the deposition of APTES, but the intensity change is not significant.

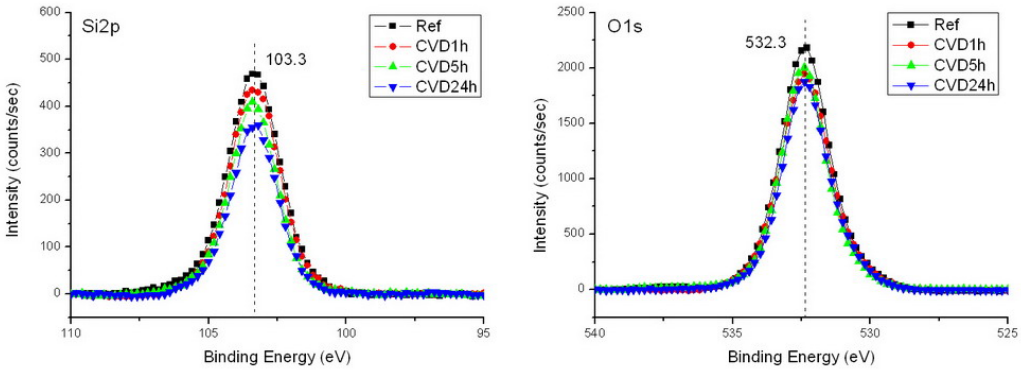


Figure 4.9: Si2p and O1s XPS spectra for APTES layers on glass, prepared by CVD.

**Analysis of Polysaccharide Coatings**

When the coatings are prepared on non-transparent substrates, like silicon wafers, the thickness of the coatings can be easily measured by ellipsometry. But if the coatings are prepared on transparent substrates, like glass slides, the reflection from the back side of the glass will interfere with the reflection from the surface, and correct results will not be accessible. For this reason, the thickness of the coatings on a silicon wafer was used to correlate XPS intensity and ellipsometry thickness.

In Figure 4.10, the Si2p and O1s signal are weakened after the coating of APTES

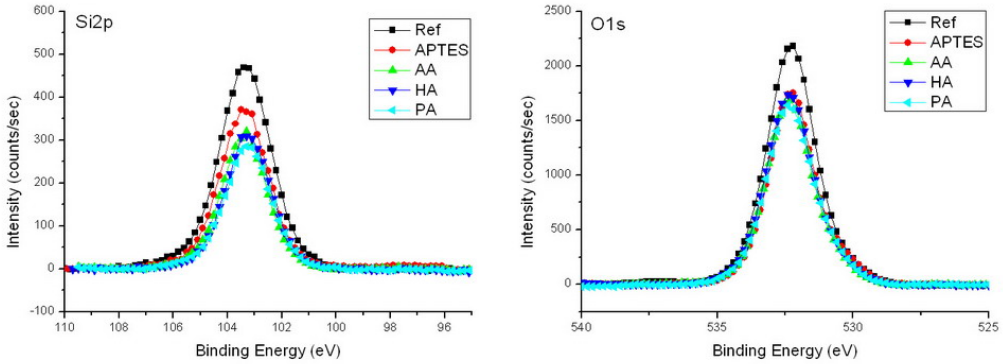


Figure 4.10: The attenuation of Si2p and O1s peaks after coating of APTES layer and polysaccharide layers on glass.

and polysaccharide films. As discussed above, the coatings also contain Si and O, Lambert-Beer's law (Equation 3.8) can not be applied to calculated the thickness of the APTES layer by considering the attenuation of Si or O signals.

Besides the theoretical method to calculate the polysaccharide film thickness by Lambert-Beer's law, an experimental method to calculate the thickness has been applied by considering the increased intensity of the C1s peak. In this method, a cross-calibration between the intensity of the XPS signal and the ellipsometry thickness was established. An APTES film and two AA films (coated on a Si-wafer) with different ellipsometry thicknesses were used as reference samples. The thickness of the AA film was controlled by the concentration of the AA in the buffer solution during the surface preparation. The C1s peak intensity on each reference sample was recorded by XPS. The data suggests a proportional relationship between the increase of the C1s peak intensity and the ellipsometry thickness of the AA film, as shown in Table 4.3 and Figure 4.11.

| **Sample** | **$\Delta A/A$** | **Film Thickness (Å)** |
|---|---|---|
| Reference AA1 | 0.53 | 14.3 |
| Reference AA2 | 1.44 | 37.1 |

Table 4.3: Calibration data from AA coated reference samples (prepared on Si-wafer).

A linear function is assumed:

$$\Delta A/A = k \cdot d \tag{4.1}$$

Here $A$ is the C1s peak area (or intensity) of the APTES layer. $\Delta A$ is the C1s peak area difference between the polysaccharide and APTES layer. $d$ is the ellipsometry thickness of the film, $k$ is an experimental constant, which can be determined by the calibration curve.

Knowing the value of $k$ ($\approx 0.04$) and $\Delta A/A$ (obtained from the C1s XPS spec-

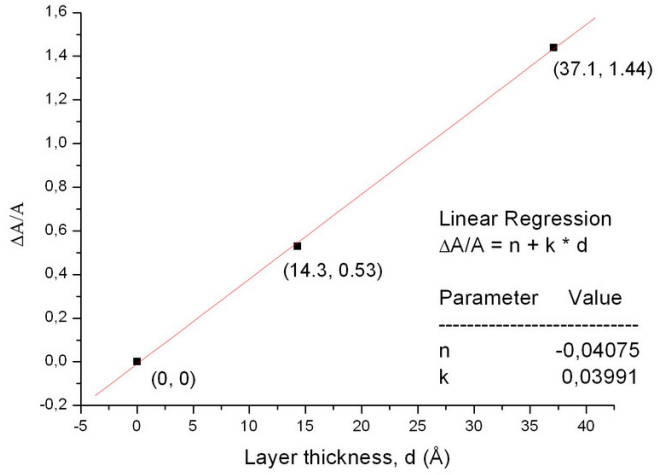


Figure 4.11: Calibration curve between XPS peak intensity and ellipsometry thickness.

trum), the thickness of the polysaccharide coating on glass slides can be determined using Equation 4.2:

$$d = (\Delta A/A)/k \tag{4.2}$$

The successful coupling of polysaccharide layers are clearly proven by the intensity increase of the C1s peaks in Figure 4.12. The areas of C1s peaks are calculated to determine the film thickness by using Equation 4.2, results are shown in Table 4.4.

| Surfaces | Peak Area | ΔA/A | Film Thickness (Å) |
|---|---|---|---|
| **APTES** | 314.1 | 0 | n.a. |
| **AA** | 568.2 | 0.81 | 20.3 |
| **HA** | 572.5 | 0.82 | 20.5 |
| **PA** | 669.5 | 1.13 | 28.3 |

Table 4.4: Film thickness calculated by the increase of C1s peaks (coatings are deposited on glass).

The results confirm an expected film thickness of about 2-3 nm. Slight inhomogeneities on the surface might cause some deviation of the film thickness in the range of 2-3 Å. The coverage of APTES on the substrate has a strong effect on the thickness (or coverage) of the polysaccharides films.

The C1s peaks in Figure 4.12 show a broadening after the coupling of polysaccharide. The carbon atoms in polysaccharide molecules are in different chemical environments, which cause different chemical shifts in the XPS spectrum. The broad and asymmetric C1s peak is actually a combination of several sharp and symmetric peaks with different chemical shifts. The assignment of the peaks is given in Table 4.5. The XPS handbook [79] and the NIST (National Institute of Standard and Technology) XPS online database [80] are used as references. Since there are many C-O bonds in the polysaccharide molecules, the peak at 286.5 eV is the most

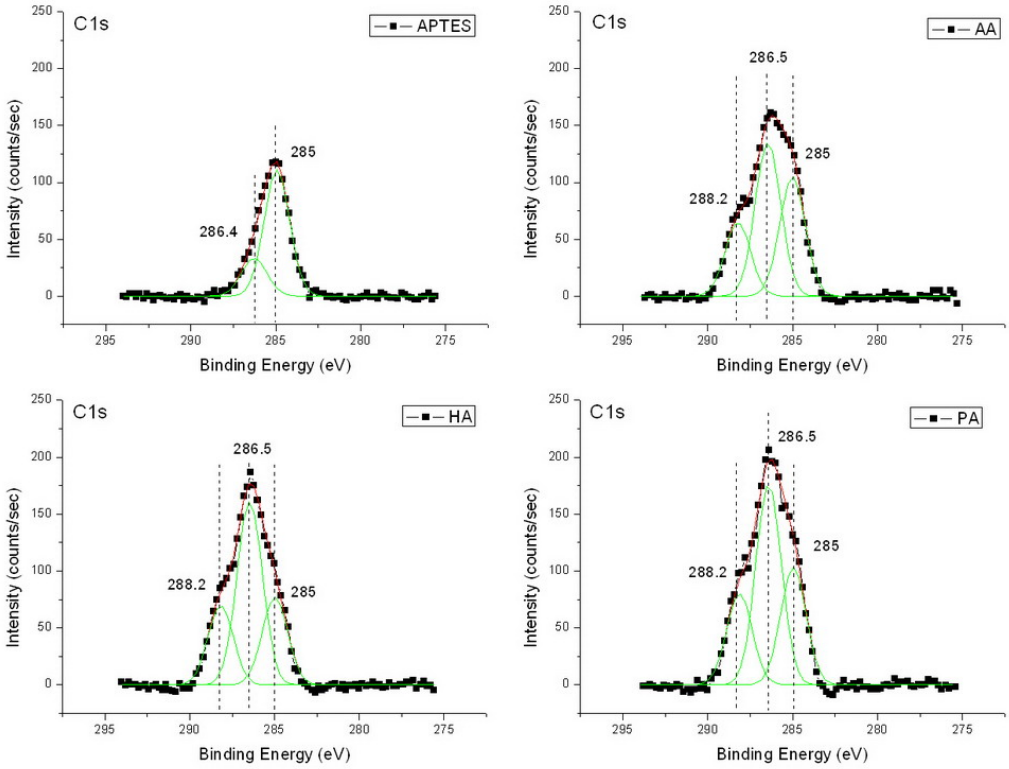


Figure 4.12: C1s XPS spectra of APTES coating and three polysaccharide coatings on glass.

| Peak Position (eV) | Origin |
|---|---|
| 285 | C-C, C-H |
| 286.5 | C-O, C-N |
| 288.2 | O-C=O, N-C=O, O-C-O |

Table 4.5: Peak assignment of C1s peak in peak fitting.

prominent signal. The peak fitting results are in agreement with Stile's former study [78].

the peak at 285 eV mainly comes from the APTES layer. The peaks at 286.5 eV and 288.2 eV come from polysaccharide molecules. The intensity ratio of the two peaks at 286.5 eV and 288.2 eV reveals the stoichiometry of the polysaccharide molecules. Results are shown in Table 4.6. The calculated results are in good agreement with the theoretical values.

| Polysaccharides | C(286.4)/C(288.2) | Theoretical Value |
|---|---|---|
| **AA** | 2.08 | 2.0 |
| **HA** | 2.32 | 2.25 |
| **PA** | 2.20 | 2.0 |

Table 4.6: Stoichiometry of the polysaccharide molecules.

After the coupling polysaccharide onto the surface, the O1s signal is also slightly changed. In Figure 4.13, the dominating peak at 532.4 eV comes from the glass

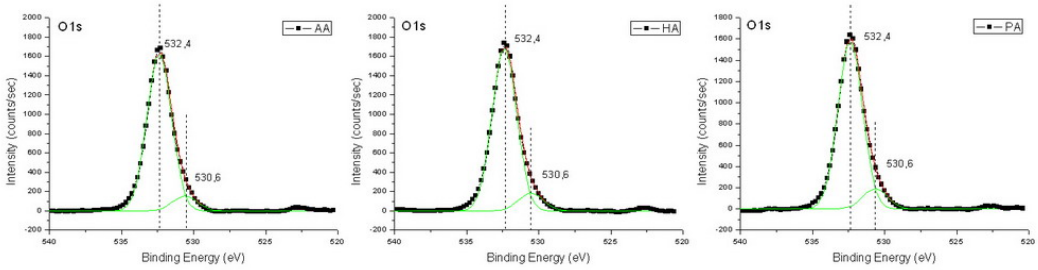


Figure 4.13: O1s XPS spectra of three polysaccharide coatings on glass.

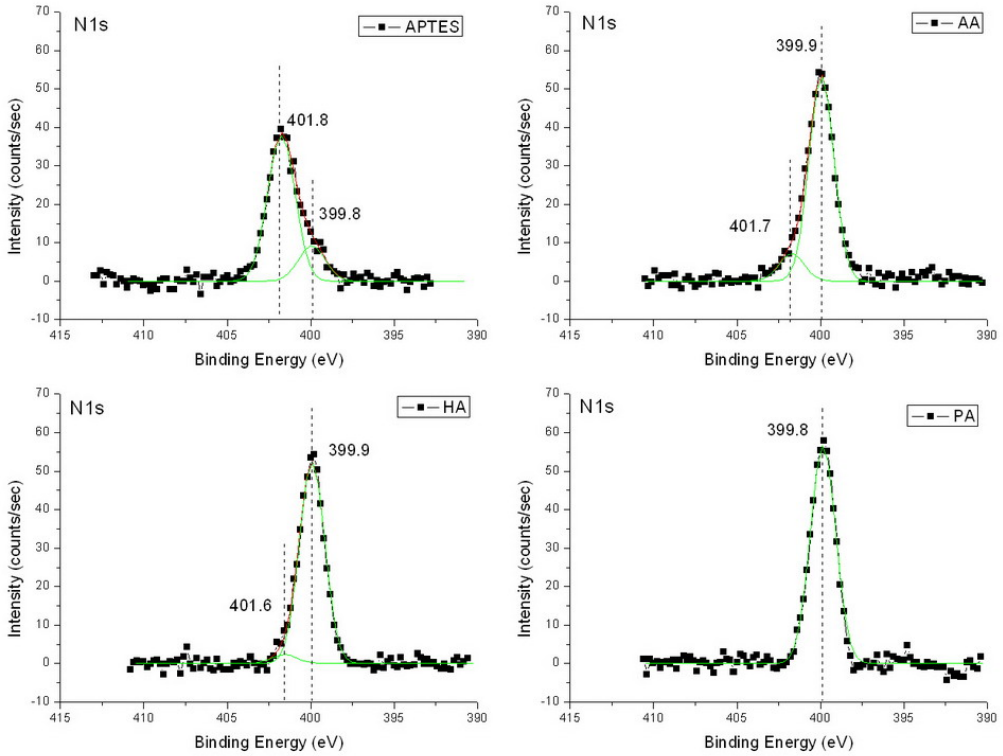


Figure 4.14: N1s XPS spectra of APTES coating and three polysaccharide coatings on glass.

substrate and the small peak at 530.6 eV is the signal from polysaccharide molecules.

The shift of the N1s peak gives a proof of the formation of amide bonds between the amino groups and carboxyl groups. After the polysaccharide coupling, the signal of protonated amines (at 401.8 eV) is decreased and the amide signal (at 399.9 eV) is increased. Another interesting observation is that the intensity of the N1s signal is not decreased but slightly increased after the polysaccharide coupling, although there are no nitrogen in AA and PA molecules at all. The covalent bonding between the APTES and polysaccharides is realized through the EDC/NHS reaction, and both EDC and NHS contain nitrogen. The increase of the N1s peak might be induced by the EDC and NHS molecules which have not been completely removed from the surface. The residues of EDC and NHS molecules on the surface (or in the

film) must also have contributions to the C1s and O1s signals in the XPS spectra.

## 4.3 Protein Adsorption on Polysaccharide Surfaces

### 4.3.1 Protein Adsorption Experiments

In order to characterize the general affinity of the polysaccharides towards biomacromolecules, their abilities to resist adsorption of proteins were tested. Polysaccharide coatings prepared on silicon wafers were used for the adsorption tests of four proteins, albumin (from bovine serum, $\geq 96\%$), fibrinogen (from bovine plasma, 55-70% protein, $\geq$ 90% clottable protein), lysozyme (from chicken egg white, 85%, 50000 units/mg protein), and pyruvate kinase (from rabbit muscle, 400-800 units/mg protein). These proteins were purchased from Sigma-Aldrich, Germany. These proteins have different molecular weights and net charges in PBS buffer solution, as listed in Table 4.7). The isoelectric point and net charge of proteins are obtained from the ExPASy (Expert Protein Analysis System) proteomics server of the Swiss institute of bioinformatics [81]. 1-Dodecanethiol SAM on a gold surface was used as non-protein resistant reference for fibrinogen and lysozyme adsorption. Ellipsometry measurements were used to determine the amount of adsorbed protein.

| **Proteins** | **From** | **Molecular Weight**(kDa) | **Isoelectric Point** | **Net Charge** |
|---|---|---|---|---|
| Albumin | bovine serum | 66 | 5.60 | - |
| Fibrinogen | bovine plasma | 340 | $\alpha$ 7.73<br>$\beta$ 8.66<br>$\gamma$ 5.47 | - |
| Lysozyme | chicken egg white | 14.7 | 9.32 | + |
| Pyruvate Kinase | rabbit muscle | 237 | 7.60 | + |

Table 4.7: Properties of the chosen proteins [81].

The protein adsorption test was performed following the protocol reported in Prime's [82] and Herrwerth's [83] earlier work. First, the protein was dissolved in PBS buffer solution. In the albumin, fibrinogen and lysozyme assays, the concentration of protein solution was 1 mg/mL. In the pyruvate kinase assay, the concentration was 80 units/mL. Second, the polysaccharide coated Si-wafer was placed at the bottom of a beaker and 5 mL PBS buffer was added to cover the sample. After 15 minutes, 10 mL protein solution was added to the beaker to immerse the sample for two hours at room temperature. Finally, the protein solution was greatly diluted by a large amount of millipore water. The sample was picked out and dried by $N_2$ gas.

The thickness of the polysaccharide films was determined by ellipsometry before and after the protein adsorption test. The adsorption of protein on the surface resulted in an increase of the film thickness. To get better statistics, the film thickness

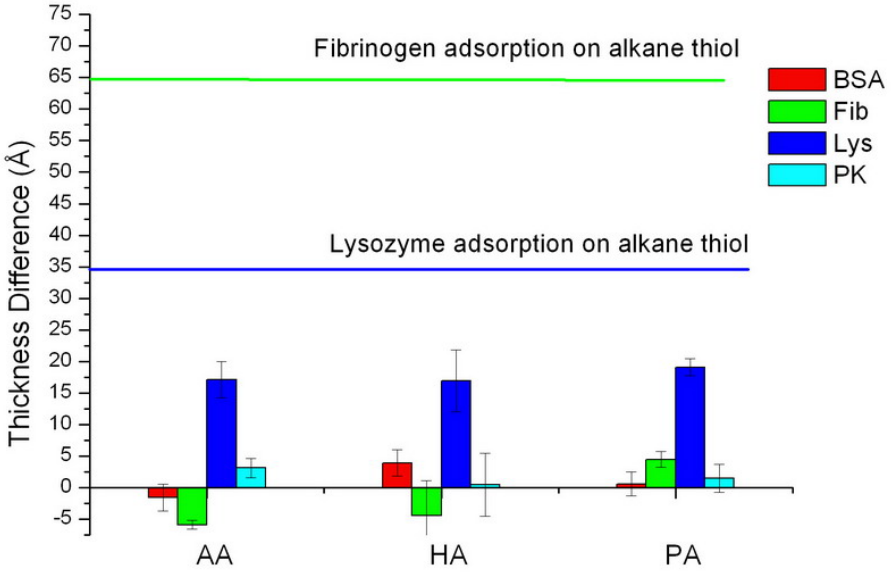


Figure 4.15: Protein adsorption on three polysacchairde coatings.

was measured at three different spots on each sample. The average value and the error were calculated. The results are plotted in Figure 4.15. Protein adsorptions on the 1-Dodecanethiol monolayer reference are shown as horizontal bars.

After the albumin and pyruvate kinase adsorption tests on the polysaccharides surfaces, the film thickness differences are very small ($< 5$ Å). Therefore, the three polysaccharide surfaces are resistant to the adsorption of albumin and pyruvate kinase. The adsorption of fibrinogen and lysozyme on 1-Dodecanethiol SAM results in a thickness increase of 65 Å and 35 Å, respectively. Compared to the alkane thiol reference, almost no adsorption of fibrinogen can be observed on polysaccharide surfaces. The thickness decrease of AA and HA films (about 5 Å) after the fibrinogen adsorption test might due to a small amount of material removal from the surfaces, such as the removal of physically adsorbed polysaccharides or EDC and NHS residues. The adsorption of lysozyme on the polysaccharide surfaces results in about 17 Å increase in film thickness. Although the thickness of adsorbed lysozyme is only half of the one observed for alkane thiols, the amount sticking on the polysaccharides is significant. Due to the carboxyl groups, the polysaccharide coatings are negatively charged in PBS buffer (pH 7.4). Therefore, negatively charged proteins like albumin and fibrinogen are unlikely to adsorb on the polysaccharide surfaces due to the electrostatic repulsion. Pyruvate kinase in contrast is slightly positively charged but still does not stick to the surface. Due to the big molecular size, steric effects might be responsible for the resistance of the polysaccharide surfaces. Lysozyme is also positively charged and the size is small, these characteristics might enable the lysozyme molecules to stick on the polysaccharide surfaces.

Two models are considered to explain the adsorption of lysozyme on polysaccharide surfaces (as shown in Figure 4.16). In model A, the positively charged lysozyme molecules are attracted by the negatively charged polysaccharide surface and adsorb on top of the surface. In model B, the opposite charge attraction together with the small molecular size enable the lysozyme to penetrate into the loose network of the polysaccharide layer and thereby to stick to the coating.

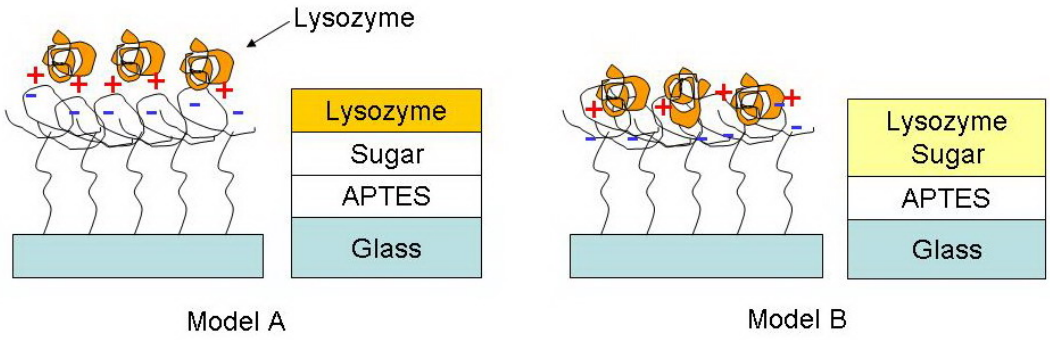


Figure 4.16: Two models to explain the adsorption of lysozyme on polysaccharide surfaces.

The lysozyme adsorption induced increase of the film thickness on polysaccharide surfaces is only half of the thickness increase on the alkane thiol reference (see Figure 4.15). This fact can be considered as an evidence for the penetration of lysozyme molecules into the polysaccharide film.

Based on this analysis, the take-off angle XPS data indicate that the adsorbed lysozyme is not located completely on top of the polysaccharide. Lysozyme molecules probably penetrate into the polysaccharide film but not through it. Therefore the origin of the observed affinity is due to the interaction between the polysaccharide and the protein. The penetration into the topmost layers of the loose polysaccharide 'mesh' network might enhance electrostatic interaction between lysozyme and polysaccharide which ultimately allows the lysozyme to stick. The limited amount of lysozyme on the surface could then be explained by the restricted numbers of meshes available for partial penetration by the protein. The mesh size itself might play a role for the observed size dependence and explain why pyruvate kinase is unable to stick to the surface.

### 4.3.2 Calcium Adsorption on Polysaccharide Surfaces

Because of its importance in modulating the interactions between polysaccharide and protein, special interest has been focused on binding of calcium with polyanions [65]. Experiments to study the calcium adsorption on polysaccharide surfaces and its influence on protein adsorption have been performed. The experimental procedure is schematically shown in Figure 4.17.

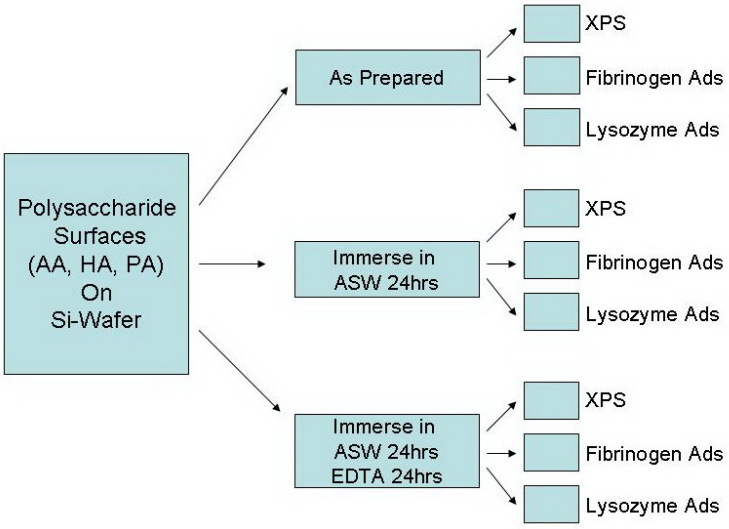


Figure 4.17: Experiments to study the adsorption of calcium on polysaccharide surfaces and its influence on protein adsorption.

| **Salts** | **Concentration (g/L)** |
|---|---|
| NaCl | 23.9 |
| $Na_2SO_4$ | 4 |
| KCl | 0.67 |
| $NaHCO_3$ | 0.2 |
| KBr | 0.1 |
| $MgCl_2 \cdot 6H_2O$ | 10.8 |
| $CaCl_2 \cdot 2H_2O$ | 1.47 |

Table 4.8: Contents of artificial seawater [84].

The three polysaccharides AA, HA and PA were covalently coupled to silicon wafers. Each sample was cut into 3 pieces. The first piece was kept as prepared, the second one was immersed into artificial seawater (ASW) for 24 hours, and the third one was immersed in ASW for 24 hours and subsequently immersed in EDTA solution (0.1 mol/L) for another 24 hours. Afterwards all three samples were washed with millipore water and dried by $N_2$ gas. Then the three samples were cut into smaller pieces for XPS measurements and protein adsorption tests.

We did not use any commercial ASW, because the macromolecules (e. g. vitamins) in some commercial ASW might adsorb on the surfaces and interfere the experiments. Instead, artificial seawater used in this experiment is a mixture of dissolved mineral salts as listed in Table 4.8 [84].

The XPS results show that $Ca^{2+}$ adsorption occurs on polysaccharide coatings. A XPS survey spectrum (Figure 4.18) of AA after 24 hours immersion in ASW is shown as an example. In this spectrum we can find that besides the C, O and N signals from the organic film and the Si signal from the substrate, there are only Ca signals present. Though the concentration of $Na^+$ and $Cl^-$ ions in ASW are much

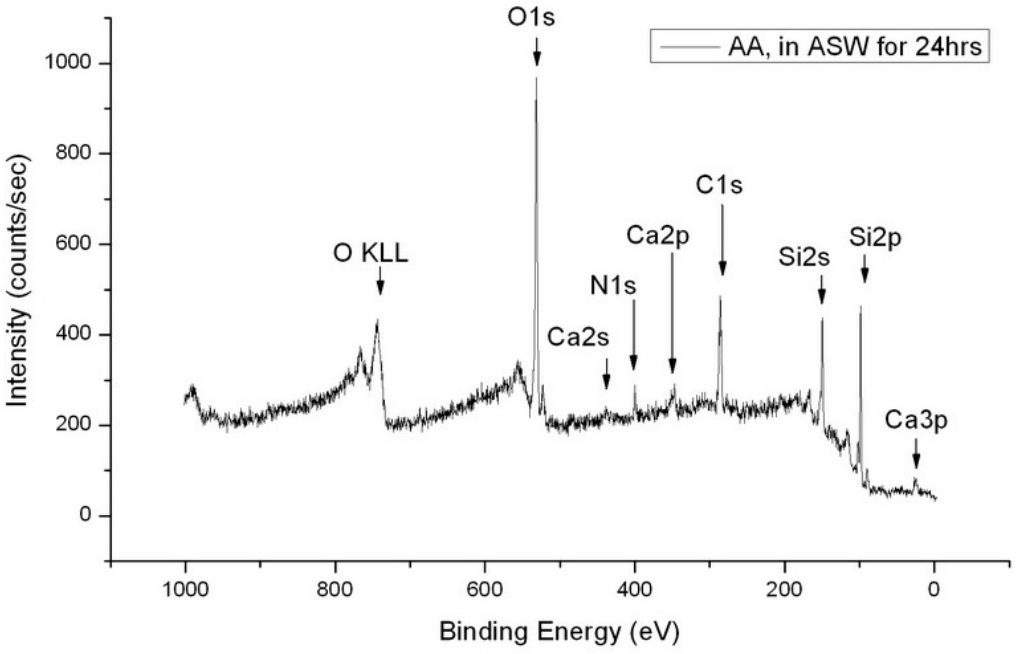


Figure 4.18: XPS survey spectrum of alginic acid (AA), after 24 hours immersion in artificial seawater.

higher than $Ca^{2+}$ (Table 4.8), signals of Na (Na KLL at 263.5 eV)and Cl (Cl2p at 198 eV) are not observable in the spectrum, which means $Na^{+}$ and $Cl^{-}$ ions do not strongly interact with the covalently immobilized polysaccharide molecules. According to the literature [85], the binding affinity of Mg towards polysaccharides is much weaker than Ca. Therefore, the Mg signal (Mg KLL at 300.9 eV) is also invisible in the spectrum (Figure 4.18), though the concentration of $Mg^{2+}$ is higher than $Ca^{2+}$ in ASW.

Figure 4.19 shows the narrow scans of the Ca2p and C1s peaks on AA, HA and PA surfaces. The spin-orbital coupling causes the multiplet splitting of the Ca2p peak (as described in chapter 3). The $2p$ orbital splits into two energy states, $2p_{1/2}$ and $2p_{3/2}$, and consequently a doublet is observed in the XPS spectrum. The detected Ca2p signals from the polysaccharide surfaces confirm $Ca^{2+}$ adsorption. Furthermore the differences in peak intensity also reveal that the adsorption on AA and PA is much higher than on HA. There might be some very weak Ca2p signal from the HA surface (indicated by the arrows), but the intensity is so low that it is difficult to distinguish the peaks from the background noise.

Fewer -COOH groups in the repeating units of HA molecules than in AA and PA molecules might be a reason for the weak $Ca^{2+}$ adsorption. But, according to Braccini's work [66, 86], the calcium binding to ionic polysaccharides is not only through electrostatic interactions between the cations and the carboxyl groups, but also through highly specific interactions related to the conformation of the polysaccharide

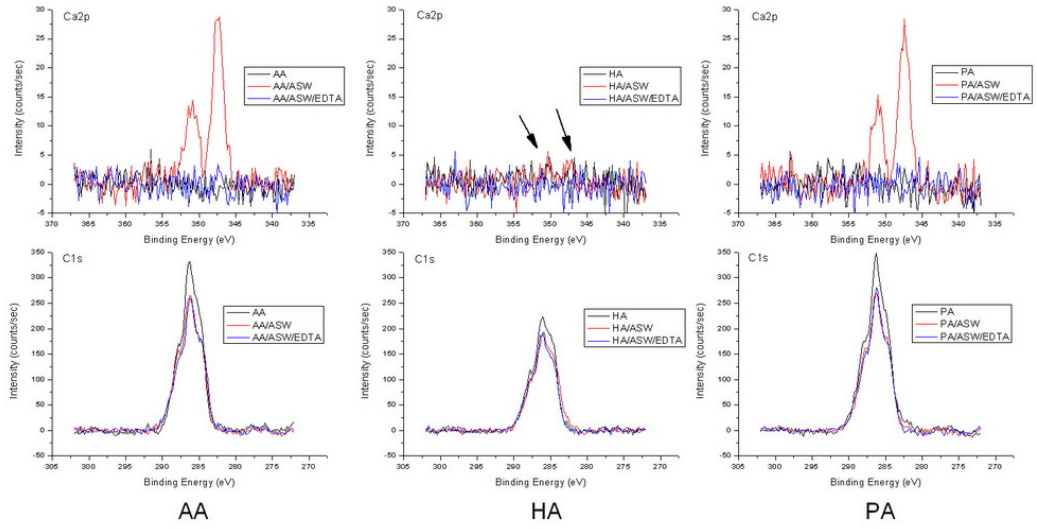


Figure 4.19: Calcium adsorption on polysaccharide surfaces studied by XPS.

| **Surfaces** | $I_{Ca2p}$ | $I_{C1s}$ | $I_{Ca2p}/I_{C1s} \times 100$ |
|---|---|---|---|
| **AA** immersion in ASW 24hrs | 83.2 | 971.1 | 8.6 |
| **HA** immersion in ASW 24hrs | N.A. | 725.5 | N.A. |
| **PA** immersion in ASW 24hrs | 75.6 | 981.1 | 7.7 |

Table 4.9: Intensity of Ca2p peak and C1s peak, and the intensity ratio between Ca2p and C1s peak.

chains. Calcium preferentially binds to the corrugated $\alpha$-$(1 \rightarrow 4)$-linked polysaccharide chains (e. g. PA and 'G units' in AA) rather than the linear $\beta$-$(1 \rightarrow 4)$-linked polysaccharide chains (e. g. HA and 'M units' in AA) [66, 86].

Besides the differences in the intensities of the Ca2p peaks, the intensities of the C1s peaks from the three polysaccharide coatings are also different (as shown in Figure 4.19), which indicates the differences in film thickness or coverage. Therefore, the peak intensity ratio $I_{Ca2p}/I_{C1s}$ is used to determine which polysaccharide surface adsorbs more calcium. The results in Table 4.9 indicate that AA surface adsorbs more calcium than PA surface, but the difference is not significant. Since the intensity of the Ca2p peak on the HA surface (after 24hrs immersion in ASW) is too low to be detected, we assume that there is no calcium adsorption on HA surface.

The adsorbed $Ca^{2+}$ ions can be removed by EDTA solution, because EDTA forms a more stable complex with $Ca^{2+}$ cations (Figure 4.20). This removal is proven by the XPS spectra in Figure 4.19. The Ca2p peak disappears after the 24 hours immersion in EDTA.

Fibrinogen and lysozyme adsorption tests were performed after 24 hours immersion in ASW to determine if the adsorbed calcium has any influence on protein adsorption. The results are shown in Figure 4.21. The freshly prepared polysaccha-

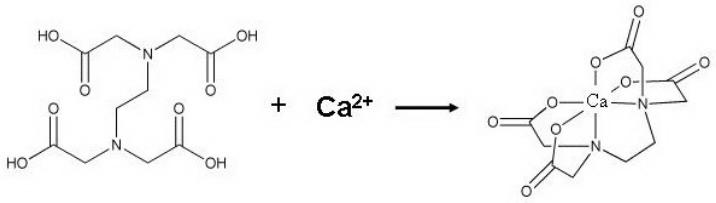


Figure 4.20: EDTA reacts with calcium to form a stable complex [65].

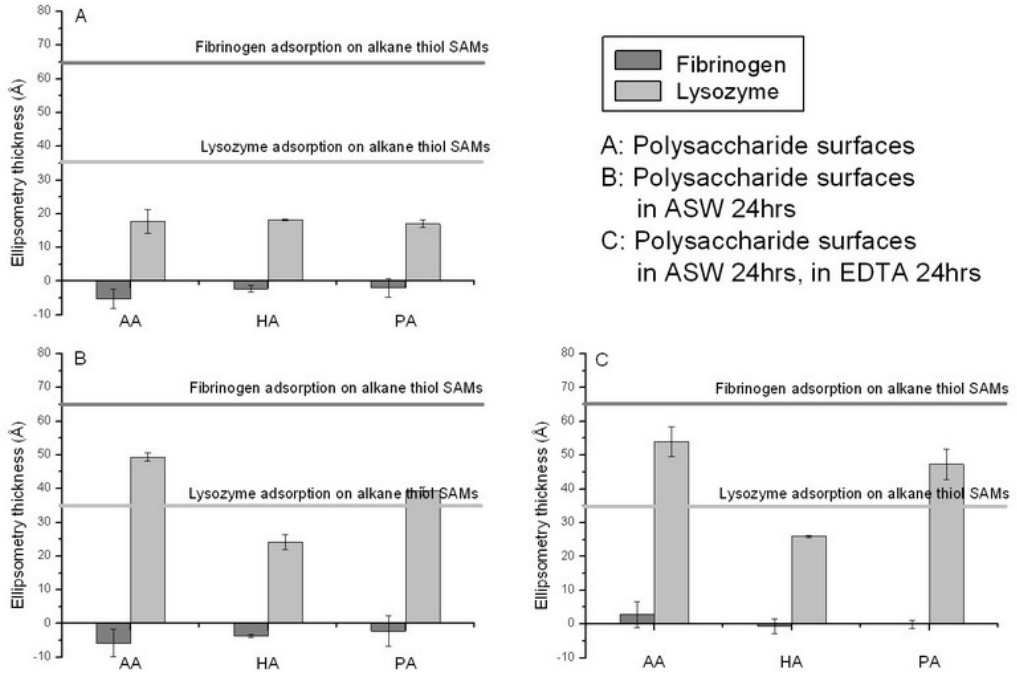


Figure 4.21: Fibrinogen and lysozyme adsorption on polysaccharide surfaces: the influence of calcium.

ride surfaces are resistant to fibrinogen adsorption but not to lysozyme adsorption, which causes about 20 Å increase in film thickness (Figure 4.21A). Compared to the protein adsorption test results in Figure 4.15, this result is reproducible. After $Ca^{2+}$ adsorption from ASW, the lysozyme adsorption on AA and PA is greatly increased and the adsorption on HA is only slightly increased. All three surfaces are still resistant to fibrinogen adsorption. When the adsorbed $Ca^{2+}$ is removed by EDTA, the lysozyme adsorption on AA and PA surfaces is still much higher than on the freshly prepared surfaces. It seems that the adsorption of calcium on polysaccharide surfaces has only a strong influence on lysozyme adsorption. Since there is more $Ca^{2+}$ bound to AA and PA than to HA, the influence on lysozyme adsorption of AA and PA surfaces is much stronger than for the HA surface. The calcium adsorption has no effect on the resistance of the three polysaccharide surfaces towards fibrinogen.

The C1s XPS spectra in Figure 4.19 show that the C1s peak decreases after 24

hour immersion in ASW. Quantitative calculation show that the intensity decrease is about 15%. This decrease probably indicates film desorption from the substrate to some extent as a result of hydrolysis in ASW (pH $\approx$ 7.8) or it could also be due to the removal of EDC and NHS residues in the coatings. After immersion in ASW, all three polysaccharide coatings show nearly the same amount of desorption (as shown in Figure 4.19), but the strong increase in lysozyme adsorption is only associtated with AA and PA surfaces, the lysozyme adsorption on HA surface is almost unchanged (Figure 4.21B). Therefore, the observed changes in lysozyme resistance are unlikely due to film desorption but rather induced by the calcium adsorption. The adsorbed $Ca^{2+}$ ions induce chain-chain interactions [87] and probably impact the network of the polysaccharide layer. As a result, there might be more sites suitable for immobilization of lysozyme molecules. This conformational change seems to be permanent, since the effect on lysozyme resistance is not reversible after the removal of calcium by EDTA.

## 4.4 Cell Adhesion on Polysaccharide Surfaces

Earlier studies about the interactions between polysaccharide surfaces and cells indicates that polysaccharide surfaces such as AA and HA are resistant to the adhesion of cells [6, 36]. In this work, the adhesion tests of the stem cells KG1a and Jurkat on the three polysaccharide coatings were performed in collaboration with Dr. Wagner form Otto-Meyerhof center (Medical department, University of Heidelberg). The medium for cell culture is RPMI-1640 with 10% FCS (Fetal Calf Serum), 5% glutamin and 5% penicillin/streptomycin.

A leak-proof silicone gasket with 4 wells (9 mm in diameter and 1 mm in depth) was fixed on the polysaccharide surface. Cell suspension was added to the wells,

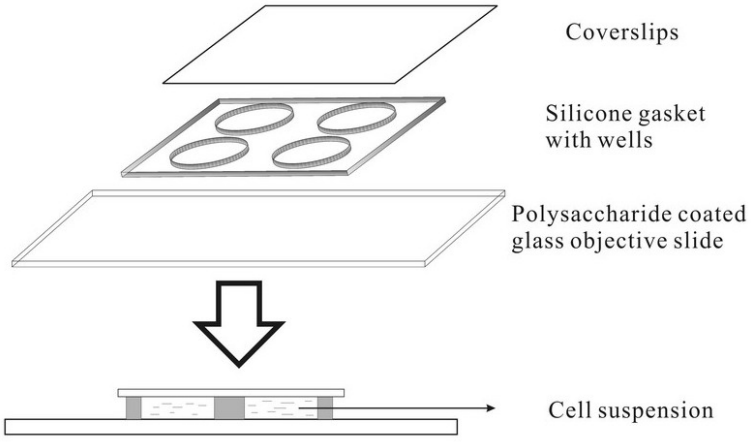


Figure 4.22: Cell attachment experiments on polysaccharide surfaces.

the concentration was 10000 cells/well. Then the cells were kept in the incubator (with 5% $CO_2$) at 37 °C for one hour. After that, a glass coverslip was put on top of the silicone gasket to cover the cell suspension. In this way, a 'sandwich' system with glass/cells/polysaccharide was established (as shown in Figure 4.22). Then the 'sandwich' system was turned up-side down and the cells that did not adhere on the polysaccharide surface could fall down to the glass surface by gravity. The cells were incubated for another 15 minutes. Finally, the samples were investigated under a light microscope and photos were taken for quantitative analysis.

The microscopic images of KG1a cell adhesion on glass surface and polysaccharide surfaces are shown in Figure 4.23. The bright spots in the images are adhered cells, the magnification and thus the field of view are the same in all images. On the polysaccharide surfaces almost no adhered cells can be observed, which clearly indicates that these surfaces are highly cell-resistant compared to glass surfaces. The blurry bright areas visible in the images of polysaccharide surfaces are actually induced by the adhered cells on the glass surface, which is only 1 mm away from the polysaccharide surfaces. Jurkat cells show a very similar adhesion behavior as KG1a.

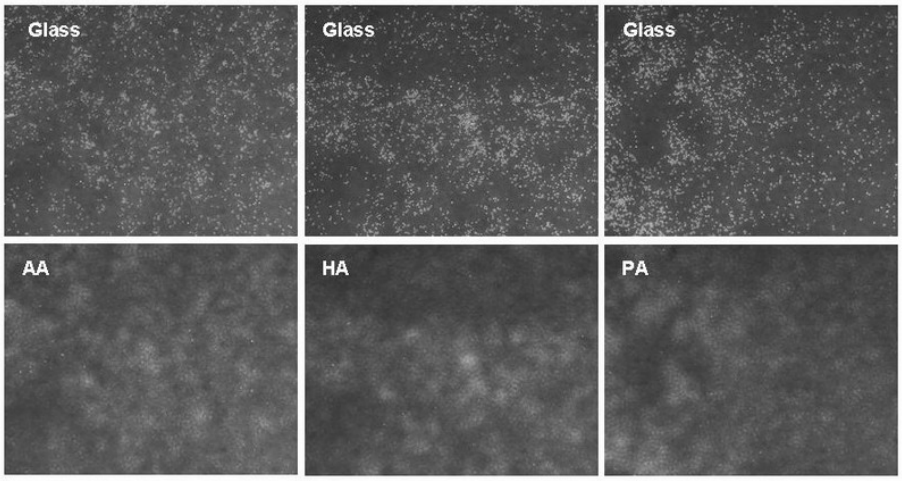


Figure 4.23: Light microscopic images of KG1a cell adhesion on glass and polysaccharide surfaces.

Adhered cells on glass and on polysaccharide surfaces were counted. The result reveals that the adhered cells on the polysaccharide surfaces are less than 2% of the adhered cells on glass surfaces (Figure 4.24). There are no differences between the three polysaccharide surfaces. Therefore, the three polysaccharide coatings are considered to be highly resistant to cell adhesion. These results are in agreement with the work of Morra [36, 5].

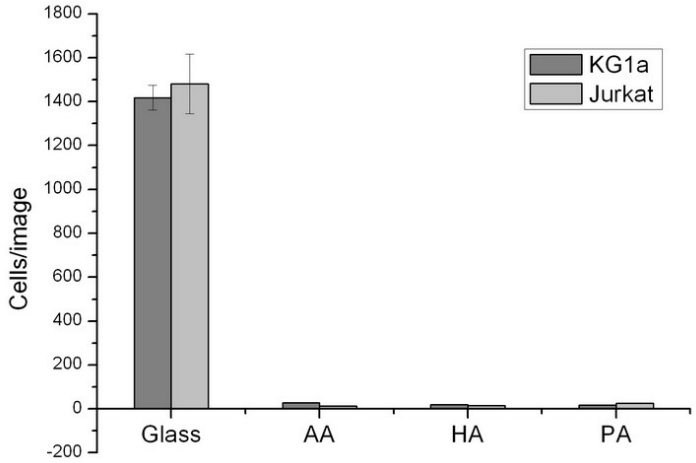


Figure 4.24: Comparison of KG1a and Jurkat cell adhesion on glass and polysaccharide surfaces.

## 4.5 Stability of the Polysaccharide Surfaces

As introduced in section 3.7 about the methods of biological evaluations, in order to determine the adhesion strength of attached *Ulva linza* spores, samples were exposed to a 51 Pa shear stress in a water flow channel. It is worthwhile to test if bonding between the polysaccharide film and the substrate is stable enough during this release assay. Therefore, two sets of polysaccharide surfaces were prepared. one set of samples were kept as prepared and the other set were sent to the partners in the University of Birmingham for the spores attachment and release assay and then sent back. XPS was used to examine the surfaces of both sets of samples. The comparisons between the C1s peak of HA surface and C1s peak of the HA surface after the spores attachment and release assay are shown in Figure 4.25.

If the polysaccharide surface is removed by the 51 Pa shear stress in the release assay, the C1s peak must be decreased. But as shown in Figure 4.25A, the C1s peak of the HA surface is obviously increased after the spore attachment and release assay, which indicates that the polysaccharide film is preserved on the substrate. The increase of the C1s peak is probably due to the adsorbed macromolecules from the seawater and remaining spores and/or adhesive on the surface.

A glass slide without any coatings was used as the reference sample in the spores attachment and release assay. If we compare the C1s peaks of the HA surface and glass surface after the assay (as shown in Figure 4.25B), it is clear that after the assay, the C1s peak of the HA surface is stronger than the C1s peak of the glass surface, which indicates that besides the adsorbed macromolecules and remaining spores on the surface, the HA molecules also contribute to the C1s peak. This can be considered as another evidence that the polysaccharide film is stable during the assay.

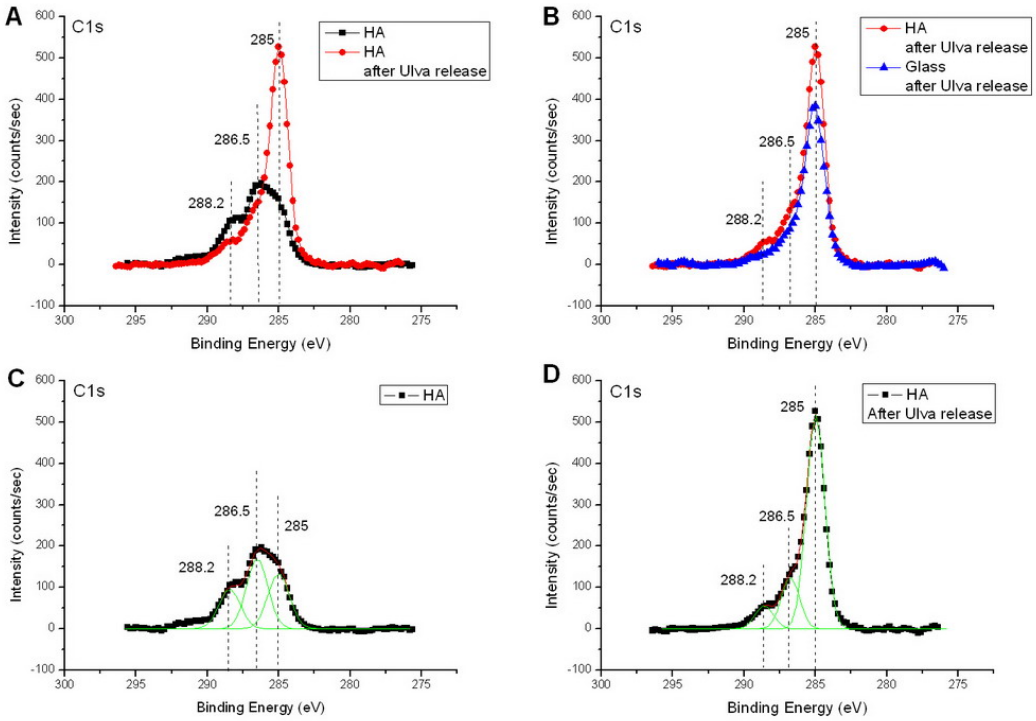


Figure 4.25: XPS comparions between the HA surface and the HA surface after spores attachment and release assay.

Detailed analysis about the C1s peak of HA surface are shown in Figure 4.25C and D. The assignment of the sub-peaks can be found in Table 4.5. Due to the adsorbed macromolecules from seawater and remained spores on the surface, the peak at 285 eV is greatly increased after the spores attachment and release assay. And also due to these adsorbed macromolecules and spores, the signals mainly from the polysaccharide surface (peaks at 286.5 eV and 288.2 eV) are obviously attenuated.

Compared to the HA surface, the changes in the XPS spectra of the AA and PA surfaces are very similar, which indicates that the AA and PA surfaces are as stable as the HA surface under the exposure to the 51 Pa shear stress in the release assay. Since the spectra are very similar, they are not shown here any more.

## 4.6 Biological Evaluation Results

As mentioned in chapter 2 and at the beginning of this chapter, biological evaluations to test the anti-fouling and foul-release properties of the polysaccharide surfaces against freshwater and marine bacteria, diatom, the green macroalga *Ulva linza* and the hard macrofouling invertebrates barnacle (*Balanus amphitrite*) were performed by the AMBIO project partners. The evaluation methods are introduced

in section 3.7.

### 4.6.1 Freshwater Bacterium

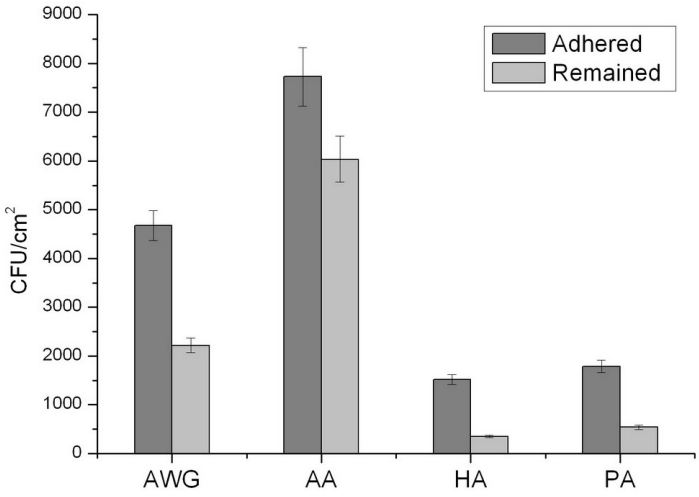


Figure 4.26: Biofilm formation of *Pseudomonas fluorescens* on polysaccharide surfaces.

Figure 4.26 shows the result for biofilm formation of *Pseudomonas fluorescens* on the polysaccharide coatings. Compared to the acid washed glass (AWG) standard, the amount of biofilms formed on HA and PA is obviously reduced. But AA has clearly a much higher amount of adhered *Pseudomonas fluorescens*, indicating no repulsive potential at all.

### 4.6.2 Marine Bacterial Biofilm

The three bacteria, *Vibrio alginolyticus*, *Cobetia marina* and *Marinobacter hydrocarbonoclasticus* are common marine biofilm bacteria. They form an early biofilm as starting point for biofouling in marine environment.

The evaluation results are shown in Figure 4.27. *Cobetia marina* adheres to all three polysaccharide surfaces in a rather similar fashion within the error bars of the measurements and no antifouling effect can be observed compared to AWG. The foul-release performance of the three polysaccharide coatings is much worse than AWG. Biofilm formation for *Vibrio alginolyticus* shows a similar trend and settlement is not inhibited by the coatings. Interestingly HA shows good release performance and 98% of the biofilm is removed after the application of a shear flow by the rotor. Thus HA can be considered as a foul-release surface with respect to Vibrio alginolyticus. Biofilm formation of *Marinobacter hydrocarbonoclastics* on AA and HA surfaces is highly reduced while the biofilm formation on PA is extremly high. None of the polysaccharide coatings show any anti-fouling or foul-release

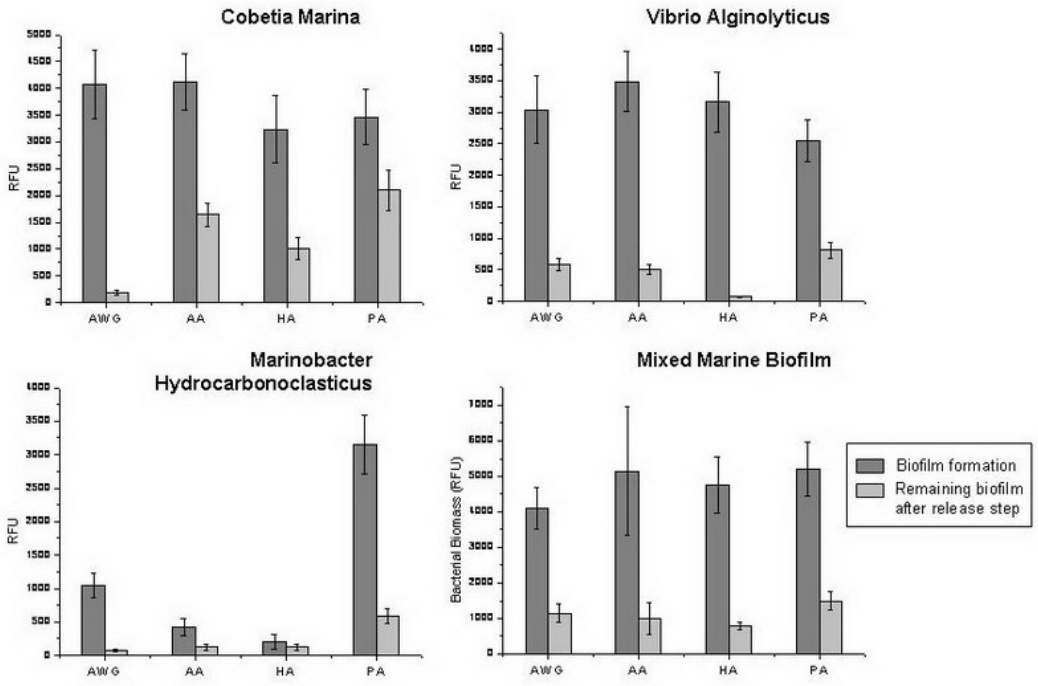


Figure 4.27: Biofilm formation of marine bacteria on polysaccharide surfaces.

performance with respect to the mixed marine biofilm.

### 4.6.3 Algae

**Macroalga: *Ulva linza***

Figure 4.28 shows the settlement result for the zoospores of *Ulva linza*. Both AA and HA significantly reduce settlement of the spores. The HA coating also shows a 64% removal of the attached zoospores after exposure to 53 Pa wall shear stress. Therefore, AA and HA can be considered as anti-fouling coatings for *Ulva* attachment. PA in contrast shows a similar performance as AWG and reveals no noticeable resistance against *Ulva* attachment.

**Diatom: *Navicula perminuta***

Since the cells of the diatom *Navicula perminuta* are not as motile as *Ulva* spores, they reach a surface by falling through the water by gravity. Thus, at the end of the incubation period, the number of cells present on every surface will in principle be nearly the same, as shown in Figure 4.29. Therefore, the aim of the diatom cell attachment assay is rather to test the foul-release property but not the foul-resistant property of the coating. As shown in Figure 4.29, before and after exposure to a shear stress in a flow channel, AA, HA and PA all show very similar performance

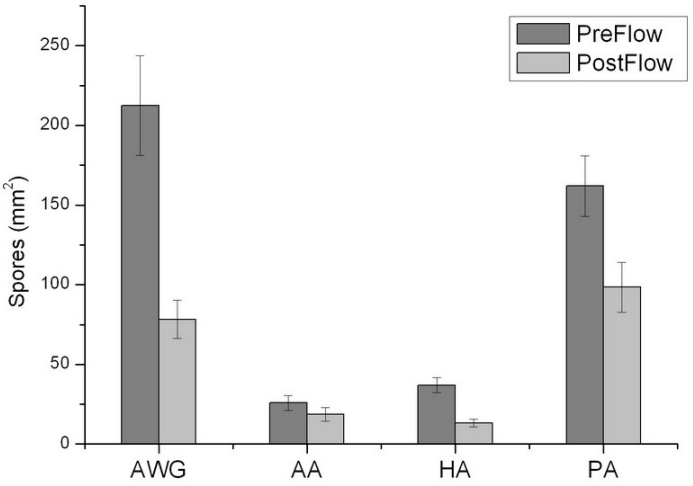


Figure 4.28: Ulva spores adhesion on polysaccharide surfaces.

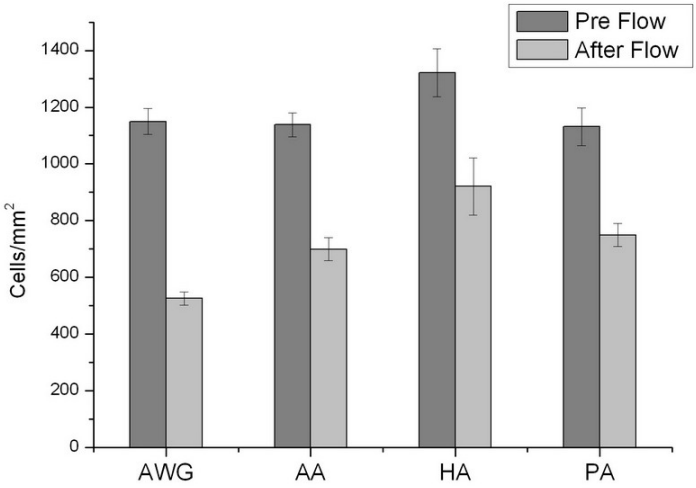


Figure 4.29: Diatom (*Navicula*) adhesion on polysaccharide surfaces.

as AWG. This result indicates that none of the three polysaccharide coatings can inhibit or weaken the attachment of *Navicula*.

### 4.6.4 Invertebrates: Barnacle Cyprids of *Balanus amphitrite*

Figure 4.30 shows the settlement of barnacle cyprids on the three polysaccharide coatings after 24 and 48 hours incubation time. For this marine organism, which is more complex than bacteria and algae, all three polysaccharides inhibit attachment of the barnacle cyprids, especially in the first 24 hours. Compared to AWG, settlement is strongly inhibited by HA. AA and PA perform rather similar and reduce about half the settlement of barnacle cyprids after 48 hours incubation. As described in section 3.7, there were no release experiment in this assay.

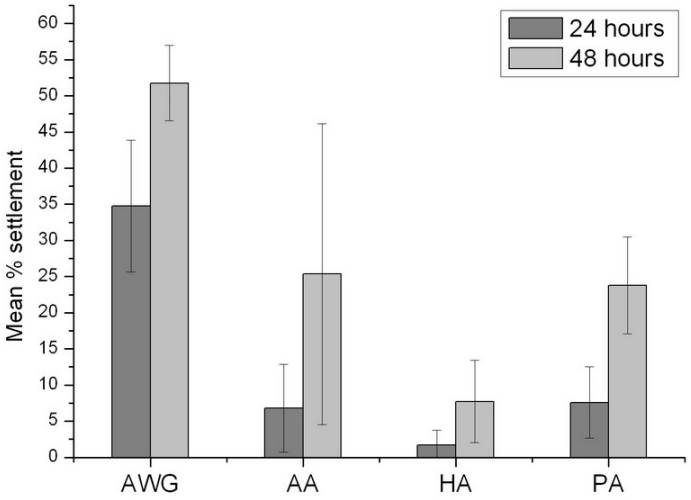


Figure 4.30: Settlement of barnacle cyprids on polysaccharide surfaces after 24 and 48 hours.

## 4.7 Conclusions and Discussions

Concluding, acidic polysaccharides AA, HA and PA were covalently coupled on glass and Si subsrates successfully, protein adsorption test, cell attachment test, and settlement assays with respect to a range of marine organisms were performed on these polysaccharide surfaces.

Protein adsorption tests reveal that these polysaccharide surfaces are resistant to large and positively charged proteins, but not to the small and positively charged proteins (such as lysozyme). The interaction between polysaccharides coatings and proteins are mainly determined by charge and steric effects. Adsorption of calcium on polysaccharide surfaces changes their resistance behavior, which is probably due to the Ca-induced chain-chain interactions between the polysaccharide molecules.

Cell attachment test confirms that the three polysaccharide surfaces are resistant against the adhesion of stem cells KG1a and Jurkat.

All three investigated surfaces seem to be suitable for attachment of most of the used marine species. No polysaccharide is able to completely suppress attachment of biomass and therefore none of the coatings can be considered as promising antifouling coating. This is a surprising finding compared to the fact that they are protein resistant (see section 4.3) and resistant to cell adhesion (see section 4.4). But their different behaviors against the marine organism settlement give a lot of information about the influence of surface properties on biological adhesion.

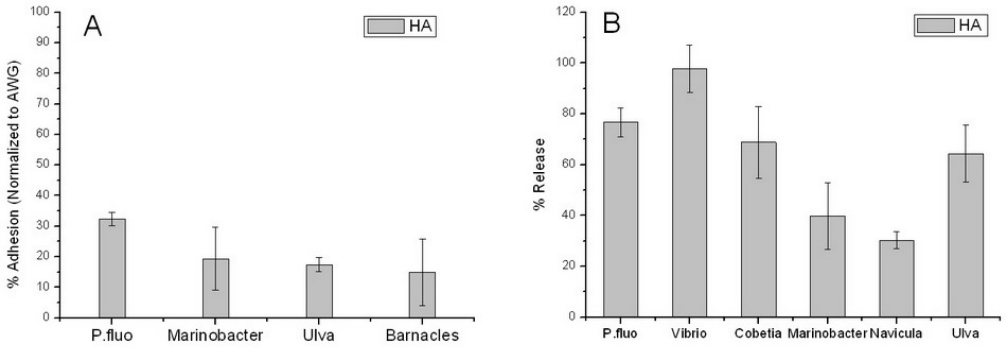


Figure 4.31: Antifouling (A) property of hyaluronic acid (HA) (compared to AWG, settlement on AWG is 100%) and foul-release (B) property of hyaluronic acid (HA).

As shown in Figure 4.31A, HA shows good antifouling performance against settlement of *Pseudomonas fluorescens*, *Marinobacter hydrocarbonoclasticus*, *Ulva* spores and barnacle cyprids compared to AWG (corresponding to 100% settlement). The relatively good performance of HA compared to AA and PA is interesting from a surface science point of view. Compared to AA and PA which both have a contact angle close to 20°, HA is more hydrophilic with a contact angle smaller than 10°. It turns out that inspite of having similar protein resistance properties, settlement of marine organisms is only significantly reduced by the very hydrophilic surface of HA.

Taking a closer look at the release properties as represented in Figure 4.31B it turns out that all investigated species show relatively good release properties on the HA coating. As many bacterial glues consist of exopolysaccharides [88] and polysaccharides also play an important role in the glue system of *Ulva* [12], the question arises why glues which are chemically similar to the coating show a relatively weak adhesion strength. Especially *P.fluorescens* and *Vibrio* show very high percentages of removal, while *Marinobacter* and *Navicula* have only moderate release properties. Seen in the light of the above described protein adsorption data, the size and charge of the secreted macromolecules might be different for the investigated mi-

croorganisms and therefore the glues might have different abilities to penetrate into the topmost network of the polysaccharide coating on the surface.

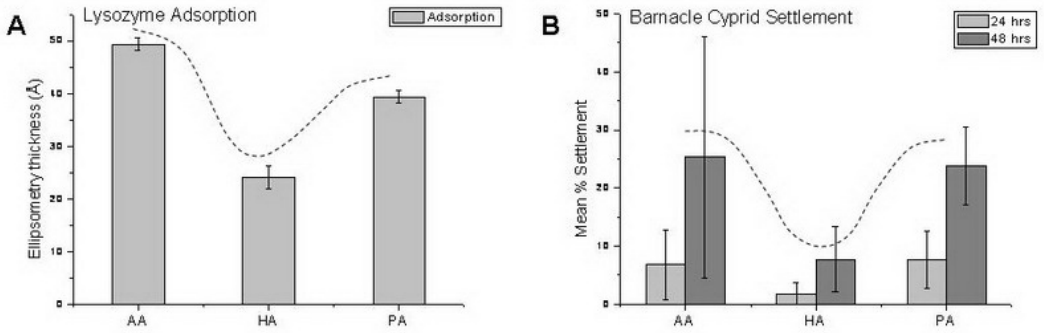


Figure 4.32: The effects of Ca adsorption: lysozyme adsorption (A) and barnacle cyprid settlement (B) on polysaccharide surfaces.

The interactions of polysaccharides with ions, especially $Ca^{2+}$, could also play a role in the adhesion of marine organisms [89]. As shown in the calcium adsorption experiments in section 4.3, a stronger calcium adsorption on AA and PA than on HA has been observed (Figure 4.19). This calcium binding induces remarkable increase of lysozyme adsorption on AA and PA surfaces (Figure 4.32A). According to the literature [90, 91], calcium plays an important role in the settlement of barnacle cyprids. The settlement of barnacle cyprids on the polysaccharide surfaces (Figure 4.32B) shows the very similar trend as the adsorption of lysozyme on the polysaccharide surfaces which have been immersed in ASW for 24 hrs. Based on these results, the relatively better antifouling performance of the HA surface than AA and PA surfaces is probably due to the weaker adsorption of calcium on it. Additionally, the adhesive (or extracellular polymeric substances, EPS) of many marine organisms also contains polysaccharides. Calcium might improve the binding between surface coated polysaccharides and polysaccharides in the adhesives through the electrostatic interactions or through the stereochemically specific chain-chain interactions between the polysaccharide molecules [66, 86]. Therefore, a calcium-inert surface such as HA shows the best antifouling performance among the three polysaccharide coatings.

Besides the hydrophilicity of the HA surface and its weak adsorption of calcium, the mechanical properties must also be considered. Sackmann's study indicates that surface grafted hyaluronic acid exhibits a distinctive swelling behavior which makes the layer very elastic [68]. Large amounts of intra- and intermolecular hydrogen bonds make the HA layer behave like a gel when the surface is immersed in water [65]. These mechanical properties should also contribute to the relatively good antifouling and/or foul-release performances of HA with respect to some marine organisms.

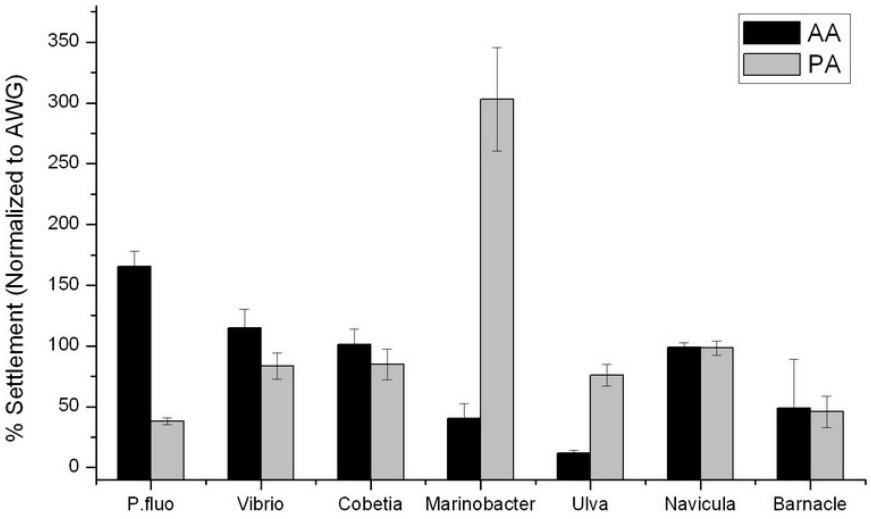


Figure 4.33: Comparison between attachment to alginic acid (AA) and pectic acid (PA) coatings for for *Pseudomonas fluorescens*, *Vibrio alginolyticus*, *Cobetia marina*, *Marinobacter carbonoclasticus*, *Ulva* spores, *Navicula* and barnacle cyprids.

Besides the performance of hyaluronic acid, the comparison between alginic acid and pectic acid is worth to be further discussed. Figure 4.33 gives a direct comparison of settlement of the investigated marine microorganisms on AA and PA. The freshwater bacterium *Pseudomonas fluorescens*, marine bacteria *Vibrio alginolyticus* and *Cobetia marina* show the same trend as they all prefer settlement on alginic acid. *Vibrio* and *Cobetia* show a much smaller variation between the two surfaces than *Pseudomonas fluorescens*. In contrast, *Marinobacter* and *Ulva* show the opposite trend and prefer to settle on pectic acid. *Navicula* and barnacle cyprids in contrast do not distinguish the two surfaces from each other.

Between AA and PA surfaces, huge differences in the settlement of *P.fluorescens*, *Marinobacter* and *Ulva* spores are observed. Since the surface analysis results reveal that the general surface properties of AA and PA such as wettability (see in Table 4.1), thickness (see in Table 4.4) and adsorption of calcium (see in Table 4.9) are highly comparable, the extremely different antifouling behavior of AA and PA should be related to their molecular conformations. As shown in Figure 4.1, in AA and PA molecules, the backbone and the functional groups attached to the cyclic saccharide units are chemically highly similar, the conformational difference is determined by the glycosidic linkage: $1 \rightarrow 4$ di-axial or $1 \rightarrow 4$ di-equatorial [66]. The AA studied in this thesis is composed mainly by di-equatorial $\beta$-$(1 \rightarrow 4)$-linked mannuronic acid (high 'M'), while PA is composed by di-axial $\alpha$-$(1 \rightarrow 4)$-linked galacturonic acid.

Some recent studies by de Kerchove and Elimelech show different changes in mechanical properties of physically adsorbed AA and PA layers due to the interaction

with calcium ions [92]. In the presence of $Ca^{2+}$, the AA layer shows increasing fluidity by swelling and behaves as a gel [93], while the PA layer becomes significantly more rigid. This might be an explanation of the different anti-fouling performance of AA and PA surfaces. Furthermore, the different molecular conformation (such as the linkage between the repeating units) of polysaccharide molecules probably plays an important role in the change of mechanical properties [87, 92].

# Chapter 5

# Polyelectrolyte Multilayers

Polyelectrolyte multilayer films have been widely studied in recent years [94]. These studies concentrated not only on the construction technique and the chemical and physical properties of the multilayer films, but also on their various biological and medical applications.

Polyelectrolyte multilayer deposition is a stepwise repetitive approach [95]. With this approach, multilayer films are assembled layer-by-layer by the repetitive, sequential adsorption of oppositely charged polyelectrolytes from dilute aqueous solutions [96]. Layer-by-layer deposition not only produces uniform, highly interpenetrated ultrathin films [1], but also allows nanoscale control over the thickness and composition of the deposited film. Furthermore, there are many parameters that can alter or control the chemical and physical properties of polyelectrolyte multilayer films, such as the choice of different oppositely charged polyelectrolyte pairs, the pH value and ionic strength of the polyelectrolyte solutions [1]. Polyelectrolyte multilayer films are usually assembled by electrostatic forces or hydrogen-bonding. Therefore, in order to improve their stabilities, the multilayer films can be cross-linked thermally or photochemically [96].

The topography of the multilayer film can be controlled by the pH value of the polyelectrolyte solution [97]. There are many un-reacted functional groups (e.g. carboxyl groups and amino groups) on the surface or within the film. These groups can be used as anchors to covalently bind other chemicals in order to regulate the wettability and chemistry of the surface. Therefore, the effects of both topography and chemistry on anti-fouling and foul-release properties of the polyelectrolyte multilayer films can be studied.

Polyelectrolyte multilayer films are found to be very promising in biological and medical applications. Many research groups studied the interactions between polyelectrolyte multilayer films and proteins and cells, and encouraging results were obtained [1, 96, 98]. Protein-resistant and cell-resistant multilayer films were achieved

by the proper choice of polyelectrolyte pairs and the control of the film properties (e.g. stiffness and roughness).

Various polyelectrolytes can be applied to assemble multilayer films. In this work, positively charged polyethylenimine (PEI, MW: 25000) and negatively charged poly(acrylic acid) (PAA, MW: 100000) were used to construct the multilayers. The concentration of their aqueous solutions is 1 mg/mL for PEI and 3 mg/mL for PAA. Their molecular structures are shown in Figure 5.1.

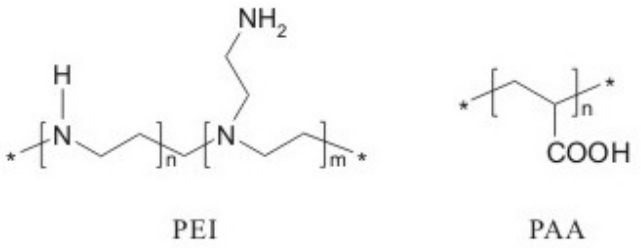


Figure 5.1: Molecular structures of PEI and PAA.

In this chapter, the construction of the polyelectrolyte multilayers and the surface analysis of these thin films are discussed in detail. Their ability to inhibit the settlement of Ulva spores and Barnacle cyprids was evaluated. Results are shown in this chapter and discussed with respect to the effects of surface morphology and chemistry.

## 5.1 Preparation of PAA and PEI Monolayers

In order to determine if the chemistry of the selected polyelectrolytes has any anti-fouling properties, PAA and PEI monolayers were prepared to test their resistance against protein adsorption and marine organism adhesion. PAA and PEI were covalently coupled to the glass slide surface through a similar reaction as described in the polysaccharide coupling in chapter 4.

### 5.1.1 Preparation of PAA Monolayers

The coupling of PAA onto glass or silicon surfaces is the same as the coating of polysaccharides. Glass slides are first functionalized by aminosilane (APTES). Then the surface amino groups are covalently linked with the carboxyl groups in the PAA molecules through the formation of amide bonds (as shown in Figure 4.3 on page 38).

1 mg/mL PAA, 0.1 M EDC and 0.05 M NHS were dissolved in 10 mM HEPES buffer (pH 6-7) and stirred for 20 minutes. Then the APTES coated glass slides were immersed into the solution and placed on a vibrational table. After 16 hours,

the slides were removed from the solution and washed with millipore water. Since the polyelectrolyte PAA is much easier to dissolve in water than polysaccharides, the 5-days washing step in the polysaccharide preparation is not necessary for the PAA monolayer coupling. Slides were soaked in millipore water and shaken for 24 hours to remove the physically absorbed molecules. Finally, they were dried with $N_2$ gas.

### 5.1.2 Preparation of PEI Monolayer

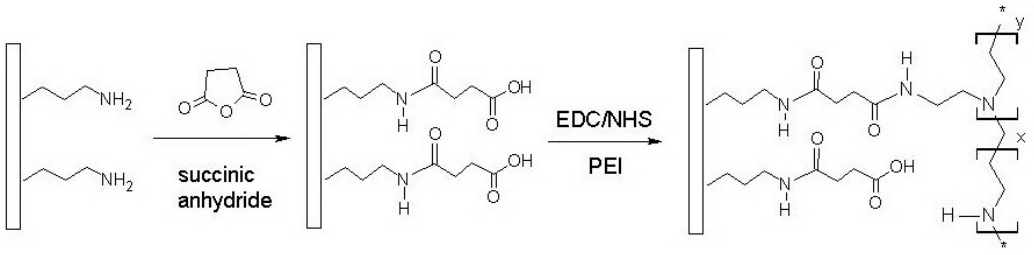


Figure 5.2: Preparation of covalently coupled PEI monolayer.

The process for the covalent coupling of the PEI monolayer on glass or Si substrates is shown in Figure 5.2. 0.1 M succinic anhydride was dissolved in Dimethylformamide (DMF, p.A.). APTES coated glass slides were soaked in the succinic anhydride/DMF solution for 24 hours while shaking [99]. The ring of the succinic anhydride opens and the surfaces are functionalized by carboxyl groups. Then the slides were washed with DMF and dried with $N_2$ gas. The next step is the coupling between the carboxyl groups on the glass surface and the amino groups in the PEI molecules (as shown in Figure 4.3). 0.1 M EDC, 0.05 M NHS and 1 mg/mL PEI were dissolved in HEPES buffer. Glass slides were immersed in the reaction solution and shaken for 16 hours. Finally, the slides were washed with millipore water, shaken in a millipore water bath for 24 hours and dried with $N_2$ gas.

## 5.2 Preparation of Polyelectrolyte Multilayers

The classical way to prepare polyelectrolyte multilayers is dip coating as described in the literature [94]. Due to the large amount of samples (for each type of surface, 6 slides for biological evaluation of each fouling organism and 1-2 slides for surface analysis) required in the AMBIO project, it takes very long time to prepare these samples with the conventional dip coating method. To speed up the sample preparation and to approach technical application, one goal of this thesis was to develop a spray coating method for the preparation of polyelectrolyte multilayers. Both dip coating and spray coating methods are briefly introduced in this section.

Objective glass slides were used as substrates. Before the construction of the polyelectrolyte multilayers, glass slides were cleaned and activated by piranha solution, and functionalized by APTES as described in chapter 4. The covalently bonded APTES layer enhances the stability of the bonding between the surface and the multilayer film.

### 5.2.1 Dip Coating Method

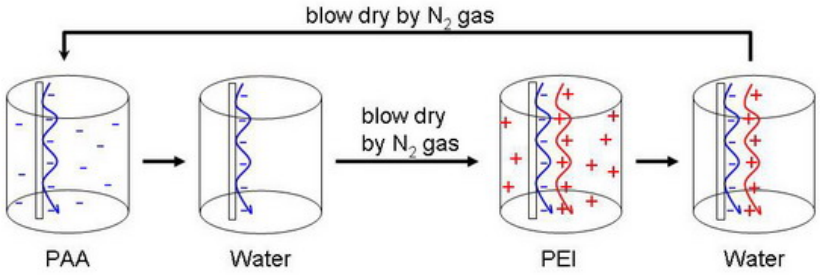


Figure 5.3: Construction of polyelectrolyte multilayers by the dip coating method.

The dip coating method is a simple and widely used technique to construct polyelectrolyte multilayer films. The process is shown in Figure 5.3. Substrates are first immersed into PAA solution for a certain time. Then they are taken out of the solution, washed in a millipore water bath to remove loosely attached molecules and dried by $N_2$ gas. Thereafter, they are immersed into PEI solution for a certain deposition time to assemble the second layer. The substrates are washed with millipore water and dried by $N_2$ gas again. The deposition and washing steps are repeated until the desired amount of layers is obtained.

### 5.2.2 Spray Coating Method

Using the spray coating method to construct polyelectrolyte multilayers is a relatively new technique. Compared to the dip coating method, spray coating is more suitable for large surfaces and is much easier to automatize. These advantages make spray coating a promising technique for mass production. Therefore, the spray coating method was applied to prepared the large amount of samples for the AMBIO project.

The procedure for spray coating is shown in Figure 5.4. It is in principle quite similar to the dip coating method. The substrate is vertically fixed on a holder. PAA solution is first sprayed onto the substrate surface. After a certain deposition time, the surface is rinsed with millipore water and dried by $N_2$ gas. Then, PEI solution is sprayed onto the surface to assemble the second layer. PAA and PEI are deposited onto the surface sequentially to form the multilayer film.

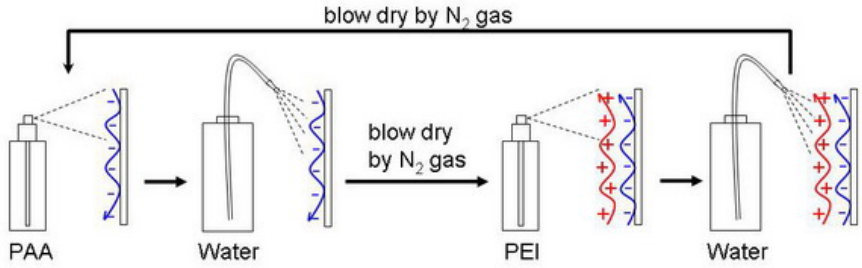


Figure 5.4: Construction of polyelectrolyte multilayers by the spray coating method.

A self-designed holder was made to hold 8 glass slides at the same time. This holder greatly increased the preparation efficiency. Glass spray bottles which can generate fine spray and consume only a small amount of solution were purchased from NeoLab, Germany. The spraying angle is 35°. By each press of the spray head, 0.05 mL solution is sprayed out. The experimental setup is shown in Figure 5.5.


Figure 5.5: Experimental setup for spray coating of polyelectrolyte multilayers: glass slides holder and spray bottles.

The formation and properties of PAA/PEI polyelectrolyte multilayer films are controlled by many parameters, such as the deposition time for each layer, the amount of layers, or the pH value of the solution. These will be discussed in details in section 5.3.

### 5.2.3 Thermal Crosslinking

Polyelectrolyte multilayers are only assembled by weak electrostatic forces or hydrogen bonds. Therefore, crosslinking the layers to generate covalent bonds in the network is a very important step to get a stable multilayer film. Heat treatment

in vacuum is the most popular way to crosslink the layers and remove the water molecules trapped in the multilayer network.

A Heraeus VT6025 vacuum oven (purchased from Carl Roth, Germany) was used for the thermo-vacuum crosslinking. The polyelectrolyte multilayers were crosslinked at 160 °C for 6 hours with $4 \times 10^{-2}$ mbar vacuum. Since there is no air in the vacuum oven, glass slides coated with polyelectrolyte multilayers were placed flat on the heating plate for optimal heat conductivity.

In-situ AFM measurements have been applied to test the stability of thermally crosslinked polyelectrolyte multilayers. Figure 5.6 shows that the morphology of a crosslinked multilayer film is almost unchanged after one day and even 7 days immersion in seawater.

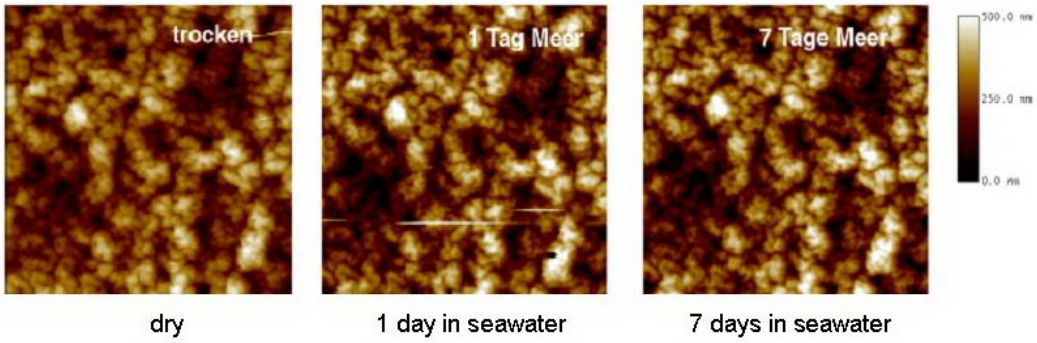


Figure 5.6: Stability test of crosslinked polyelectrolyte multilayers by immersion in seawater, imaged by in-situ AFM.

## 5.3 Layer-by-Layer Spray Coating of Polyelectrolyte Multilayers

The properties of the polyelectrolyte multilayer films, such as homogeneity, morphology and thickness have been studied with respect to the deposition time of each layer, the amount of layers and the pH value of the polyelectrolyte solutions.

### 5.3.1 Deposition Time

The deposition time is the time interval between the deposition of two adjacent, oppositely-charged polyelectrolyte layers. To study the effect of deposition time on the properties of the multilayer films, samples with two different deposition times (3 mins and 1 min) were prepared. In this experiment, 3 mg/mL PAA solution (pH=2.89) and 1 mg/mL PEI solution (pH=9) were used for the deposition of multilayer films with 15 layers. Since the substrates are held vertically, when the solution is sprayed onto the surface, the excess solution drifts to the bottom by

gravity and leaves only a thin liquid film on the surface. Due to evaporation, the surface dries within about one minute. Therefore, to keep the surface always wet during the deposition period, polyelectrolyte solution has to be re-applied onto the surface every minute. For the sample with 3 minutes deposition time of each layer, polyelectrolyte solution was re-applied twice, once per minute. To make sure that the same amount of solution was used in the preparation of each sample, for the sample with one minute deposition time, the solution was also re-applied twice, once per 20 seconds.

The topography and thickness of the polyelectrolyte multilayer films were investigated by SEM. Though the two samples have different deposition times (3 mins and 1 min), they have quite similar surface morphology and film thickness as shown in Figure 5.7.

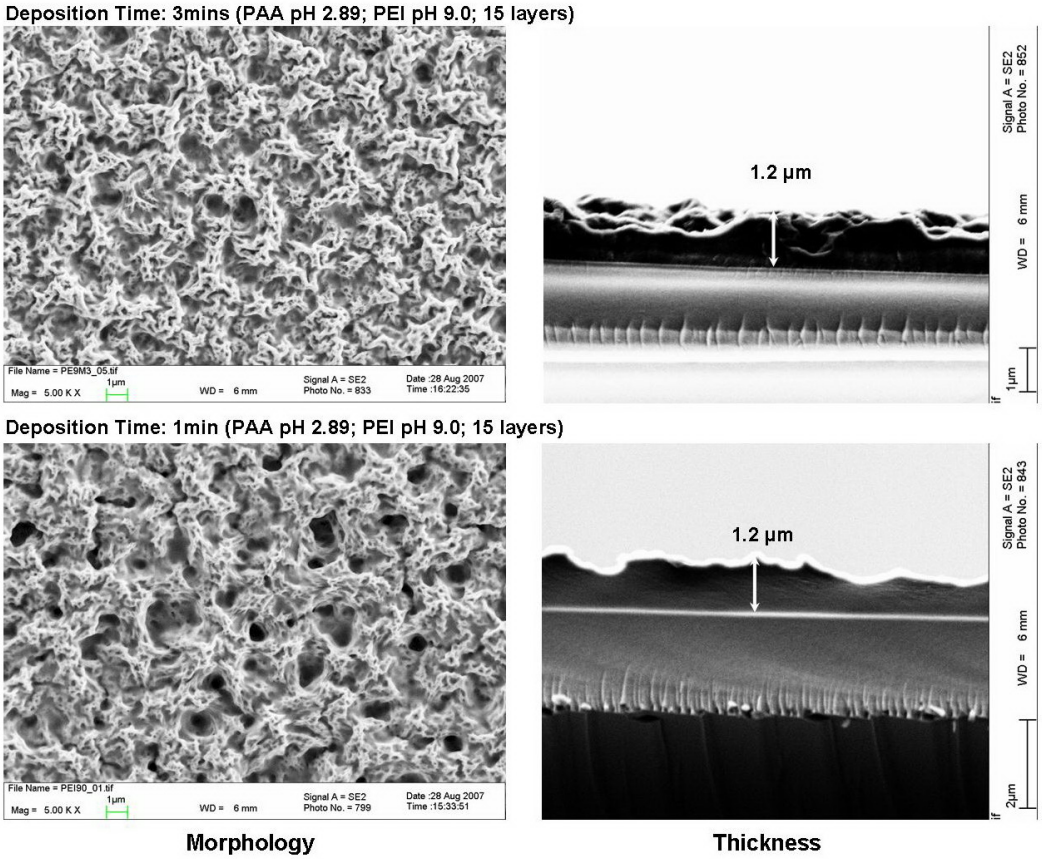


Figure 5.7: Effect of deposition time on the morphology and thickness of polyelectrolyte multilayer films.

Since a deposition time longer than one minute would not greatly change the properties of the multilayer films, in the following experiments, the multilayer films were all prepared with one minute deposition time for each layer.

### 5.3.2 The Top Layer and Number of Layers

The top layer (or the terminal layer) and the number of layers have a strong influence on the topography of the multilayer film and the film thickness. As reported in earlier studies on the multilayer systems, the film thickness grows exponentially with increasing number of deposited layers [97].

Polyelectrolyte multilayer films with a different number of layers were prepared to study the effect of the top layer and number of layers on the surface morphology and film thickness. The polyelectrolyte solutions were 3 mg/mL PAA (pH=2.89) and 1 mg/mL PEI (pH=9). The deposition time of each layer was one minute. During the layer-by-layer deposition, the changes of the multilayer surface can easily be observed. When PAA was the top layer, the film was opaque, which indicates a rougher surface. When PEI was the top layer, the film was transparent, which indicates a smoother surface. This instantaneous transition happens after the deposition of each layer. As an example, the topographical changes from 13th layer to 15th layer are demonstrated by SEM images in Figure 5.8.

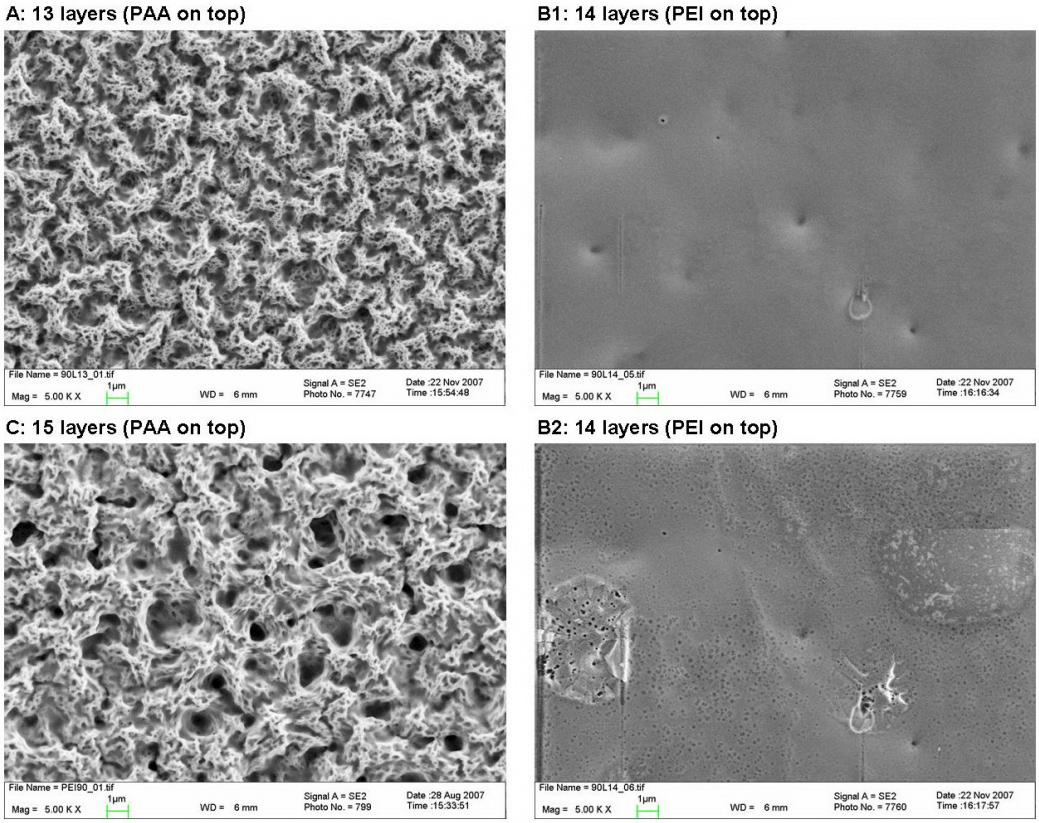


Figure 5.8: The topography differences of polyelectrolyte multilayer films with different top layer: **A**) 13 layers (PAA on top); **B1** and **B2**) 14 layers (PEI on top); and **C**) 15 layers (PAA on top).

After 13 layers were deposited, the film surface was rough with micro-sized structures (Figure 5.8A). When the 14th layer, the PEI layer, was deposited, the topog-

raphy completely changed and the surface became smooth and flat (Figure 5.8B1). After the deposition of the 15th layer (PAA layer), the surface became rough again and micro topography reappeared (Figure 5.8C). The smooth-effect induced by the deposition of PEI can be explained by the diffusion of smaller polycations into the film [100, 101].

Another interesting observation is the stability of the multilayer film. The multilayer films shown in Figure 5.8 are all thermally crosslinked. When PAA is the topmost layer (Figure 5.8A and C), the multilayer films are very stable under the illumination of the electron beam during the SEM imaging. No obvious destruction of the film has been observed in the SEM images. But the surface with PEI as the topmost layer is fragile. Figure 5.8B1 shows a very smooth surface. After only about one minute scanning by the electron beam at the same spot, destruction of the PEI layer is clearly observed in Figure 5.8B2.

As demonstrated in Figure 5.8, only when PAA is the topmost layer the multilayer films have nano-micrometer sized structures on the surface. Therefore, only multilayer films with PAA as top-layer (odd number of layers) were chosen to study the influence of the number of layers on surface morphology. Multilayer films with 7 layers, 11 layers, 15 layers and 25 layers were prepared. The surface topography and film thickness of these multilayer samples are shown in Figure 5.9.

With an increasing number of layers, the topography and thickness of the film are dramatically changed. When there are only 7 layers deposited on the surface, the randomly arranged structure is about 1/10 $\mu$m (or 100 nm) in size and the film thickness is so thin that it is difficult to be determined by SEM. After deposition of 11 layers, the structure size increases to about 1 $\mu$m and the film thickness increases to around 600 nm. After 15 layers, the structure increases to about 2 $\mu$m and many 1-2 $\mu$m sized holes appear on the surface. The thickness increases to more than 1 $\mu$m. When 25 layers are deposited, the morphology does not change significantly but the thickness continuously increases to nearly 2 $\mu$m.

From the cross-section of the multilayer films (Figure 5.9, right column) we can find that the films are not distinguished by layers, although they are prepared by layer-by-layer deposition. The growth mechanism of multilayer films is based on the diffusion of polycations [100, 101]. When PEI is deposited on the film, excessive polycations diffuse into the film. After PAA is deposited, the free polycations diffuse out of the film and form a complex with the polyanions [97]. This coalescence process forms a highly intermixed film.

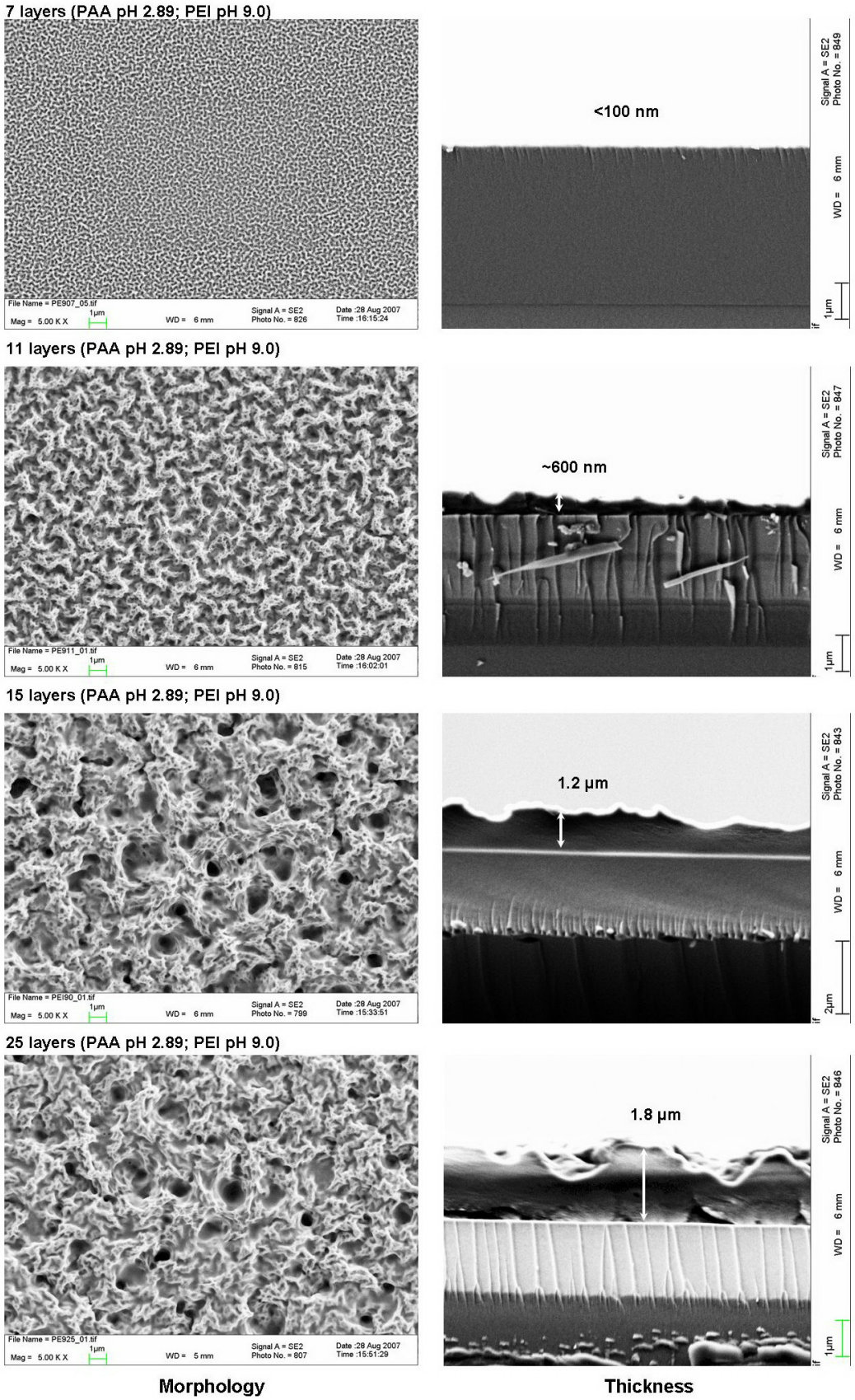


Figure 5.9: The morphology and thickness of polyelectrolyte multilayer films with different number of layers.

### 5.3.3 pH Value of the Polyelectrolyte Solution

As has been reported in many papers [1, 96, 97], when using the layer-by-layer dip coating method to construct polyelectrolyte multilayers, the pH value of the polyelectrolyte aqueous solution has a very strong effect on the stiffness, roughness and topography of the multilayer films. In the spray coating method, the pH effect should also be a sensitive trigger to finely control the structure of the multilayer films.

Polyelectrolyte solutions with different pH values were used to prepare the multilayer films. The pH of the polyelectrolyte solutions was measured by a pH meter pH 540 GLP with the pH electrode SenTix 61 (products from WTW, Wissenschaftlich-Technische Werkstaetten GmbH, Germany). Acetic acid was used to adjust the pH. To obtain different morphologies, the pH of the PAA solution was always kept as 2.89 and the PEI solution was adjusted to 4 different pH values (5.0, 6.5, 7.5, and 9.0) to study the pH effect on the formation of polyelectrolyte multilayers. All the multilayer films have 15 layers and one minute deposition time for each layer.

An ionization equilibrium always exists in the electrolyte solution. When the pH of the solution is changed, the equilibrium is also changed. In the case of the PEI aqueous solution, the ionization equilibrium forms as:

$$R{-}\mathrm{NH_2} + \mathrm{H_2O} \rightleftharpoons R{-}\mathrm{NH_3^+} + \mathrm{OH^-} \tag{5.1}$$

The equilibrium constant $K$ is defined as:

$$K = \frac{\left[R{-}\mathrm{NH_3^+}\right]\left[\mathrm{OH^-}\right]}{\left[R{-}\mathrm{NH_2}\right]} \tag{5.2}$$

Equation 5.2 can be changed to the following form:

$$\frac{\left[R{-}\mathrm{NH_3^+}\right]}{\left[R{-}\mathrm{NH_2}\right]} = \frac{K}{\left[\mathrm{OH^-}\right]} \tag{5.3}$$

When the pH of the solution decreases, the concentration of $\mathrm{OH^-}$ anions decreases and the ratio $[R{-}\mathrm{NH_3^+}]/[R{-}\mathrm{NH_2}]$ increases, which means that more amino groups are ionized and the PEI molecules are stronger charged. Therefore, the binding between PAA and PEI molecules is strong when the pH of PEI solution is low, which should result in a thin and smooth film. On the other hand, when the pH of the PEI solution is high, the charge attraction between PAA and PEI is weak, long chain polyelectrolyte molecules have more flexibility and are loosely packed. In this case, a rough and thick film is expected. The analysis about pH induced ionization is confirmed by the research from Choi and Rubner [102].

SEM was used to investigate the topography and film thickness (Figure 5.10).

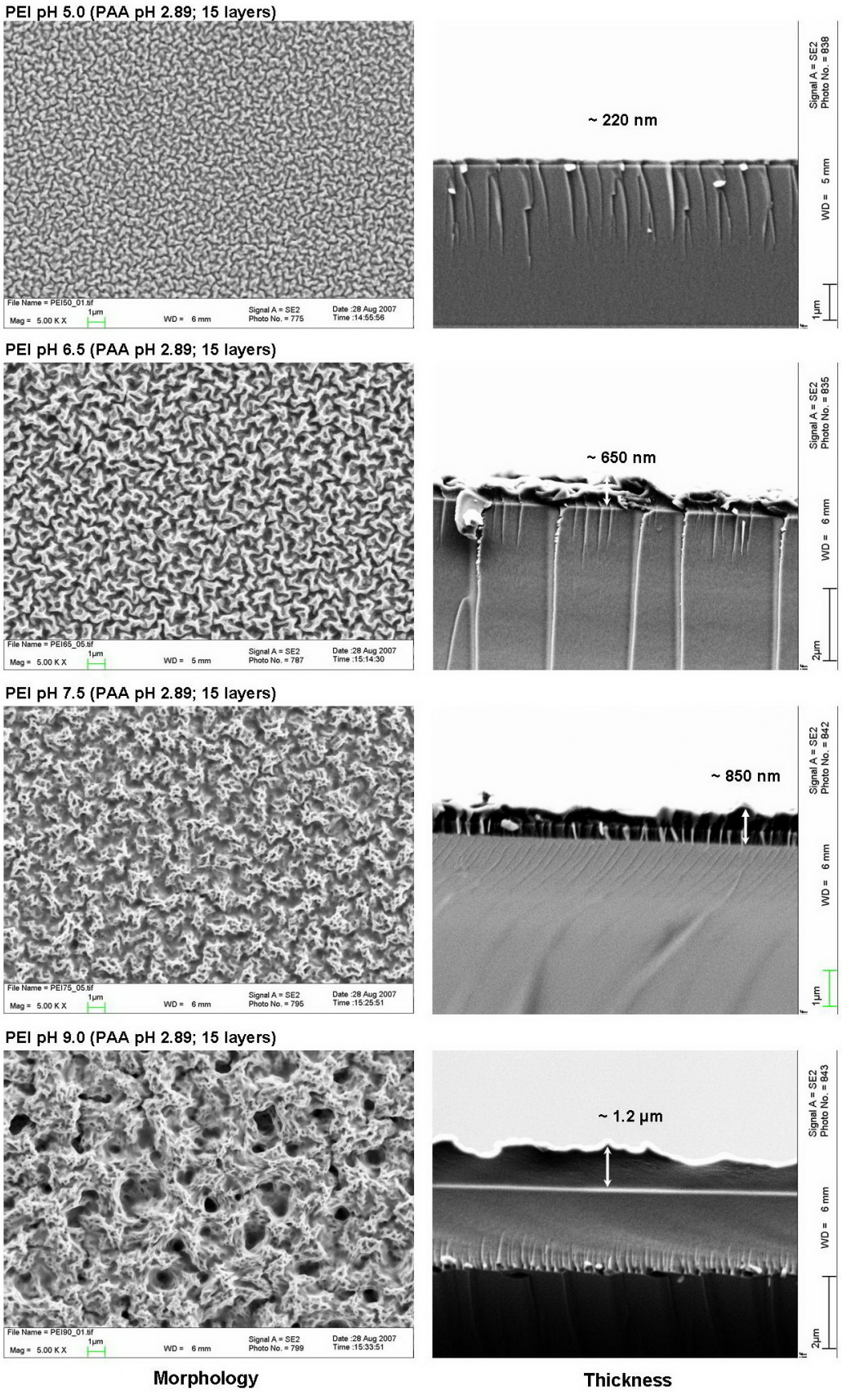


Figure 5.10: Effect of pH on the morphology and thickness of polyelectrolyte multilayer films.

| Multilayers (15 layers) | Thickness (nm) |
|---|---|
| PAA 3 mg/mL, pH 2.89; PEI 1 mg/mL, pH 5.0 | 220 |
| PAA 3 mg/mL, pH 2.89; PEI 1 mg/mL, pH 6.5 | 645 |
| PAA 3 mg/mL, pH 2.89; PEI 1 mg/mL, pH 7.5 | 854 |
| PAA 3 mg/mL, pH 2.89; PEI 1 mg/mL, pH 9.0 | 1196 |

Table 5.1: Thickness of polyelectrolyte multilayers, measured by SEM.

Randomly self-arranged, homogeneous structures can be found on the polyelectrolyte multilayer surfaces. The size of the structure increases from several hundred nanometers to several micrometers with increasing pH value of the PEI solution. Additionally, the pH value also influences the thickness of the films. The trends of changes in morphology and film thickness are perfectly in agreement with the former discussion.

This set of polyelectrolyte multilayer films was chosen to study the topographical effects on marine biofouling. The surfaces of these multilayer films were also modified by fluorinated silane and poly(ethylene glycol) to vary the surface wettability and chemistry to study their influences on marine biological adhesion. Surface modification methods are described in section 5.5. Detailed surface characterizations of these multilayers and modified multilayers are given in section 5.7.

## 5.4 Simultaneous Spray Coating of Polyelectrolyte Multilayers

Besides the layer-by-layer technique, a simultaneous spray method has also been tested to construct polyelectrolyte multilayers. In this method, negatively charged PAA solution (3 mg/mL, pH 2.89) and positively charged PEI solution (1 mg/mL, pH 9.0) were simultaneously sprayed on the substrate to form a layer. Then, the substrate was rinsed with millipore water and dried with $N_2$ gas before the second layer was applied. In contrast to the layer-by-layer technique, when the two counter ions were sprayed simultaneously, precipitates formed immediately on the substrate. The deposition time of each layer and the number of layers were considered to alter the homogeneity, morphology and thickness of the films. Three different samples were prepared. The first sample has 7 layers and one minute deposition time of each layer (Figure 5.11 top). The second sample also has 7 layers but the surface was rinsed immediately after the simultaneous spray was applied (Figure 5.11 middle). The third sample was prepared in the same way as the second sample and the number of layers was increased to 15 (Figure 5.11 bottom). SEM was used to investigate the homogeneity, morphology and thickness of these simultaneously sprayed multilayers.

As shown in the SEM images (Figure 5.11), surfaces of simultaneously coated

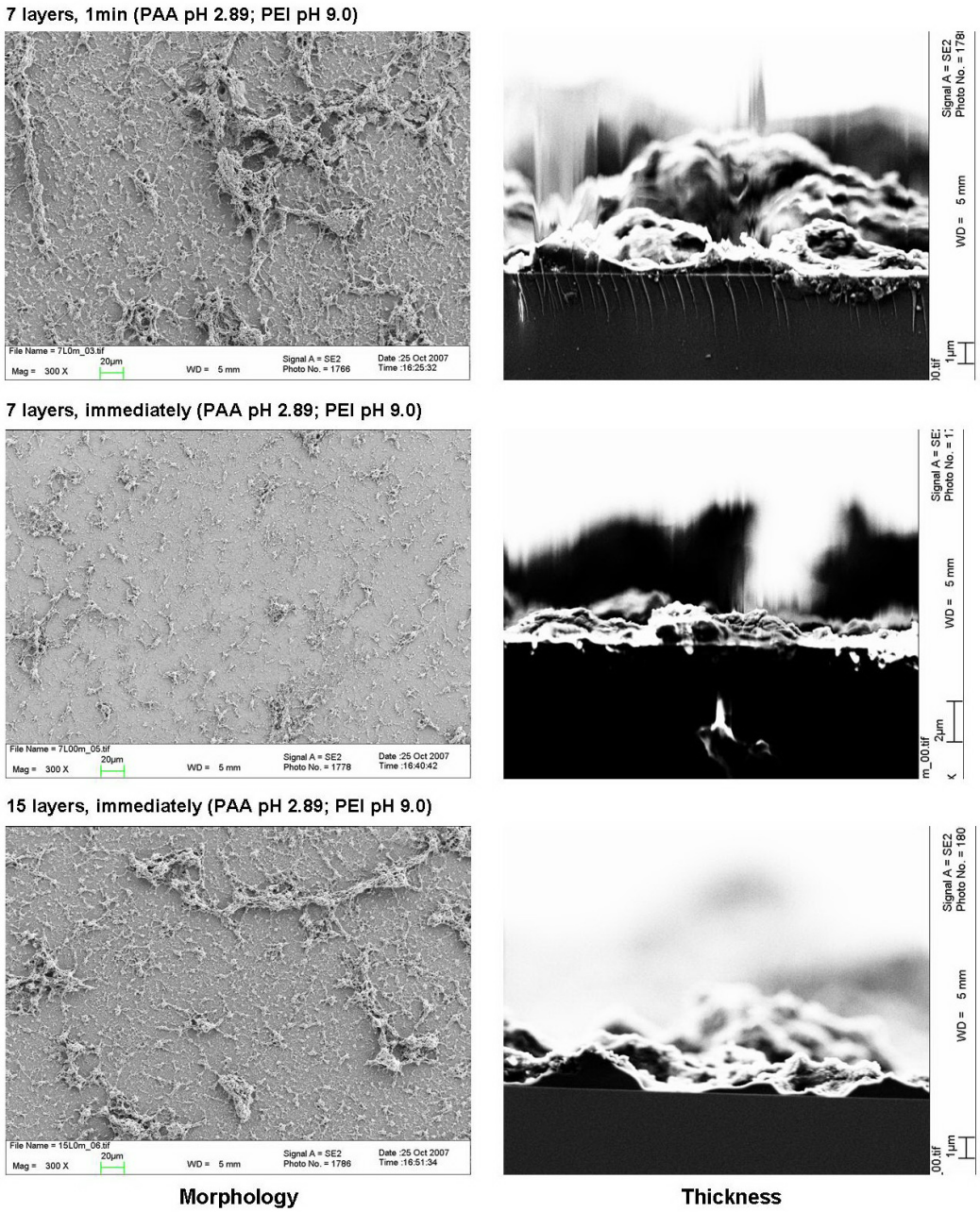


Figure 5.11: The morphology and thickness of polyelectrolyte multilayer films prepared by simultaneous spray coating.

polyelectrolyte multilayers are very irregular. Precipitates with different sizes are observed all over the surface and there are no regular structures. Longer deposition time and more layers result in bigger precipitates. Considering the magnification of the images and the scale bar, most precipitates are much bigger than the structures on the polyelectrolyte multilayers constructed by layer-by-layer technique (Figure 5.10). The surface is so irregular that it is impossible to determine the thickness of the films.

Although such a co-deposition would be practically favorable, the relationships between surface morphology and biofouling are difficult to be studied by these highly irregular structures. Therefore, polyelectrolyte multilayers constructed by simultaneous spray coating were not used for biological evaluations.

## 5.5 Surface Modification

Besides the influences of surface morphology on biofouling [10, 11, 103], surface chemistry also has strong effects on the adhesion of marine organisms. To study the effects of both surface morphology and surface chemistry on biofouling, polyelectrolyte multilayers with different morphologies were also chemically modified. In this way, surface morphology and surface chemistry are combined together (as shown in Figure 5.12). In this thesis, fluorinated silane (F-silane) and PEG were used to modify the polyelectrolyte multilayer surfaces.

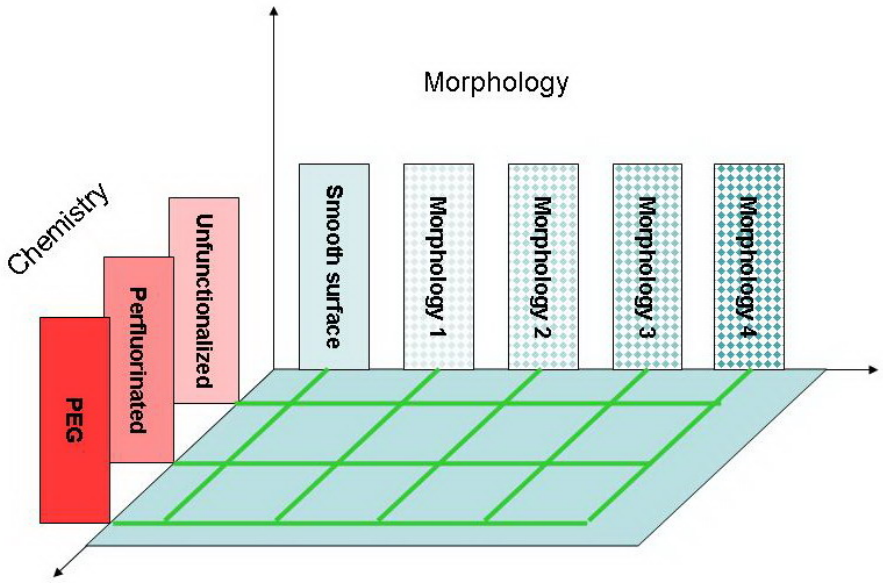


Figure 5.12: Chemical modification on structured polyelectrolyte multilayers: the combination of morphology and chemistry.

### 5.5.1 Fluorinated Silane Coating

Fluorinated silane was coated on Si-wafers, glass slides and polyelectrolyte multilayers through chemical vapor deposition (CVD) to increase the hydrophobicity of the surfaces. Firstly, Si-wafers and glass slides were cleaned and activated by piranha solution and dried in an oven for 30 mins at 105 °C. 0.5 mL fluorinated silane (tridecafluoroctyl-triethoxysilane, purchased from Degussa, Germany) was added into a small glass petri dish at the bottom of a dried exsiccator. Then, Si-wafers, glass slides and polyelectrolyte multilayers were placed in the exsiccator and 0.1 mbar vacuum was applied. The exsiccator was placed in the oven for 2 hours at 80 °C. After the deposition, the samples were rinsed with ethanol (p.A.) and dried with $N_2$ gas.

### 5.5.2 PEG Silane Coating

#### Synthesis of PEG Silane

The synthesis of PEG silane was performed according to Bluemmel's work [49]. 1 g $\omega$-amino-poly(ethylene glycol)monomethylether (MW: 2000 g/mol, with 43 ethylene glycol units) was dissolved in 10 mL dried DMF (p.A.) and 0.05 mmol 3-isocyanatopropyl-triethoxysilane was added in the solution. The mixture was stirred at room temperature for 72 hours with protection of $N_2$ gas (as shown in Figure 5.13).

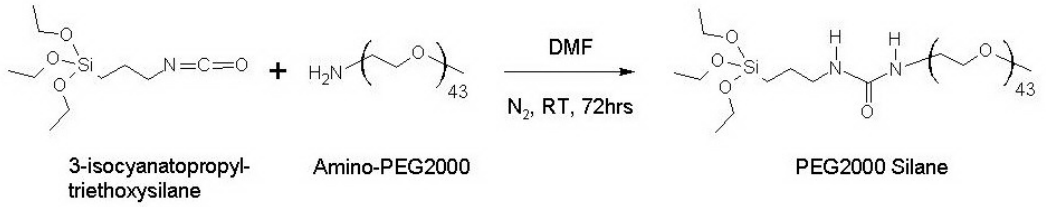


Figure 5.13: Synthesis of PEG2000 Silane.

The raw product precipitated at −20 °C and the solvent was removed by fine vacuum. Then, the raw product had to be purified by recrystallization in nitrogen atmosphere. 2 mL dried toluene (p.A.) was first added to dissolve the raw product, then 8 mL dried cyclohexane (p.A.) was very slowly added on top of the toluene solution. The recrystallization appeared slowly at the interface between toluene and cyclohexane. After 24 hours of recrystallization, the product was washed with dried and cold cyclohexane and finally dried in fine vacuum [49].

#### Coupling of PEG Silane to Substrates

PEG2000 silane was coated on Si-wafers, glass slides and polyelectrolyte multilayers. Before the silane coating, Si-wafers and glass slides were activated by piranha solution. The substrates were placed in a teflon box and dried in the vacuum oven at 80 °C and $10^{-2}$ mbar for 3 hours. 0.25 mM PEG2000 silane and 2.5 $\mu$M triethylamine were dissolved in dried toluene (p.A.). Then the solution was added into the teflon box to immerse the substrates. The teflon box was tightly closed and filled with $N_2$ gas. After 48 hours immersion at 55 °C, the samples were rinsed with ethylacetat (p.A.) and sonicated in ethylacetat for 2 mins and then rinsed again with ethylacetat and methanol (p.A.). Finally the samples were dried with $N_2$ gas.

## 5.6 PAA, PEI, F-silane and PEG Monolayers

### 5.6.1 Surface Characterization

PAA and PEI were covalently coupled to the glass substrate as described in section 5.1. Glass slides coated with F-silane and PEG were also prepared as described in section 5.5. XPS was used to investigate the coatings and calculate the thickness. The contact angle on the coatings was also measured.

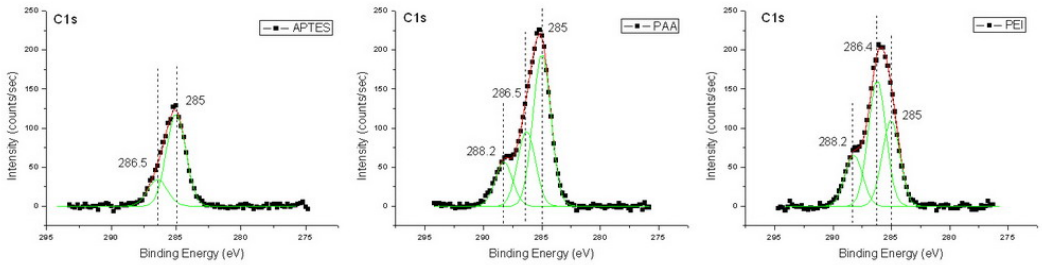


Figure 5.14: C1s XPS spectra of PAA and PEI monolayers on glass.

The stepwise covalent coupling of PAA and PEI onto the glass surface is clearly confirmed by the intensity increase and the broadening of the C1s peak in Figure 5.14. The assignment of each sub-peak can be found in Table 4.5 on page 45. By considering the increased intensity of the C1s peak, the film thickness can be calculated by the method which has been introduced in chapter 4. The results are shown in Table 5.2.

| **Surfaces** | **Thickness** (Å) | **Contact Angle** (°) |
|---|---|---|
| **PAA** | 32.5 | 19.2±2.1 |
| **PEI** | 30.3 | 40.5±0.8 |

Table 5.2: PAA and PEI film thickness calculated by the increase of C1s peaks.

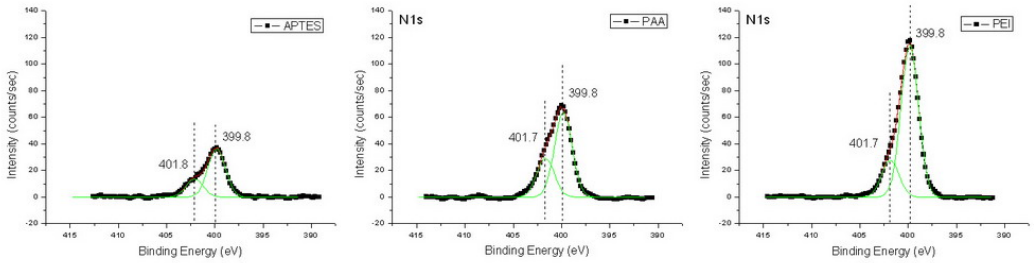


Figure 5.15: N1s XPS spectra of PAA and PEI monolayers on glass.

The N1s peak increases after the coupling of PEI as expected (Figure 5.15), because there are numerous nitrogen atoms in PEI molecules. But, the N1s peak also increases after the PAA coupling. As discussed in chapter 4, this increase of N1s peak is due to the EDC and NHS residues in the film. Since EDC and NHS in the film also contribute to the C1s signal and influence the intensity and distribution of the sub-peaks (Figure 5.14), the detailed stoichiometry analysis based on peak ratios cannot be performed.

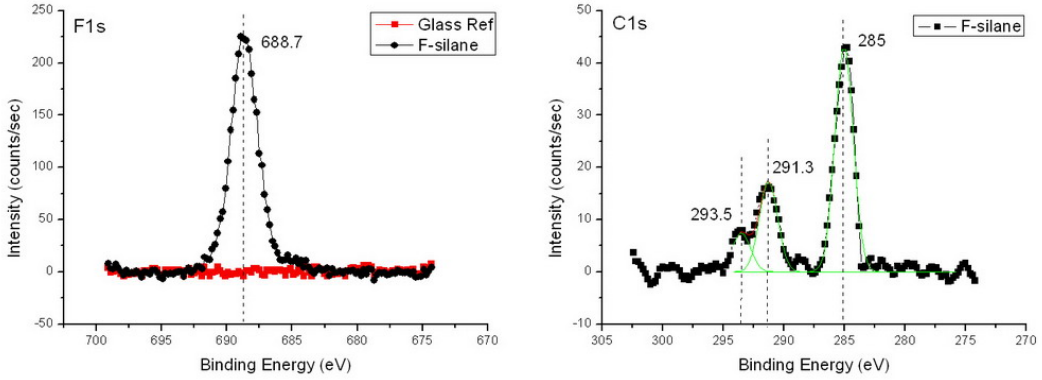


Figure 5.16: F1s and C1s XPS spectra of the F-silane monolayer on glass.

F-silane was coated on the glass surface through CVD. As shown in Figure 5.16, compared to the glass reference sample, a sharp F1s peak is observed on the F-silane coating. The carbon atoms in $-CF_3$ and $-CF_2-$ groups give a C1s peak at 293.5 eV and 291.3 eV, respectively. The C1s peak at 285 eV comes from the alkyl carbon in the silane molecules and also from the hydrocarbon contaminants adsorbed from the atmosphere, therefore its intensity is much stronger than expected.

As shown in Figure 5.17, the PEG2000 silane coating causes a sharp and strong C1s peak. The dominating C1s peak at 286.8 eV is the typical signal of the carbon in the $-(CH_2CH_2O)-$ groups, the weak peak at about 285 eV is due to the alkyl carbon and the hydrocarbon contamination. The molecular weight of this PEG silane is about 2000 Da and there is only one silicon atoms is the molecule, therefore, the deposition of PEG2000 causes a strong attenuation of the Si2p peak. If we assume

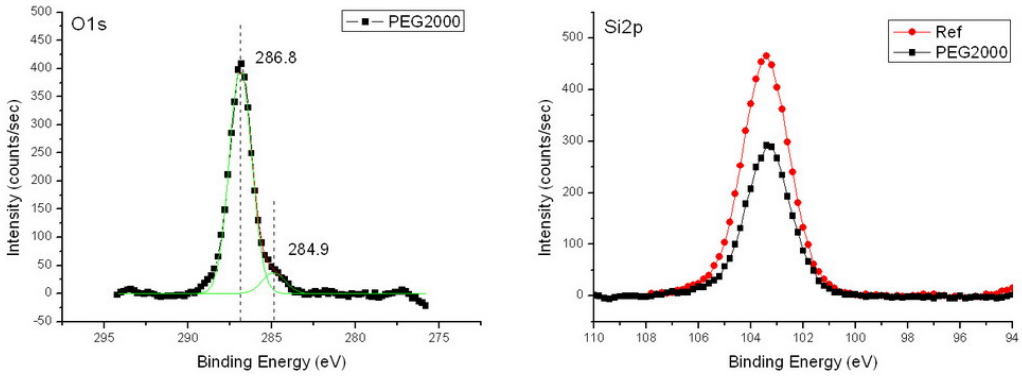


Figure 5.17: C1s and Si2p XPS spectra of the PEG2000 monolayer on glass.

that the contribution of the Si in PEG molecules to the observed Si2p signal is very week, Lambert-Beer's law (Equation 3.7) can be applied to calculate the film thickness by considering the attenuation of the Si2p peak. The calculated thickness is 21.7 Å, which is very similar to the thickness obtained from the ellipsometry measurement on a PEG2000 coated Si-wafer (in Table 5.3). Though PEG2000 molecules are long chain molecules with 43 $-(CH_2CH_2O)-$ units, they are present on the surface in a coiled state, therefore, the film thickness is much smaller than the chain length.

The layer thicknesses of F-silane and PEG2000 silane monolayers prepared on Si-wafers are determined by ellipsometry measurements and are shown in Table 5.3. The contact angles of both surfaces are also shown in Table 5.3.

| **Surfaces** | **Thickness** (Å) | **Contact Angle** (°) |
|---|---|---|
| **F-silane** | $19.2 \pm 2.3$ | $110.2 \pm 0.5$ |
| **PEG2000** | $21.8 \pm 1.3$ | $31.8 \pm 0.5$ |

Table 5.3: Layer thickness and contact angles of F-silane and PEG2000 monolayers on Si-wafer.

### 5.6.2 Protein Adsorption Test

PAA and PEI monolayers, F-silane and PEG2000 silane were also prepared on silicon wafers to test their protein resistance properties. Fibrinogen (from bovine plasma) and lysozyme (from chicken egg white) were used for the adsorption test. The molecular weights, isoelectric points and net charges of these two proteins can be found in Table 4.7 on page 47. The protein adsorption assay followed the same protocol as described in chapter 4.

The results are shown in Figure 5.18. Compared to the alkane thiol SAMs, the PAA monolayer can effectively reduce the adsorption of fibrinogen, but on the other hand, it greatly improves the adsorption of lysozyme. In contrast, the PEI

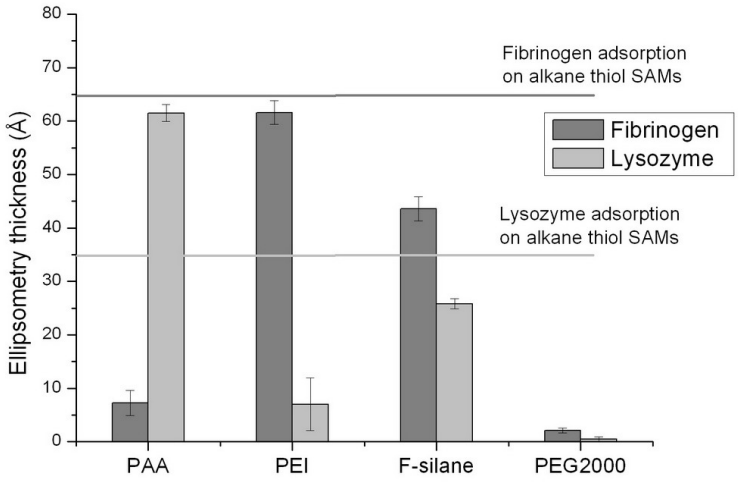


Figure 5.18: Fibrinogen and lysozyme adsorption on PAA monolayer, PEI monolayer, F-silane and PEG silane surfaces.

monolayer surface is non-resistant to the adsorption of fibrinogen but can reduce the adsorption of lysozyme. The hydrophobic F-silane surface cannot resist either fibrinogen or lysozyme. The PEG2000 silane surface is non-selectively inert to both proteins.

As already discussed in chapter 4, the charge attraction or repulsion plays an important role in the interaction with proteins. In PBS buffer (pH 7.4), the surface of the PAA monolayer is negatively charged due to the ionized carboxyl groups. Therefore, the PAA monolayer repels the negatively charged fibrinogen and attracts the positively charged lysozyme. The PEI monolayer surface is positively charged due to the ionized amino groups, so it attracts the negatively charged fibrinogen and repels the positively charged lysozyme.

The inertness of the PEG monolayer is believed to be due to the steric repulsion [104]. The heavily hydrated PEG chains in the near surface region have high conformational freedom and are random in orientation and motion, therefore protein molecules are prevented from approaching the surface.

The non-resistant behavior of the F-silane relates to its hydrophobicity and low surface energy.

## 5.7 Surface Characterization of Polyelectrolyte Multilayers

As discussed in section 5.3.3, the surface morphology of polyelectrolyte multilayers can be finely controlled by the pH of the polyelectrolyte solutions. The size of the structures on the surface and the film thickness can be altered from nanometer to micrometer range by increasing the pH of the PEI solution. The surface roughness was analyzed by atomic force microscopy (AFM).

Besides these morphological changes of the multilayers, the surface chemistry of the multilayers might also be different. Surface modifications by F-silane and PEG2000 silane certainly change the surface chemistry of the multilayers. These changes in surface chemistry were investigated by XPS and the chemical composition of the multilayer surfaces was quantitatively calculated.

The wettability of each surface was determined by contact angle measurements as described in chapter 3.

Spray coated polyelectrolyte multilayer films with four different morphologies (Figure 5.10, described in section 5.3.3), F-silane and PEG2000 silane coated multilayer films were chosen to study the effects of topography, wettability and surface chemistry on the adhesion of marine organisms in the AMBIO project.

### 5.7.1 Polyelectrolyte Multilayers (without Surface Modification)

#### Texture Analysis by Fourier Transform Image Analysis

As shown in the SEM images (Figure 5.10), surfaces of polyelectrolyte multilayers are composed of a lot of irregular 'hills and valleys' with random arrangement. The bright parts are 'hills' and the dark parts are 'valleys'. The smallest distance between two 'hills' (or 'valleys') is called the spatial texture size (or feature size).

It is possible to measure the texture size manually and individually, and finally calculate the average. But this kind of calculation is very tedious and time consuming. Since the arrangement of 'hills' and 'valleys' is random in every direction, it is difficult to decide which is the smallest distance between the peaks of two 'hills'. Therefore, the Fourier Transform image processing method was applied to analyze the SEM images of polyelectrolyte multilayers and obtain the texture size of the surfaces. The fundamental theory of the Fourier Transform image processing method is introduced in chapter 3.

SEM images with a magnification of 2000× (shown in Figure 5.19) were used for the Fourier transform analysis. At this magnification there are large amounts of features on the surface and the features are still clearly resolved, therefore a good result can be obtained. The analyzed data are plotted in Figure 5.20. The maximum of each curve gives the pronounced peak to peak maximum, therefore the corresponding value in the x-axis (in micrometer) is the distance between the 'hills' (or 'valleys'). The calculated values are listed in Table 5.4.

From the SEM pictures (Figure 5.19), we can observe that the feature size of the polyelectrolyte multilayer surface increases with increasing pH of the PEI solution. Fourier Transform analysis gives a quantitative value of the texture size (Table 5.4) and clearly shows the effect of pH on the topography of the polyelectrolyte multilayers.

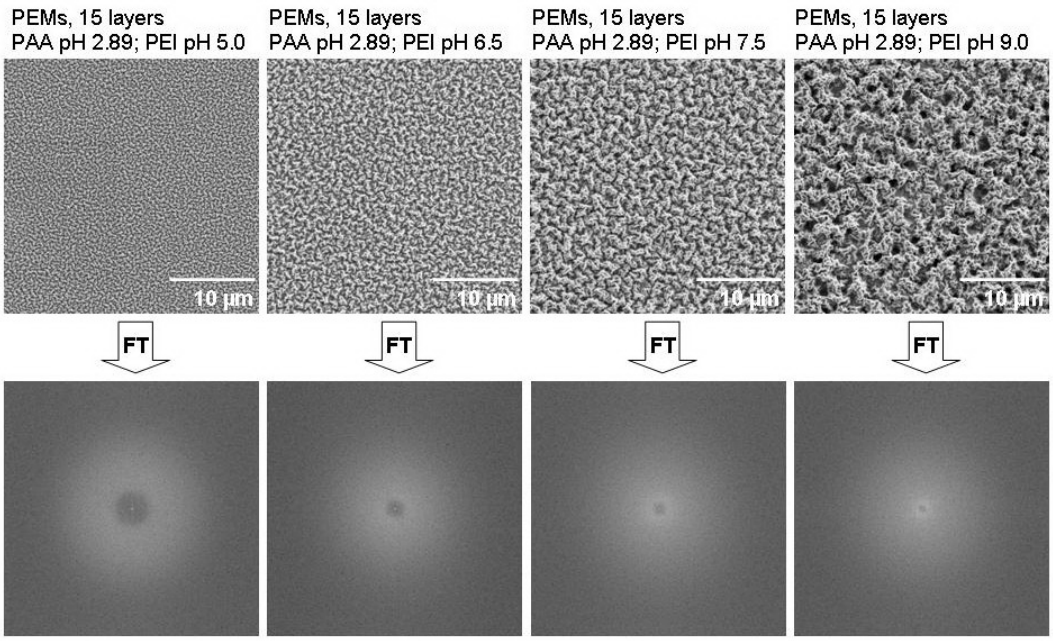


Figure 5.19: SEM topography images of polyelectrolyte multilayer surfaces ( magnification 2000×) and the corresponding Fourier transformed images.

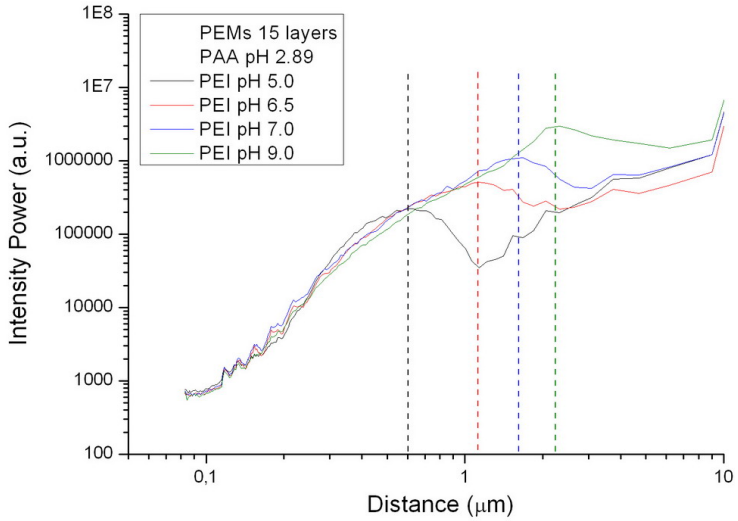


Figure 5.20: Spatial texture analysis on polyelectrolyte multilayer surfaces by Fourier transform image processing.

| Multilayers (15 layers) | Texture Size (nm) | Label |
|---|---|---|
| PAA(2.89), PEI(5.0) | $605 \pm 18$ | PEM600 |
| PAA(2.89), PEI(6.5) | $1119 \pm 70$ | PEM1100 |
| PAA(2.89), PEI(7.5) | $1645 \pm 147$ | PEM1600 |
| PAA(2.89), PEI(9.0) | $2273 \pm 282$ | PEM2300 |

Table 5.4: Surface texture size of polyelectrolyte multilayers obtained by Fourier transform image anaylsis and labels of samples.

Since the texture size is a very important parameter in the following discussion about the effects of topography on biofouling, the polyelectrolyte multilayer samples are labeled according to their texture sizes. The labels of the samples are listed in Table 5.4. For example, polyelectrolyte multilayer film with a texture size of 1119 nm is labeled as PEM1100. For the fluorinated PEM1100 sample, the label will be PEM1100F, and for the PEGylated PEM1100 sample, the label will be PEM1100P.

#### Roughness Analysis by AFM

As discussed in chapter 3, besides SEM, AFM was applied for topography imaging and surface roughness calculation. The AFM measurements of polyelectrolyte multilayers were performed by Frank Leisten at the University of Hannover.

Figure 5.21 shows the topography and section analysis of the multilayer films. In order to obtain the thickness of the films, a part of the film was removed by scratching with a scalpel to uncover the glass substrate. There is a sudden decline in the section analysis of a linear scan, the higher part is the multilayer film and the lower part in the glass substrate. The distance between the higher and lower plateaus gives the thickness of the film.

Amplitude surface roughness parameters $R_{rms}$ and $R_a$ and the film thickness of the multilayer films are listed in Table 5.5. An increase in the pH of the PEI solution results in a rougher surface and thicker film. The values of film thickness obtained from AFM measurements and SEM (see in Table 5.1) are in good agreement with each other.

| Label | Multilayers (15 layers) | $R_{rms}$ (nm) | $R_a$ (nm) | Thickness (nm) |
|---|---|---|---|---|
| PEM600 | PAA(2.89), PEI(5.0) | 34 | 28 | 316 |
| PEM1100 | PAA(2.89), PEI(6.5) | 102 | 84 | 644 |
| PEM1600 | PAA(2.89), PEI(7.5) | 146 | 119 | 841 |
| PEM2300 | PAA(2.89), PEI(9.0) | 294 | 234 | 1202 |

Table 5.5: Surface roughness and film thickness of polyelectrolyte multilayers, measured by AFM.

#### XPS Analysis of Polyelectrolyte Multilayer Surfaces

C1s, O1s, N1s and Si2p XPS spectra of the multilayer films are shown in Figure 5.22. After the deposition of multilayers on glass substrates, the Si2p peak is completely

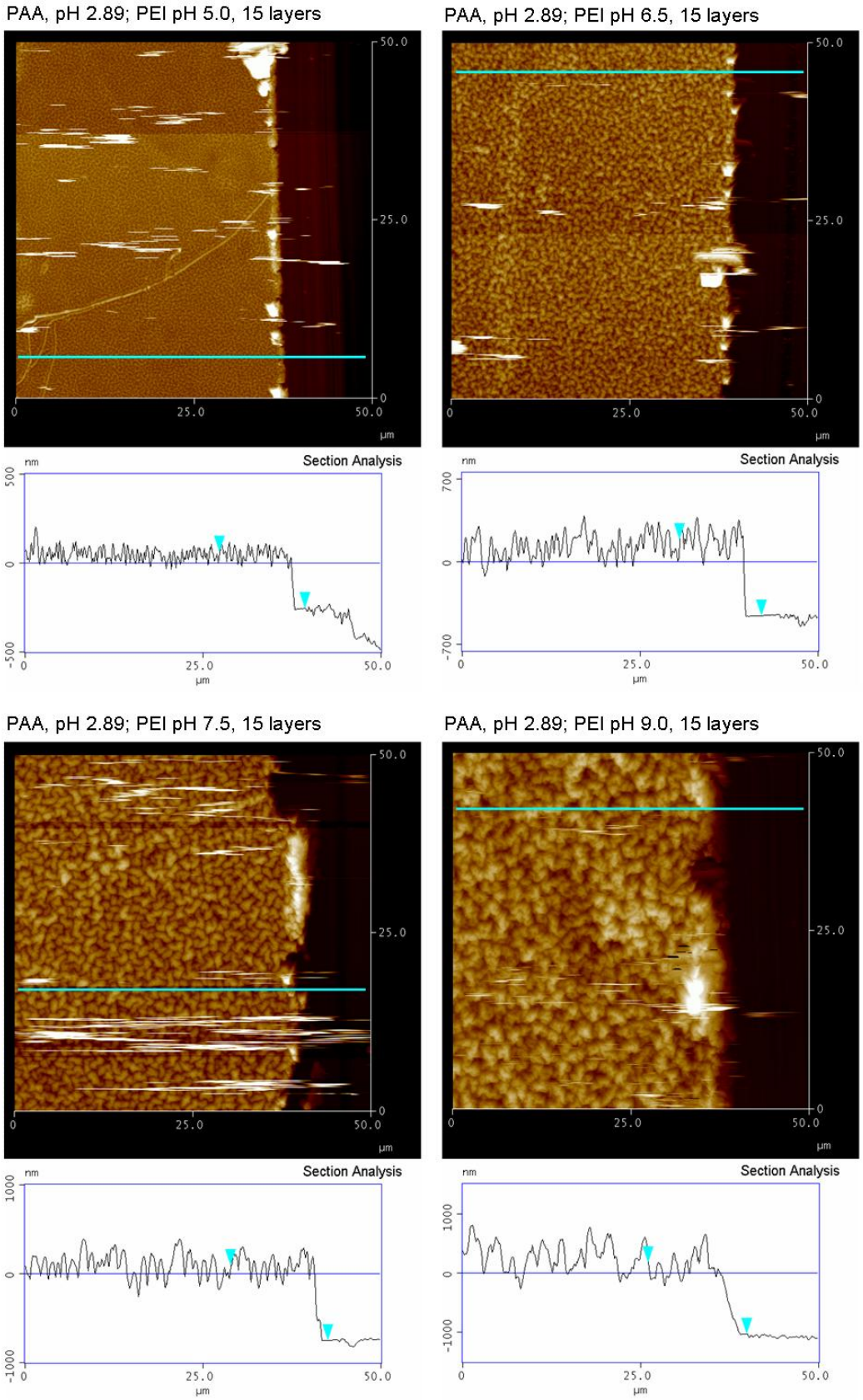


Figure 5.21: AFM picture and section analysis of polyelectrolyte multilayer films.

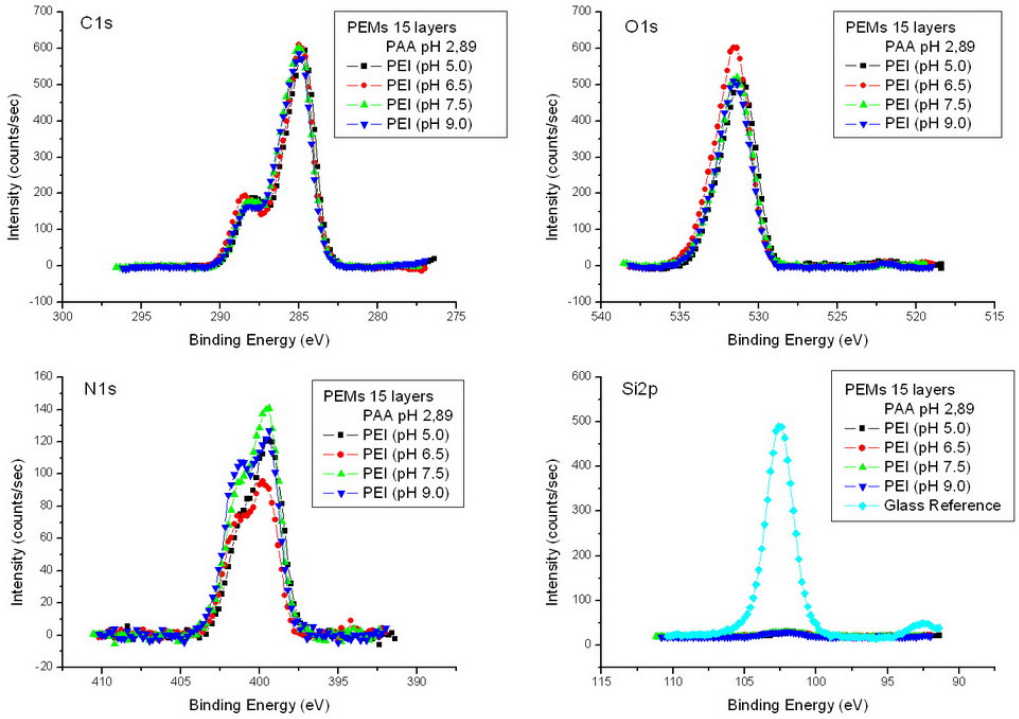


Figure 5.22: XPS spectra of polyelectrolyte multilayer films.

invisible, because the multilayers are much thicker (the thinnest film is about 300nm, in Table 5.5) than the sampling depth of XPS (about 10 nm). Therefore, XPS spectra only give information about the surface of the multilayer films. For this reason, the C1s peak intensities of the four multilayer films are almost identical, though the film thicknesses are different.

As described in section 5.3.2, though multilayer films are prepared by layer-by-layer deposition, the layers are not distinguished but rather intermixed with each other due to the diffusion of polycations during the deposition process [97, 100, 101]. Therefore, on the surface of the multilayer films, the O1s signal from PAA and the N1s signal from PEI are both observable. Small differences in peak intensity are observed in the O1s and N1s spectra from different multilayer films. These differences reveal the slight variation in the chemical composition of the multilayer surfaces. Quantitative calculation was made from XPS spectra and the results are shown in Table 5.6.

| Label | Multilayers (15 layers) | C (%) | O (%) | N (%) | Contact Angle(°) |
|---|---|---|---|---|---|
| PEM600 | PAA(2.89), PEI(5.0) | 66.2 | 24.9 | 8.8 | $56.7 \pm 2.2$ |
| PEM1100 | PAA(2.89), PEI(6.5) | 65.7 | 27.3 | 7.0 | $52.1 \pm 2.7$ |
| PEM1600 | PAA(2.89), PEI(7.5) | 66.9 | 23.0 | 10.1 | $64.7 \pm 3.0$ |
| PEM2300 | PAA(2.89), PEI(9.0) | 66.3 | 23.3 | 10.3 | $74.6 \pm 0.6$ |

Table 5.6: Chemical composition and contact angle of polyelectrolyte multilayer surfaces.

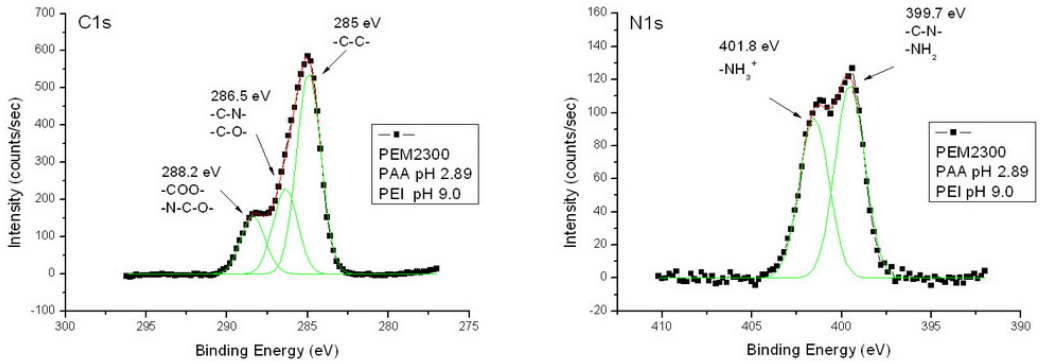


Figure 5.23: C1s and N1s XPS spectra of polyelectrolyte multilayer films PEM2300.

Since the C1s spectra of all the multilayer samples are almost identical, the C1s spectrum of sample PEM2300 is shown as an example in Figure 5.23. The C1s peak of PEM2300 can be deconvoluted as a combination of three peaks. The dominating peak at 285 eV comes from the alkyl carbon in both PAA and PEI molecules. The peak at 286.5 eV is the carbon signal from the C-N bonds in PEI molecules. The peak at 288.2 eV mainly comes from the -COOH groups in PAA molecules. The deconvolution of N1s peak of sample PEM2300 is also shown in Figure 5.23. The peak at 401.8 eV comes from the protonated amines [78], the peak at 399.7 eV originates from the unprotonated amines and the C-N bonds in PEI molecules [78, 80]. The different peak ratio between the two N1s sub-peaks induces the different N1s peak shape in Figure 5.22. The intensity ratios of the two N1s sub-peaks were calculated, but no correlation has been found between these ratios and the surface properties (e. g. texture size, chemical composition, wettability) of the multilayer samples, therefore, they are not shown in this thesis.

The contact angles of these multilayer films are also listed in Table 5.6. The wettability of the surface is related to both topography and chemistry. As shown in Figure 5.10, when the pH of PEI increases from 5.0 to 9.0, the texture size of the multilayer films also increases. Correspondingly, the contact angle of the surface also increases. The only exception is the multilayer film PEM1100. In this case, the concentration of oxygen on the surface is higher than on the other surfaces and the concentration of nitrogen is lower, which indicates that compared to the other surfaces PAA is more abundant on PEM1100. The carboxyl groups in PAA might make PEM1100 more hydrophilic than the other multilayers.

PEM1600 and PEM2300 are almost identical in surface chemical composition. The difference in contact angle of these two surfaces is certainly due to their different surface topographies.

### 5.7.2 Polyelectrolyte Multilayers with Perfluorination

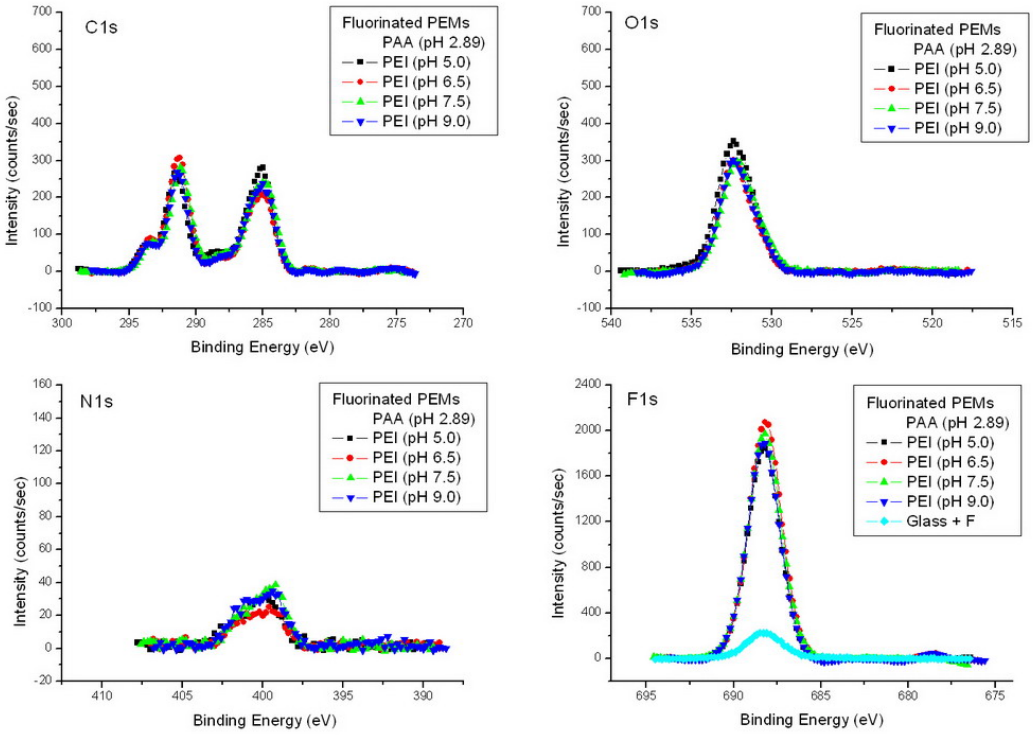


Figure 5.24: XPS spectra of polyelectrolyte multilayer films after F-silane coating.

The polyelectrolyte multilayer films discussed above were modified by F-silane to increase the hydrophobicity of the surfaces. From the XPS spectra in Figure 5.24, we can clearly find that the strong F1s peak appears and the C1s, O1s and N1s signals are greatly decreased after the fluorinated silane deposition (the x and y scale of the C1s, O1s and N1s spectra are the same as in Figure 5.22). The chemical composition of fluorinated polyelectrolyte multilayers can be found in Table 5.7. Comparing the chemical composition values in Table 5.7 and in Table 5.6, after F-silane coating, the surfaces are dominated by fluorine and the concentrations of C, O and N are greatly reduced.

| Label | Multilayers (15 layers) | C (%) | O (%) | N (%) | F (%) | Contact Angle(°) |
|---|---|---|---|---|---|---|
| PEM600F | PAA(2.89), PEI(5.0) | 40.4 | 12.6 | 1.9 | 45.1 | $120.7 \pm 1.6$ |
| PEM1100F | PAA(2.89), PEI(6.5) | 37.9 | 9.9 | 1.8 | 50.4 | $125.5 \pm 4.8$ |
| PEM1600F | PAA(2.89), PEI(7.5) | 39.6 | 10.5 | 2.4 | 47.5 | $132.6 \pm 2.3$ |
| PEM2300F | PAA(2.89), PEI(9.0) | 39.6 | 10.6 | 2.5 | 47.3 | $131.5 \pm 2.0$ |

Table 5.7: Chemical composition and contact angle of polyelectrolyte multilayer surfaces after F-Silane coating.

Compared to the F-silane coated glass, the F1s peak on the multilayer surface is much stronger (Figure 5.24). The multilayer surfaces are much rougher than the glass surface, so the surface area of multilayer films is much bigger than on glass

| Surfaces | F1s peak Intensity (counts/sec) | Ratio ($I_{F1sGlass}/I_{F1sPEMs}$) |
|---|---|---|
| F-silane (on glass) | 589.7 | 1 |
| PEM600F | 4315.1 | 7.3 |
| PEM1100F | 4886.7 | 8.3 |
| PEM1600F | 4679.6 | 7.9 |
| PEM2300F | 4411.9 | 7.5 |

Table 5.8: F1s peak intensity ratios between F-silane coated glass and F-silane coated polyelectrolyte multilayers.

slides. Therefore, more F-silane is deposited on the multilayer surfaces than on glass surface. If we assume that the F-silane coating on glass and on the multilayer surfaces is a monolayer, then, the intensity of the F1s peak is supposed to be related to the surface area of the substrates. The F1s peak intensity ratio between F-silane coated glass and F-silane coated polyelectrolyte multilayers (Table 5.8), $I_{F1sGlass}/I_{F1sPEMs}$, might indicate that the surface area of the polyelectrolyte multilayers is probably as large as about 8 times of the surface area of the glass substrates.

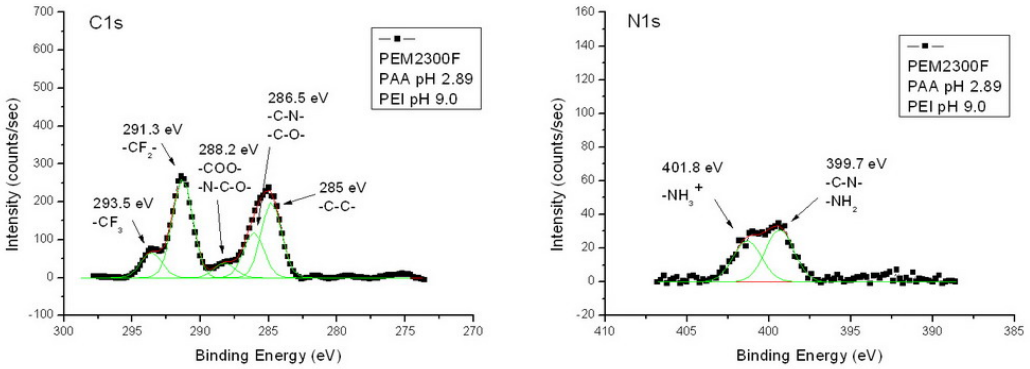


Figure 5.25: C1s and N1s XPS spectra of polyelectrolyte multilayer films PEM2300F.

In Figure 5.25, the C1s and N1s spectra of multilayer sample PEM2300F are shown as examples for the detailed analysis. Besides the decreased C1s signals from the polyelectrolyte multilayers (sub-peaks at 285 eV, 286.5 eV and 288.2 eV), two more signals (at 291.3 eV and 293.5 eV) appear in the C1s spectrum of the fluorinated multilayer sample PEM2300F. The signals at 291.3 eV and 293.5 eV come from the $-CF_2-$ and $-CF_3$ groups in the F-silane molecules, respectively. The N1s signal from the buried multilayers is greatly decreased due to the F-silane coating, but the peak is still a combination of two sub-peaks at 399.7 eV and 401.8 eV.

The contact angles of the surfaces increase a lot after fluorination (Table 5.7). Figure 5.26 shows images of a water drop on the surfaces of PEM2300 and PEM2300F. Though the wettability of the surfaces are mainly determined by the F-Silane coating in this case, the topography still has some influences. As shown in Table 5.7, after the fluorination, the two rougher surfaces (PEM1600F and PEM2300F) are slightly

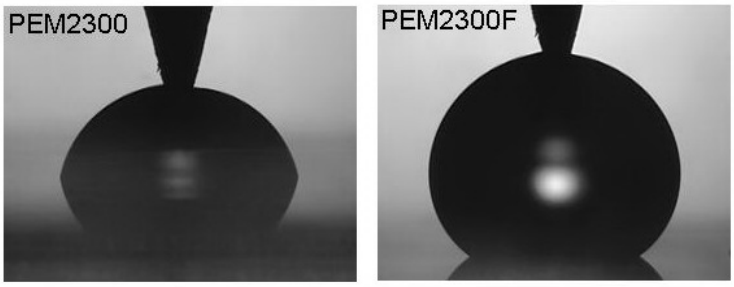


Figure 5.26: Hydrophobicity greatly increases after perfluorination: images of a water drop on PEM2300 and PEM2300F.

more hydrophobic than the two smoother surfaces (PEM600F and PEM1100F).

### 5.7.3 Polyelectrolyte Multilayers with PEGylation

Polyelectrolyte multilayer films discussed in section 5.3.3 were also modified by PEG2000 silane. The chemical composition of these surfaces was caluculated from the XPS spectra. The small differences in the C1s, O1s and N1s peaks (Figure 5.27 reveal that the chemical composition of each multilayer surface is slightly different. The concentration of C, O and N on the PEGylated multilayer surfaces are shown in Table 5.9.

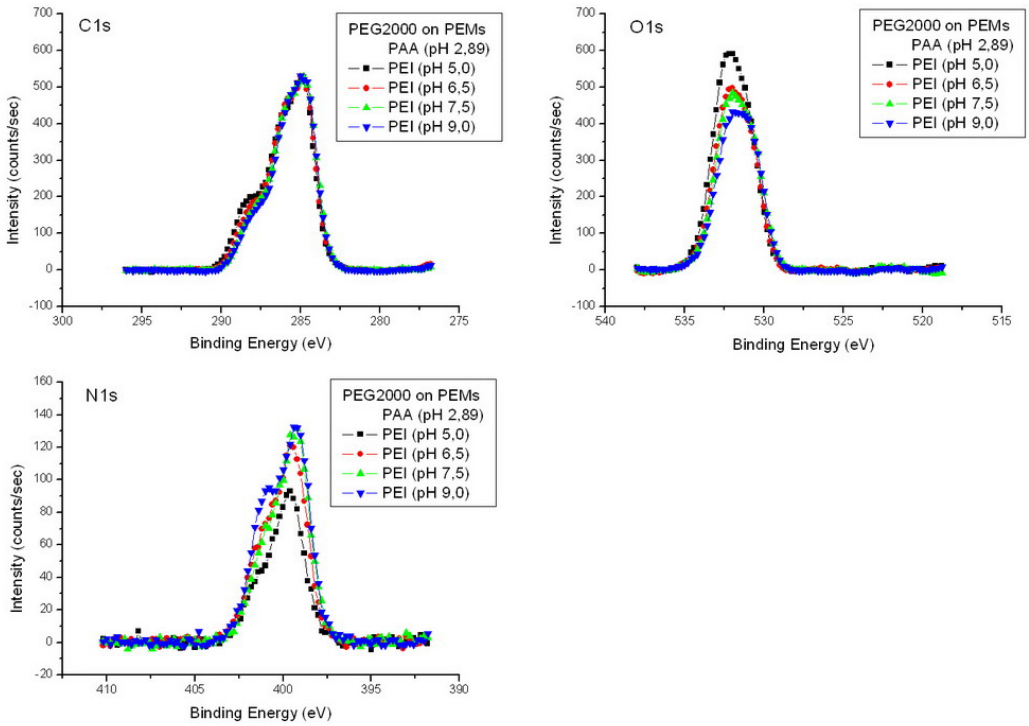


Figure 5.27: XPS spectra of polyelectrolyte multilayer films after PEG2000 silane coating.

The PEG2000 molecule is mainly composed of C and O, and both elements

| Label | Multilayers (15 layers) | C (%) | O (%) | N (%) | Contact Angle(°) |
|---|---|---|---|---|---|
| PEM600P | PAA(2.89), PEI(5.0) | 64.4 | 30.1 | 5.6 | $29.3 \pm 0.4$ |
| PEM1100P | PAA(2.89), PEI(6.5) | 65.9 | 26.0 | 8.1 | $43.1 \pm 1.3$ |
| PEM1600P | PAA(2.89), PEI(7.5) | 66.5 | 25.0 | 8.5 | $32.0 \pm 1.0$ |
| PEM2300P | PAA(2.89), PEI(9.0) | 66.3 | 23.7 | 9.7 | $66.6 \pm 0.6$ |

Table 5.9: Chemical composition and contact angle of polyelectrolyte multilayers surfaces after PEG2000 coating.

are also present on the bare multilayer surfaces, therefore, the changes in surface chemical composition induced by the PEG2000 coating are not very prominent. By comparing the values in Table 5.9 and in Table 5.6, we can find that there are differences in the concentration of C, O and N, but these differences are not significant. For the flattest multilayer film (PEM600), after PEG2000 coating, the concentration of O is increased by about 5% and N is decreased by about 3%. For the other multilayer films, the changes in the concentration of O and N are only less than 2%, which are so small that they might only be due to measurement and calculation (such as peak fitting) errors.

Although the changes in surface chemical composition do not give strong evidence for the deposition of PEG2000 silane, the obvious changes in contact angle (in Table 5.9, compared to Table 5.6) can be considered as the result of PEGylation. After PEG2000 silane deposition, the surfaces of the four multilayer films are all more hydrophilic.

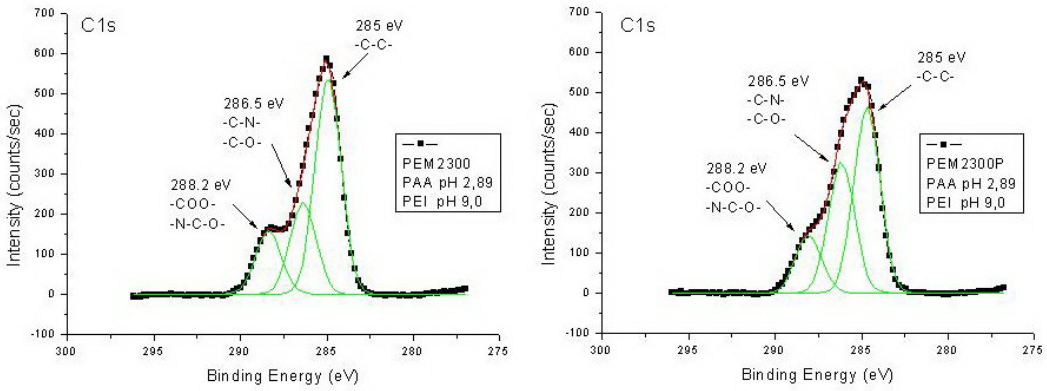


Figure 5.28: C1s XPS spectra comparison between polyelectrolyte multilayers PEM2300 (left) and PEGylated polyelectrolyte multilayers PEM2300P (right).

Compared to the surface chemical composition analysis, peak shape analysis by peak fitting gives more detailed information about the surface. Figure 5.28 is the C1s XPS spectra comparison between the multilayer film PEM2300 and the PEGylated multilayer film PEM2300P. Both C1s peak of PEM2300 and C1s peak of PEM2300P can be fitted as a combination of three sub-peaks with identical width. The peak at 285 eV originates from the alkyl carbon, the peak at 286.5 eV comes from the

carbon atoms in C-O and C-N bonds, and the peak at 288.2 eV comes from carbon atoms in carboxyl or amide groups. Due to the large amounts of carbon atoms in the ethylene glycol groups, the deposition of PEG2000 silane causes an increase of the peak at 286.5 eV and correspondingly a decrease of the peaks at 285 eV and 288.2 eV.

For the other three multilayer films, the same kind of change in peak shape has been observed. This change in peak shape indicates a successful deposition of PEG2000 silane on the multilayer surfaces.

## 5.8 Biological Evaluations

The samples listed in Table 5.10 were sent to University of Birmingham and Newcastle University for the settlement assays of Ulva spores and Barnacle cyprids. A brief introduction about the biological evaluation assays can be found in section 3.7.

| **Label** | **Descriptions** | **Contact Angle**(°) |
|---|---|---|
| F-silane | Monolayer: Fluorinated silane on glass | $78.8 \pm 1.1$ |
| PEG | Monolayer: PEG2000 silane on glass | $31.8 \pm 0.5$ |
| PEM600 | Polyelectrolyte multilayers (15 layers): PAA 3mg/mL pH 2.89; PEI 1mg/mL pH 5.0 | $56.7 \pm 2.2$ |
| PEM600F | Fluorinated silane on PEM600 | $120.7 \pm 1.6$ |
| PEM600P | PEG2000 silane on PEM600 | $29.3 \pm 0.4$ |
| PEM1100 | Polyelectrolyte multilayers (15 layers): PAA 3mg/mL pH 2.89; PEI 1mg/mL pH 6.5 | $52.1 \pm 2.7$ |
| PEM1100F | Fluorinated silane on PEM1100 | $125.5 \pm 4.8$ |
| PEM1100P | PEG2000 silane on PEM1100 | $43.1 \pm 1.3$ |
| PEM1600 | Polyelectrolyte multilayers (15 layers): PAA 3mg/mL pH 2.89; PEI 1mg/mL pH 7.5 | $64.7 \pm 3.0$ |
| PEM1600F | Fluorinated silane on PEM1600 | $132.6 \pm 1.0$ |
| PEM1600P | PEG2000 silane on PEM1600 | $32.0 \pm 1.0$ |
| PEM2300 | Polyelectrolyte multilayers (15 layers): PAA 3mg/mL pH 2.89; PEI 1mg/mL pH 9.0 | $74.6 \pm 0.6$ |
| PEM2300F | Fluorinated silane on PEM2300 | $131.5 \pm 2.0$ |
| PEM2300P | PEG2000 silane on PEM2300 | $66.6 \pm 0.6$ |
| PAA | Monolayer: PAA on glass | $19.2 \pm 2.1$ |
| PEI | Monolayer: PEI on glass | $40.5 \pm 0.8$ |

Table 5.10: Samples for biological evaluation: labels, descriptions, and water contact angles.

It must be pointed out that in this set of samples, the contact angle of the fluoriante silane coated glass (F-silane) is a bit low (Table 5.10). Normally, for the F-silane/glass sample, we can get a contact angle in the range of 90-100 °, but for the F-silane/glass surface in this set of samples, the contact angle is only about 80 °, which means the coverage of F-silane on the glass surface is a little bit low.

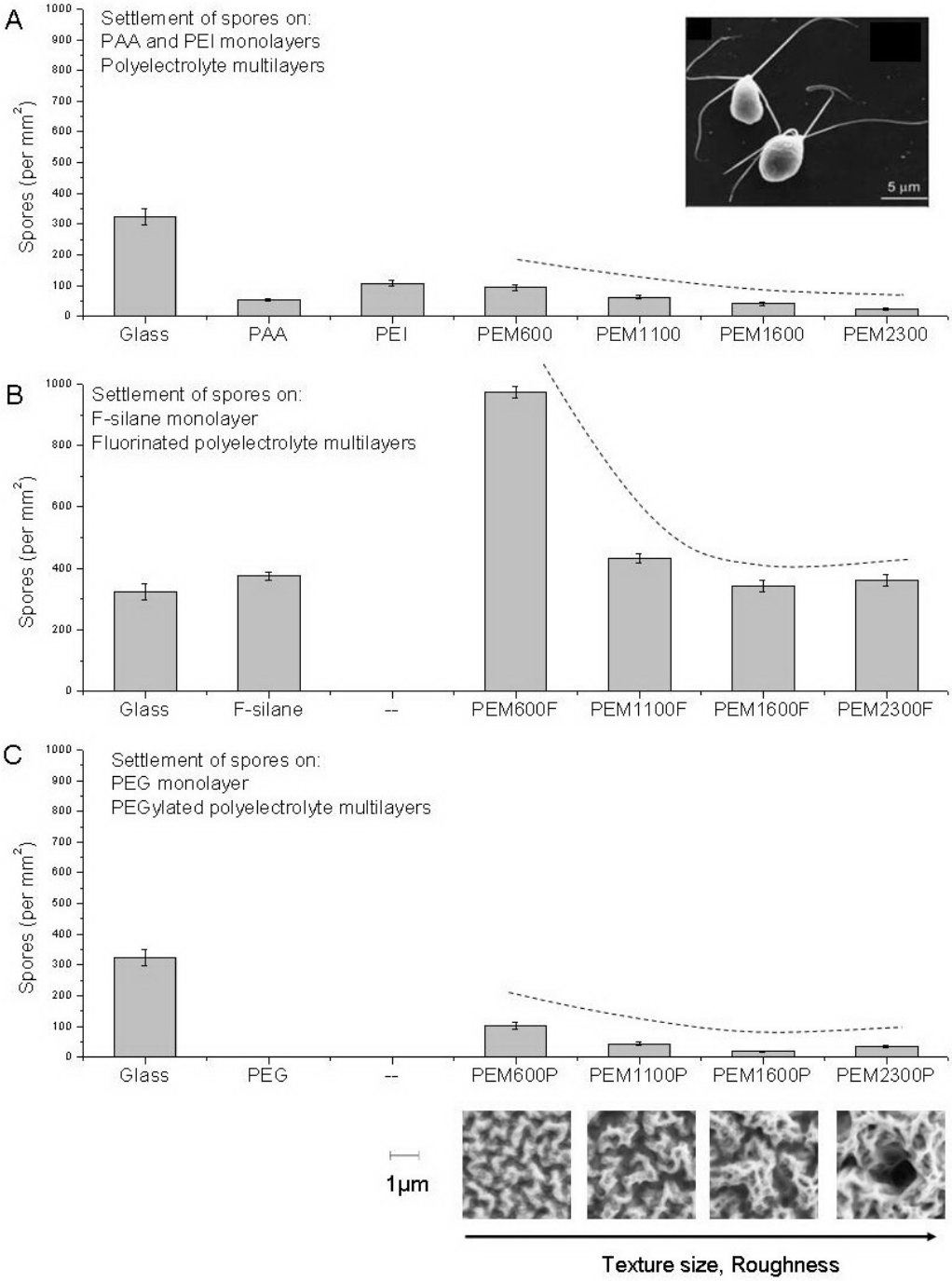


Figure 5.29: *Ulva* spores attachment on **A**: PAA and PEI monolayers and polyelectrolyte multilayers; **B**: F-silane monolayer and fluorinated polyelectrolyte multilayers; **C**: PEG monolayer and PEGylated polyelectrolyte multilayers.

### 5.8.1 Ulva Spores Settlement: (*Ulva linza*)

The densities of settled *Ulva* spores on all samples are shown in three plots in Figure 5.29. Plot A shows the spores settlement on the monolayers of PAA and PEI and the polyelectrolyte multilayers. Plot B shows the settlement of spores on the F-silane monolayer and on fluorinated multilayers. The spores settlement on PEG monolayer and PEGylated multilayers is shown in plot C. To make a clear comparison, all three plots have the same Y-scale and the spores settlement on the standard glass surface is shown in each plot.

As shown in Figure 5.29A, the spores settlement density is lower on both PAA and PEI than on glass. The different anti-adhesion behavior of PAA and PEI monolayer is probably determined by their wettability and surface charge. The four polyelectrolyte multilayers with different morphologies show resistance against the settlement of spores. A more interesting observation is that the settlement density decreases with increasing texture size and roughness of the multilayer surfaces. The highest settlement density is associated with PEM600, which has only nanoscale features on the surface. The density of settled spores is lowest on PEM2300, which has microscale features. According to the results in Table 5.6, the differences in the chemical composition of the multilayer surfaces are not very significant. Therefore, the influence of surface chemistry on the different antifouling properties of the multilayer films should be negligible. In this case, the observed trend of the settlement of spores (indicated by the dashed line) is mainly determined by the surface morphology (topography and roughness) of the multilayer films.

Compared to the glass reference, the hydrophobic fluorinated silane monolayer (F-silane) promotes the adhesion of spores (Figure 5.29B) as known from literature [105]. After the surface modification with fluorinated silane on the multilayer films, the settlement of spores is greatly enhanced (Figure 5.29B). But a similar trend of spore settlement is still observable. The highest settlement density is associated with the smoothest fluorinated multilayer surface PEM600 and for the multilayers with larger structures, the settlement of spores is lower. In this case, the settlement of spores is determined by both surface chemistry and surface morphology.

As can be seen in Figure 5.29C, the PEG monolayer almost completely resists the adhesion of spores, which is probably due to steric repulsion. But, surprisingly, none of the PEG coated multilayer films is as resistant as the PEG monolayer. The anti-adhesion performance of the PEGylated multilayers is almost the same as the unfunctionalized multilayers and the same trend is observed. Though the surface chemistry and wettability are changed after the PEG coating, the morphological effect on spores adhesion is not covered by the PEG molecules.

### 5.8.2 Barnacle Cyprids Settlement: (*Balanus amphitrite*)

Figure 5.30 shows the settlement rates of barnacle cyprids on selected samples after 24 and 48 hours incubation. Plot A shows the cyprids settlement on the PAA and PEI monolayers and polyelectrolyte multilayers. Plot B shows the settlement of cyprids on the F-silane monolayer and fluorinated polyelectrolyte multilayers. According to our colleague Schilp's work [106], barnacle cyprids do not settle on any oligo- or poly(ethylene glycol) surfaces. For this reason, PEG modified polyelectrolyte multilayers were not sent to the partners from Newcastle University for barnacle settlement evaluation. As mentioned in section 3.7, there are no foul-release assay for the settlement of barnacle cyprids.

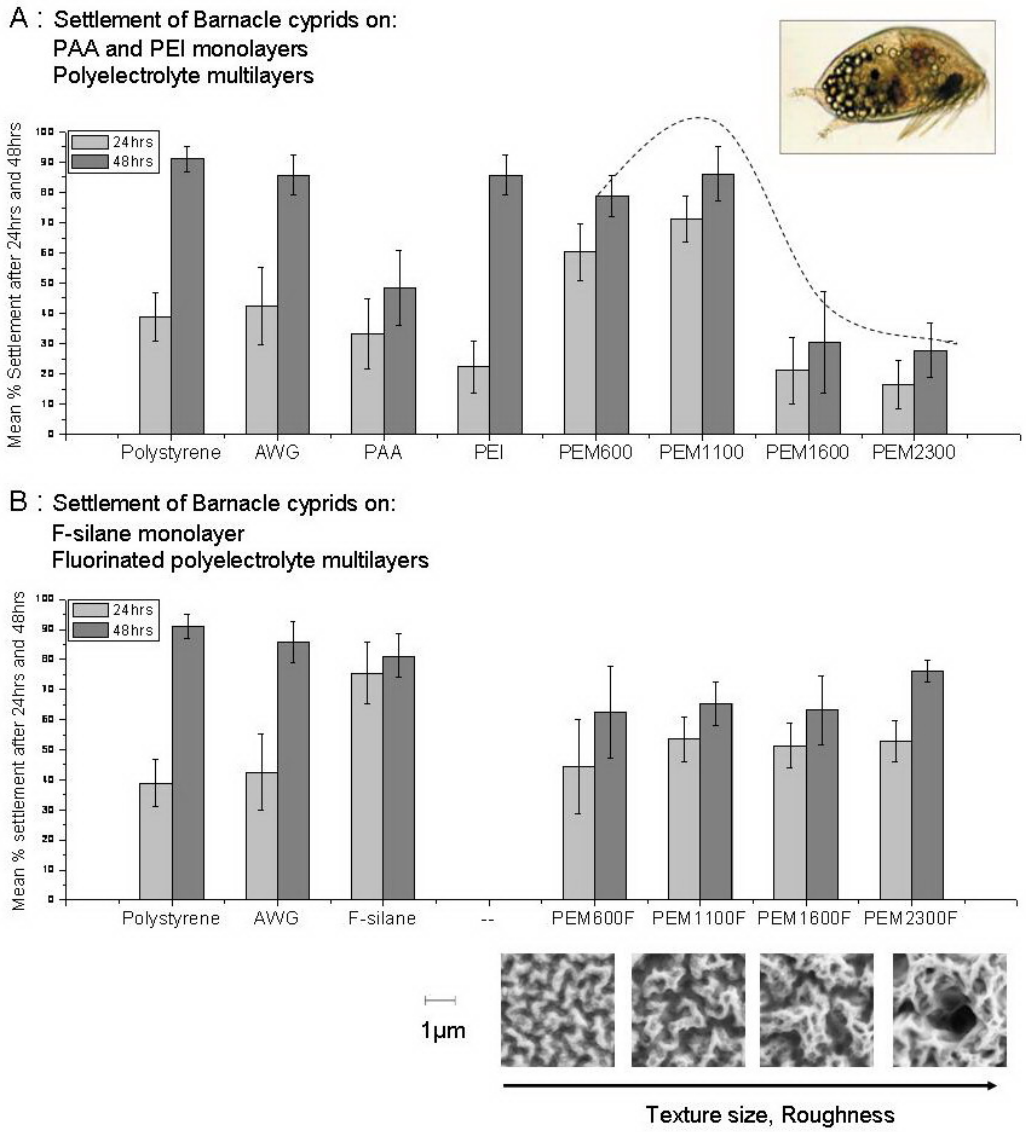


Figure 5.30: Barnacle cyprids settlement on **A**: PAA and PEI monolayers and polyelectrolyte multilayers); **B**: F-silane monolayer and fluorinated polyelectrolyte multilayers.

A 24-well plate (polystyrene) and acid washed glass slides (AWG) were included in the assay as internal standards. The cyprids settlement on the standard surfaces are shown in every plot to make the comparison clearer. All three plots in Figure 5.30 have the same Y-scale, from zero to 100%.

The partners from Newcastle University mentioned in the evaluation report that settlement rates increase with cyprid age. The very high settlement at 48 hours suggests the cyprids were 'physiologically older' than their temporal age. Therefore, the initial selective settlement stage of cyprids is better revealed from the settlement rates at 24 hours. The following discussions are focused on the results observed after 24 hours.

As shown in Figure 5.30A, cyprid settlement on PAA is slightly higher than on PEI. But the error bar suggests that this difference is not significant. Both PAA and PEI monolayers are slightly more resistance to barnacle cyprids than the standard surfaces (polystyrene and AWG). The cyprids settlement on polyelectrolyte multilayers shows clear differences. Compared to the standard surfaces, the settlement of cyprids is improved on the multilayers with smaller feature size (PEM600 and PEM1100), while on the multilayers with larger feature size and roughness (PEM1600 and PEM2300), the settlement of cyprids is reduced. It seems that the cyprids can sense the differences in surface topography and choose the most suitable surface for settlement. Among the four multilayer films with different morphologies, the sample PEM1100 with a texture size of 1.1 $\mu$m is the favored surface for barnacle cyprid settlement. The strong decrease of settlement from PEM1100 to PEM1600 is very noteworthy. The increase of feature size and roughness from PEM1100 to PEM1600 is only several hundreds of nanometers, but a significant decrease of cyprids settlement is induced by these morphological changes.

Compared to the standards, the settlement of cyprids is greatly improved by the F-silane monolayer, while the settlement of cyprids on the fluorinated multilayers is only very slightly increased (Figure 5.30B). It seems that the cyprids can not sense the morphological differences when the surface is very hydrophobic.

### 5.8.3 Bacterial Attachment (preliminary): *Cobetia marina*

A preliminary attachment test of the marine bacterium *Cobetia marina* on the fluorinated glass and polyelectrolyte multilayers were performed to examine the effect of surface topography on the smaller maine organism (*Cobetia marine* cell is about 1.3 $\mu$m in length and 660 nm wide). One slide of each surface (F-silane monolayer and fluorinarted multilayer films with four different morphologies) were tested by project partners from TNO (NL). The preliminary results are shown in Figure 5.31.

Among the fluorinated polyelectrolyte multilayer films with different topogra-

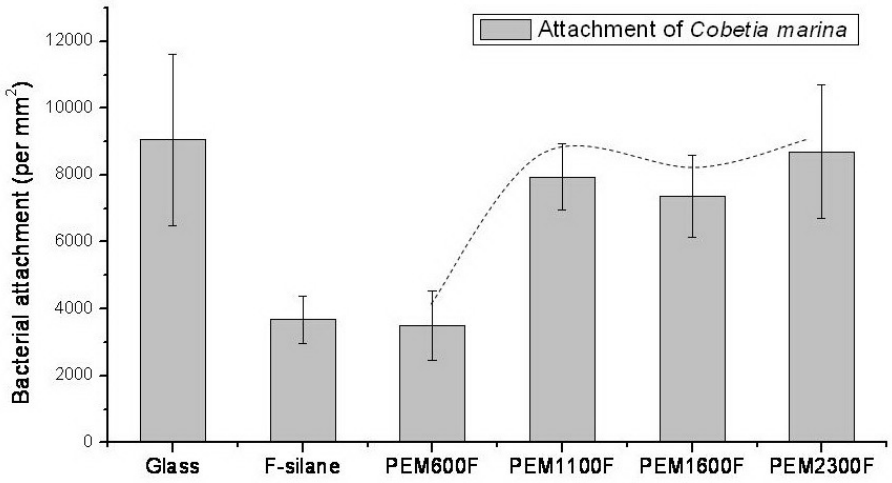


Figure 5.31: Attachment of marine bacterium *Cobetia marina* on F-silane monolayer and fluorinated polyelectrolyte multilayers.

phies, the multilayer film PEM600F with the smallest texture size and lowest roughness is the best anti-fouling surface against the attachment of *Cobetia marina*. The observed trend indicates that a surface with smaller surface structures is more effective to prevent the adhesion of smaller organisms than the surfaces with larger structures.

## 5.9 Conclusions and Discussions

Polyelectrolyte multilayers were successfully constructed by the layer-by-layer spray coating method. The surface morphology, such as the texture size, roughness and thickness, can be finely controlled by the pH value of the polyelectrolyte solutions.

The settlement of *Ulva* spores and barnacle cyprids on structured polyelectrolyte multilayer films indicates that the morphological properties of the surfaces have strong influence on the 'selective' adhesion of spores and cyprids. As shown in Figure 5.29A, the settlement density of *Ulva* spores on multilayer surfaces decreases gradually with the increase of surface feature size (from 0.6 $\mu$m to 2.3 $\mu$m, in Table 5.4) and roughness ($R_{rms}$ ranges from 30 nm to 300 nm, in Table 5.5). Barnacle cyprids can also sense the morphological difference of the surface but certainly not in the same way as the *Ulva* spores. Compared to the standards (polystyrene and AWG), more cyprids settle on the multilayer layer films with a texture size of 1 $\mu$m or smaller (PEM600 and PEM1100), while the multilayer films with a texture size of about 2 $\mu$m (PEM1600 and PEM2300) can effectively reduce the settlement of barnacle cyprids (Figure 5.30).

According to some recent studies [11, 103, 107], the length scale of the fouling organisms must be taken into consideration during the discussion about the effect

of surface topography on biofouling. The settlement of *Ulva* spores (5-7 $\mu$m) on structured PDMS surfaces with different length scales gives very interesting results. Compared to the smooth PDMS surface, the settlement of spores is greatly enhanced on the PDMS surfaces with 5-10 $\mu$m wide channels [107], while on the PDMS surfaces with only 2 $\mu$m structures and spacing (e. g. pillars, ridges, sharklets, as shown in Figure 2.7), the settlement is reduced [11, 103]. Our results demonstrate that the polyelectrolyte multilayer film with a feature size of about 2 $\mu$m is the best antifouling surface with respect to *Ulva* spores. This observation is perfectly in agreement with the results of Schumacher's work [11, 103].

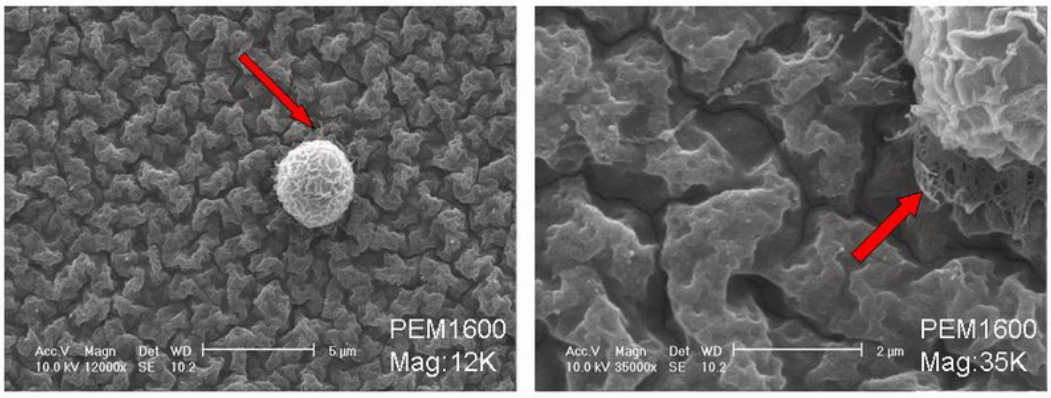


Figure 5.32: SEM images of a *Ulva* spore adhered on polyelectrolyte multilayer film PEM1600 (Spore is fixed on the surface by glutaraldehyde and critical point dried).

Figure 5.32 shows a single spore adhered on the multilayer film PEM1600 with 1.6$\mu$m texture size. The spore can neither settle into the space between two features nor on top of one feature. This might make the spore feel very 'uncomfortable'. The irregular structures might also cause some binding problem between the spore and the surface through the secreted adhesive (pointed out by the arrows in Figure 5.32).

The effect of surface topography on the adhesion of fouling organisms is explained by considering the contact area or attachment points between the organisms and the surface [108]. If the size of features (such as channels and pillars) and the spacing between the features on the surface is similar or larger than the organism, the organsim could probably fit into the features and the attachment points might increase, as a result, the adhesion would be enhanced. On the other hand, surface structures smaller than the size of the fouling organisms can probably reduce the attachment points and weaken the adhesion. Our results show that the settlement of Ulva spores (5-7 $\mu$m) is greatly reduced by the multilayer film with 2 $\mu$m structures and the attachment of *Cobetia marina* (1.3 $\mu$m in length and 660nm in width) is effectively reduced by the multilayer film with 600 nm structures. These results are good supports of the above discussed the hypothesis.

Besides the size of the features, the height of features [107, 103] and the amplitude

roughness (defined by $R_a$ and $R_{rms}$) must also have effects on the adhesion of the organism by altering the attachment points between the surface and the organism.

Besides the overall dimensions of the fouling organisms, the scale and function of their organs for surface sensoring (e. g. barnacle cyprid antennules) must also be considered [103]. The antennules of a cyprid have been studied in great detail [109, 110]. Each antennule is divided into four segments and the third segment bears the antennular attachment disc, the surface of which is covered by micro-scale cuticular villi, surrounded by an encircling velum [103]. The oval attachment disc of *Balanus amphitrite* is approximately 25-30 $\mu$m in the long axis and 15 $\mu$m in width [109, 110]. Based on the length scale of the attachment disc, biomimetic sharklet PDMS surface (Figure 2.7A) with 20 and 40 $\mu$m feature width and spacing was developed [103]. Settlement of barnacle cyprids on this specially designed PDMS surface has been greatly reduced.

The texture size of the polyelectrolyte multilayer films presented in this thesis only ranges from 0.6 $\mu$m to 2.3 $\mu$m, which is much smaller than the attachment disc of the cyprid antennules, but the topography effect on the adhesion of cyprids is still very obvious (Figure 5.30A). On the multilayer film with 1.1 $\mu$m feature size (PEM1100), the settlement of cyprids is the highest. With increasing texture size (PEM1600 and PEM2300), the settlement is greatly decreased. On the other hand, a decrease of the texture size (PEM600) also induces a reduced cyprids settlement. Though the error bar is high, the trend is observable. Following this trend, polyelectrolyte multilayers with a texture size larger than 2.3 $\mu$m or smaller into the nanometer range might also inhibit the attachment of barnacle cyprids.

Fluorination of polyelectrolyte multilayers combines the effects of topography and chemistry. The hydrophobicity of multilayer films is greatly increased (contact angle $\approx 130\,^\circ$), and as expected, the adhesions of spores and cyprids are enhanced. But these surfaces are still some distance away from the superhydrophobic surface (contact angle $> 160\,^\circ$). A further enlargement in contact angle can probably be achieved by increasing the texture size and roughness of the polyelectrolyte multilayers. Evaluations on the foul-release properties of these hydrophobic surfaces are of interest and will be performed soon.

The PEG monolayer is completely resistant to the adhesion of *Ulva* spores, while the performance of polyeletrolyte multilayers is worse than the PEG monolayer and the performance is not improved by the PEG modification (Figure 5.29C). According to the study by Unsworth et.al. [111] on PEG-SAMs, the high packing density induces a loss of molecular conformational flexibility and chain mobility and results in lower resistance against the adsorption of fibrinogen and lysozyme. But this theory is probably not suitable to explain the settlement of spores on PEGylated

multilayers. If PEG molecules are very densely packed on the multilayer surface, the concentration of N on the surface must be strongly decreased. But actually, the XPS results show that the decrease of N concentration on multilayer surfaces is only about 2% after PEG modification, which probably indicates that the packing density or the coverage of the PEG molecules on the multilayer films is fairly low. For this reason, the PEGylated multilayers have almost the same performance as the bare multilayers with respect to the settlement of *Ulva* spores, which is mainly determined by the surface topography rather than the surface chemistry.

# Chapter 6

# Conclusions and Outlook

Smooth and structured polyelectrolyte surfaces were developed and characterized. Their performance as antifouling surfaces with respect to a range of selected marine organisms were tested.

Three polysaccharides, Hyaluronic acid (HA), Alginic acid (AA), and Pectic acid (PA) were successfully coupled to glass and silicon surfaces through covalent bonding, which was verified by XPS and spectral ellipsometry. The results of protein adsorption tests reveal that the interactions between polysaccharide coatings and proteins are mainly determined by the charge and steric effects. The negative charges on the surface and the crosslinked molecular network created by inter- and intramolecular hydrogen bonding make the polysaccharide coatings resistant to negatively charged proteins or proteins with large molecular size. But positive charged small proteins, such as lysozyme, are able to adsorb on the polysaccharide surfaces. The polysaccharide-protein interaction is influenced by small ions, especially by $Ca^{2+}$. Adsorption of calcium by polysaccharide molecules probably abrogates the 'matrix' by disturbing the hydrogen bonds [65] and induces chain-chain interactions [66, 87], and consequently creates more suitable sites for the adsorption of lysozyme.

Though the three polysaccharide coatings have similar behaviors in the resistance of protein adsorption and cell adhesion, their performances in the settlement of marine organisms are obviously different. Among the three coatings, HA has the best anti-fouling and foul-release properties, which are supposed to be related to its weak interaction with calcium and its gel-like nature in water [68]. AA and PA coatings are highly similar in surface properties, while their anti-fouling performances against certain organisms (e. g. *Ulva* spores) are significantly different. The changes in elastic properties after the adsorption of calcium [112], which might be induced by different molecular conformations (especially, the linkage of repeating units in the molecules), could be an explanation.

Though none of the three polysaccahride coatings can be considered as an anti-

fouling or foul-release coating in general, the study of these three polysaccharide coatings reveals that biological adhesion on a surface is a complex process, the anti-adhesion performance of a surface is determined by a lot of parameters, and many of them are closely related to the surface chemistry. As a conclusion from this study, the hydrophilic surface coating which has strong swelling behavior in water and does not actively interact with ions (such as calcium) can probably reduce the settlement and adhesion strength for some marine organisms.

PAA/PEI polyelectrolyte multilayers with hierarchical surface structures were constructed by layer-by-layer spray coating method. The effects of deposition time, number of layers, and especially the pH value of the polyelectrolyte solution on the surface structures have been intensively studied. By tuning the pH of the PEI solution, the topographical properties of the multilayer films, such as texture size, film roughness and thickness, can be finely controlled.

Settlements of *Ulva* spores and barnacle cyprids on polyelectrolyte multilayers were performed to study the effect of topography. The results demonstrate that settlements of spores and cyprids are much lower on the multilayers with larger texture size ($\approx 2$ $\mu$m) and higher roughness ($R_a > 100$ nm). Attachment points theory [108] is applied to explain the effect of topography on the settlement of marine organisms. Attachment points between the organisms and the surface are minimized by those hierarchical structures with proper lateral size (texture size) and vertical height (roughness), therefore, the adhesion is weakened.

Obviously, the attachment points are not only determined by the size of the structures on the surface, but also by the size of the organisms themselves. Therefore, the settlement of smaller organisms, such as bacteria, on the polyelectrolyte multilayers presented in this thesis is highly interesting. The preliminary result of *Cobetia marina* attachment on the multilayer films gives a good indication about the effects of the structure size. On the other hand, the settlement of spores and cyprids on multilayer films with larger structures is also interesting. These larger structures are supposed to be able to be obtained by altering the pH of PAA solution or by increasing the ionic strength of the polyelectrolyte solution. These further experiments have already been planned and will be performed.

Finally, considering the broad range of marine organisms, their adaptable nature and the range of bioadhesives they employ [12], it seems to be impossible that a completely and universally non-fouling coating is determined only by one special surface property. In order to achieve an effective anti-fouling or foul-release surface coating, many properties have to be optimized and applied together through chemistry, physics, biology and technological engineering.

# Appendix A

## A.1 SEM Images

SEMs images of polyelectrolyte multilayers with 45° tilting angle are shown in figure A.1, which give better three-dimensional view of the hierarchical structures on the surfaces:

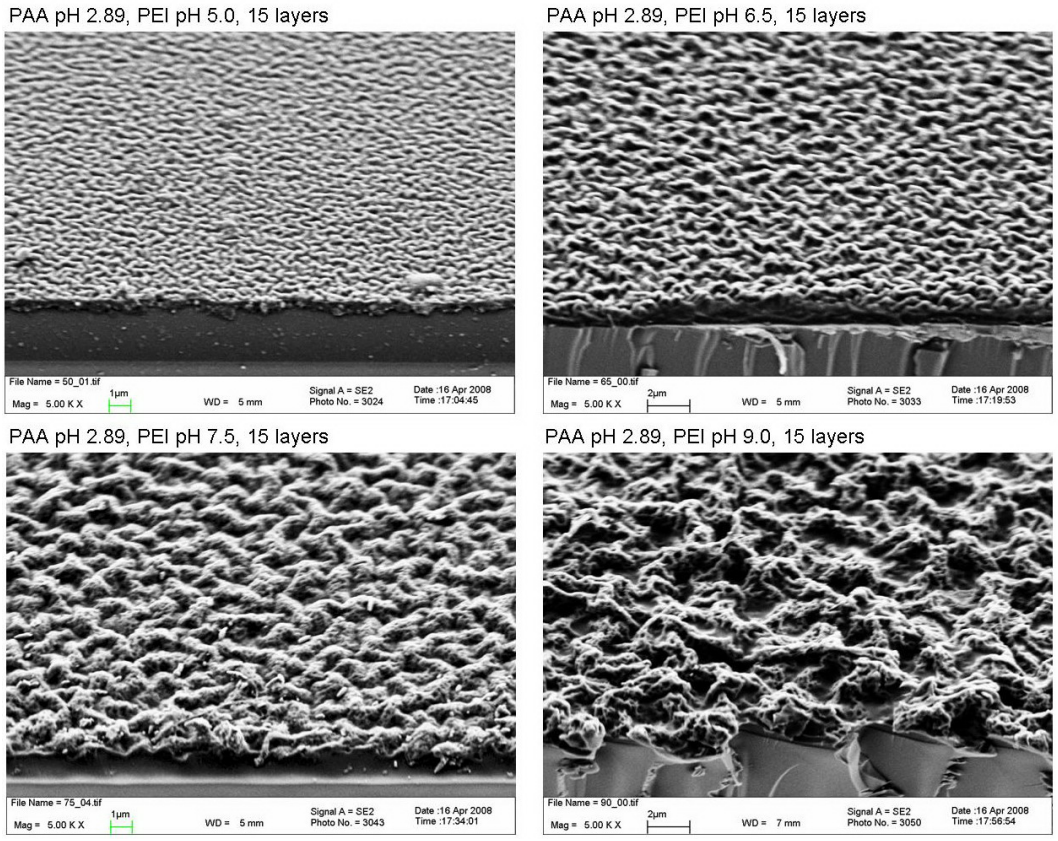


Figure A.1: SEMs images of polyelectrolyte multilayers with 45° tilting angle, Mag=5000

## A.2 Abbreviations

| | |
|---|---|
| AA | Alginic Acid |
| AFM | Atomic Force Microscope |
| AMBIO | Advanced Nanostructured Surfaces for the Control of Biofouling |
| APTES | 3-Aminopropyltriethoxysilane |
| ASW | Artificial seawater |
| AWG | Acid Washed Glass |
| BSA | Albumin from Bovine Serum |
| CVD | Chemical Vapor Deposition |
| CFU | Colony-Forming Units |
| DMF | Dimethylformamide |
| EDC | N-(3-Dimethylaminopropyl)-N'-ethylcarbodiimide |
| EDTA | Ethylenediaminetetraacetic acid |
| EPS | Extracellular Polymeric Substances |
| Fib | Fibrinogen |
| F-silane | Fluorinated silane, (Tridecafluoroctyl)triethoxysilane |
| FT | Fourier Transform |
| HA | Hyaluronic Acid (Hyaluronan) |
| HEPES | 4-(2-Hydroxyethyl)piperazine-1-ethanesulfonic acid |
| Lys | Lysozyme |
| NHS | N-Hydroxysuccinimide |
| PA | Pectic Acid (Polygalacturonic acid) |
| PAA | Poly(acrylic acid) |
| PBS | Phosphate Buffered Saline |
| PDMS | Polydimethylsiloxane |
| PEI | Polyethylenimine |
| PEG | Poly(ethylene glycol) |
| PEMs | Polyelectrolyte Multilayers |
| PK | Pyruvate Kinase |
| RFU | Relative Fluorescence Units |
| SAMs | Self-assembled Monolayers |
| SEM | Scanning Electron Microscope |
| XPS | X-ray Photoelectron Spectroscopy |

# Bibliography


[1] Jonas D. Mendelsohn, Sung Yun Yang, JeriAnn Hiller, Allon I. Hochbaum, and Michael F. Rubner. Rational design of cytophilic and cytophobic polyelectrolyte multilayer thin films. *Biomacromolecules*, 4:96–106, 2003.

[2] Maureen E Callow and James A Callow. Marine biofouling: a sticky problem. *Biologist*, 49:1–5, 2002.

[3] Axel Rosenhahn, Thomas Ederth, and Michala E. Pettitt. Advanced nanostructures for the control of biofouling: The fp6 eu integrated project ambio. *Biointerphases*, 3(1):IR1–IR5, 2008.

[4] Chakravarthy S. Gudipati, John A. Finlay, James A. Callow, Maureen E. Callow, and Karen L. Wooley. The antifouling and fouling-release perfomance of hyperbranched fluoropolymer (hbfp)-poly(ethylene glycol) (peg) composite coatings evaluated by adsorption of biomacromolecules and the green fouling alga ulva. *Langmuir*, 21:3044–3053, 2005.

[5] Macro Morra and Clara Cassinelli. Non-fouling properties of polysaccharide-coated surfaces. *J. Biomaterials Science, Polymer Edn*, 10(10):1107–1124, 1999.

[6] Macro Morra. Engineering of biomaterials surfaces by hyaluronan. *Biomacromolecules*, 6:1205–1223, 2005. AMBIO.

[7] Jan Genzer and Kirill Efimenko. Recent developments in superhydrophobic surfaces and their relevance to marine fouling: a review. *Biofouling*, 22(5):339–360, 2006.

[8] J. Verran and R. D. Boyd. The relationship between substratum surface roughness and microbiological and organic soiling: a review. *Biofouling*, 17(1):59–71, 2001.

[9] A. Kerr and M. J. Cowling. The effects of surface topography on the accumulation of biofouling. *Philosophical Magazine*, 83:2779–2795, 2003.

[10] Michelle. Carman, Thomas G. Estes, Adam W. Feinberg, James F. Schumacher, Wade Wilkerson, Leslie H. Wilson, Maureen E. Callow, James A. Callow, and Anthony B. Brennan. Engineered antifouling microtopographies: correlating wettability with cell attachment. *Biofouling*, 22:11–21, 2006.

[11] James F. Schumacher, Michelle L. Carman, Thomas G. Estes, Adam W. Feinberg, Leslie H. Wilson, Maureen E. Callow, James A. Callow, John A. Finlay, and Anthony B. Brennan. Engineered antifouling microtopographies: effect of

feature size, geometry, and roughness on settlement of zoospores of the green alga ulva. *Biofouling*, 23:55–62, 2007.

[12] J. A. Callow and M. E. Callow. *The Ulva sproe adhesive system. In: Biological Adhesives.* Springer Berlin, 2006.

[13] W.G. Characklis. *Biofilms*, volume Modeling the initial events in biofilm accumulation. John Wiley & Sons, New York, 1990.

[14] R. Breur. *Fouling and Bioprotection of Metals: Monitoring and control of deposition processes in aqueous environment.* PhD thesis, Technical University Delft, The Netherlands, 2001.

[15] Van Loosdrecht, J. Lyklema, W. Norde, G. Schraa, and A. Zehnder. Electrophoretic mobility and hydrophobicity as a measure to predict the initial steps of bacterial adhesion. *Appl. Environ. Microbiol.*, 53:1898–1901, 1987.

[16] Flemming and Wingender. Relevance of microbial polymeric substances (epss) part i: Structural and ecological aspects. *Water Sci. Technol.*, 43:1–8, 2001.

[17] *AMBIO Biological Evaluation Workshop Handbook.*

[18] A. Chiovitti, T. M. Dugdale, and R. Wetherbee. *Diatom adhesives: molecular and mechanical properties. In: Biological Adhesives.* Springer Berlin, 2006.

[19] L. A. Edgar and J. D. Pickett-Heaps. Diatom locomotion. *Prog. Phycol. Res*, 3:47–88, 1984.

[20] R. Wetherbee, J. L. Lind, J. Burke, and R. S. Quantrano. The first kiss: establishment and control of initial adhesion by raphid diatoms. *J. Phycol*, 34:9–15, 1998.

[21] N. C. Poulsen, I Spector, T. P. Spurck, T. F. Schultz, and R. Wetherbee. Diatom gliding is the result of an actin-myosin motility system. *Cell motility and the cytoskeleton*, 44(1):23–33, 1999.

[22] K. D. Hoagland, J. R. Rosowski, M. R. Gretz, and S. C. Roener. Diatom extracellular polymeric substances: function, fine structure, chemistry, and physiology. *J. Phycol*, 29:537–566, 1993.

[23] T. M. Dugdale, R. Dagastine, A. Chiovitti, and R. Wetherbee. Diatom adhesive mucilage contains distinct supramolecular assemblies of a single modular protein. *Biophysical Journal*, 90(8):2987–2993, 2006.

[24] J. A. Finlay, M. E. Callow, M. P. Schultz, G. W. Swain, and J. A. Callow. Adhesion strength of settled spores of the green alga enteromorpha. *Biofouling*, 18:251–256, 2002.

[25] J. Bowen, M. E. Pettitt, K. Kendall, G. J. Leggett, J. A. Preece, M. E. Callow, and J. A. Callow. The influence of surface lubricity on the adhesion of navicula perminuta and ulva linza to alkanethiol self-assembled monolayers. *Journal of the Royal Society, Interface*, 4(14):473–477, 2007.

[26] R. Holland, T. M. Dugdale, R. Wetherbee, A. B. Brennan, J. A. Finlay, J. A. Callow, and M. E. Callow. Adhesion and motility of fouling diatoms on a silicone elastomer. *Biofouling*, 20(6):323–329, 2004.

[27] A. Chiovitti, M. J. Higgins, R. E. Harper, R. Wetherbee, and A. Bacic. The complex polysaccharides of the raphid diatom pinnularia viridis (bacillariophyceae). *J. Phycol*, 39:543–554, 2003.

[28] B. J. Bellinger, A. S. Abdullahi, M. R. Gretz, and G. J. C. Underwood. Biofilm polymers: relationship between carbohydrate biopolymers from estuarine mudflats and unialgal cultures of benthic diatoms. *Aquat. Microbial. Ecol*, 38:169–180, 2005.

[29] Maureen E. Callow, J. A. Callow, Linnea K. Ista, Sarah E. Coleman, Aleece C. Nolasco, and Gabriel P. Lopez. Use of self-assembled monolayers of different wettabilities to study surface selection and primary adhesion processes of green algal (enteromorpha) zoospores. *Applied and Environmental Microbiology*, 66(8):3249–3254, 2000.

[30] M. K. Chaudhury, S. Daniel, M. E. Callow, J. A. Callow, and J. A. Finlay. Settlement behavior of swimming algal spores on gradient surfaces. *Biointerphases*, 1(1):18–21, 2006.

[31] Kei Kamino. *Barnarcle Underwater Attachment. In Biological Adhesives.* Springer Berlin, 2006.

[32] Ioannis K. Konstantinou, editor. *Antifouling Paint Biocides.* Springer-Verlag Berlin Heidelberg, 2006.

[33] Miriam Cohen, Eugenia Klein, Benjamin Geiger, and Lia Addadi. Organization and adhesive properties of the hyaluronan pericellular coat of chondrocytes and epithelial cells. *Biophysical Journal*, 85:1996–2005, 2003.

[34] G. Mathe, A. Albersdoerfer, K. R. Neumaier, and E. Sackmann. Disjoining pressure and swelling dynamics of thin adsorbed polymer films under controlled hydration conditions. *Langmuir*, 15:8726–8735, 1999.

[35] J. Israelachvili and H. Wennerstrom. Role of hydration and water structure in biological and collaidal interactions. *Nature*, 379:219–224, 1996.

[36] Marco Morra and Clara Cassinelli. Surface studies on a model cell-resistant system. *Langmuir*, 15:4658–4663, 1999.

[37] R. Dhamodharan and Thomas J. McCarthy. Adsorption of alginic acid and chondroitin sulfate-a to amine functionality introduced on polychlorotrifluoroethylene and glass surfaces. *Macromolecules*, 32:4106–4112, 1999.

[38] Sara Spadoni, Olga Zabotina, Adele Di Matteo, Joern Dalgaard Mikkelsen, Felice Cervone, Giulia De Lorenzo, Benedetta Mattei, and Daniela Bellincampi. Polygalacturonase-inhibiting protein interacts with pectin through a binding site formed by four clustered residues of arginine and lysine. *Plant Physiolog*, 141:557–564, 2006.

[39] Johan M. Berg, L. G. Tomas Eriksson, Per M. Claesson, and Kari Grete Nordli Borve. Three-component langmuir-blodgett films with a controllable degree of polarity. *Langmuir*, 10(4):1225–1234, 1994.

[40] Erwin A. Vogler. Sturcture and reactivity of water at biomaterial surfaces. *Advances in Colloid and Interface Science*, 74:69–117, 1998.

[41] Linnea K. Ista, Maureen E. Callow, John A.Finlay, Sarah E. Coleman, Aleece C. Nolasco, Robin H. Simons, James A. Callow, and Gabriel P. Lopez. Effect of substratum surface chemistry and surface energy on attachment of marine bacteria and algal spores. *Applied and Environmental Microbiology*, 70(7):4151–4157, 2004.

[42] James F. Schumacher, Christopher J. Long, Maureen E. Callow, John A. Finlay, James A. Callow, and Anthony B. Brennan. Engineered nanoforce gradients for inhibition of settlement (attachment) of swimming algal spores. *Langmuir*, 24:4931–4937, 2008.

[43] C. Baum, W. Meyer, R. Stelzer, L.-G. Fleischer, and D. Siebers. Average nanorough skin surface of the pilot whale (globicephala melas, delphinidae): considerations on the self-cleaning abilities based on nanoroughness. *Marine Biology*, 140:653–657, 2002.

[44] C. H. Porcel, A. Izquierdo, V. Ball, G. Decher, J.-C. Voegel, and P. Schaaf. Ultrathin coatings and (poly(glutamic acid)/polyallylamine) films deposited by continuous and simultaneous spraying. *Langmuir*, 21:800–802, 2005.

[45] John C. Vickerman, Rod Wilson, Buddy Ratner, David Castner, and Hans Joerg. *Surface Analysis: The Principal Techniques*. John Wiley & Sons, 1997.

[46] B. K. Agarwal. *X-ray Spectroscopy: An Introduction*, volume 15 of *Springer Series in Optical Sciences*. Springer-Verlag, 2nd edition, 1991.

[47] J.J.Sakurai. *Modern Quantum Mechanics*. Addison-Wesley, 1994.

[48] SPECS: surface Analysis and Computer Technology. *SpecsLab: Data Acquisition and Processing Tool*.

[49] Jacques Bluemmel. *Entwicklung biofunktionalisierter Nanostrukturen an Grenzflaechen zur Untersuchung der Kinetik des molekularen Motorproteins Eg5*. PhD thesis, Ruprecht-Karls-Universitaet Heidelberg, July 2005.

[50] Graham C. Smith. *Surface Analysis by Electron Spectroscopy: Measurement and Interpretation*. Plenum Press, New York and London, 1994.

[51] Abraham Marmur. Super-hydrophobicity fundamentals: implications to biofouling prevention. *Biofouling*, 22:107–115, 2006.

[52] T. Young. An assay on the cohesion of fluids. *Philos. Trans. R. Soc. Lond*, 95:65–87, 1805.

[53] A. Cassie and S. Baxter. Wettability of porous surfaces. *Trans. Faraday. Soc*, 40:546–551, 1944.

[54] R. N. Wenzel. Resistance of solid surfaces to wetting by water. *Ind. Eng. Chem*, 28:988–994, 1936.

[55] A. W. Neumann and Jan. K. Spelt, editors. *Applied Surface Thermodynamics*. Marcel Dekker Ltd, 1996.

[56] J. A. Woollam Co., Inc. *Guide to Using WVASE32: Software for VASE and M-44 Ellipsometers.*

[57] Vladimir G. Bordo and Horst-Guenter Rubahn. *Optics and Spectroscopy at Surfaces and Interfaces.* WiLey-VCH, 2005.

[58] Patrick Koelsch. *Static and dynamic properties of soluble surfactants at the air/water interface.* PhD thesis, Universitaet Potsdam, 2005.

[59] J.A. Woollam Co. Inc. *Hardware Manual: M-44(TM) Ellipsometer*, July 1998.

[60] F.A. Jenkins and H.E. White. *Fundamentals of Optics.* McGraw-Hill, Inc., 1981.

[61] Ray F. Egerton. *Physical Principles of Electron Microscopy.* Springer, 2007.

[62] Wikipedia. Roughness. *http://en.wikipedia.org/wiki/Roughness.*

[63] Wilhelm Burger and Mark James Burge, editors. *Digital Image Processing.* Springer, 1st edition, 2008.

[64] M. P. Schultz, J. A. Finlay, M. E. Callow, and J. A. Callow. A turbulent channel flow apparatus for the determination of the adhesion strength of microfouling organisms. *Biofouling*, 15:243–251, 2000.

[65] B. Casu, H. Chanzy, R. Vuong, W. Mackie, I. A. Nieduszynski, D. H. Isaac, V.S.R. Rao, and Margaret Biswas. *Polysaccharides: Topics in Structure and Morphology.* VCH Publishers, 1985.

[66] Isabelle Braccini, Robert P. Grasso, and Serge Perez. Conformational and configurational features of acidic polysaccharides and their interactions with calcium ions: a molecular modeling investigation. *Carbohydrate Research*, 317:119–130, 1999.

[67] P. A. Williams, C. Sayers, C. Viebke, C. Senan, J. Mazoyer, and P. Boulenguer. Elucidation of the emulsification properties of sugar beet pectin. *J. Agric. Food Chem.*, 53:3592–3597, 2005.

[68] A. Albersdoerfer and E. Sackmann. Swelling behavior and viscoelasticity of ultrathin grafted hyaluronic acid films. *The European Physical Journal B*, 10:663–672, 1999.

[69] J. Duchet, B. Chabert, J. P. Chapel, J. F. Gerard, J. M Chovelon, and N. Jaffrezic-Renault. Influence of the deposition process on the structure of grafted alkylsilane layers. *Langmuir*, 13:2271–2278, 1997.

[70] Gerald L. Witucki. A silane primer: Chemistry and applications of alkoxy silanes. *Journal of Coatings Technology V*, 65:57–60, July 1993.

[71] Jun ichi Ida, Tatsushi Matsuyama, and Hideo Yamamoto. Surface modification of a ceramic membrane by the spcp-cvd method suitable for enzyme immobilization. *Journal of Electrostatics*, 49:71–82, 2000.

[72] Satu Ek, Eero Iiskola, Lauri Niinisto, Jari Vaittinen, Tuula Pakkanen, Jetta Keranen, and Aline Auroux. Atomic layer deposition of a high-density aminopropylsiloxane network on silica through sequential reactions of $\gamma$-aminopropyltrialkoxysilanes and water. *Langmuir*, 19:10601–10609, 2003.

[73] Satu Ek, Eero I Iiskola, and Lauri Niinisto. Gas-phase deposition of aminopropylalkoxysilanes on porous silica. *Langmuir*, 19:3461–3471, 2003.

[74] John Comyn. *Adhesion Science.* The Royal Society of Chemistry, 1997.

[75] Abraham Ulman. Formation and structure of self-assembled monolayers. *Chem. Rev*, 96:1533–1554, 1996.

[76] Ranee A. Stile and Kevin E. Healy. Thermo-responsive peptide-modified hydrogels for tissue regeneration. *Biomacromolecules*, 2:185–194, 2001.

[77] Carel T.M. Fransen, Simon R. Haseley, Miranda M.H. Huisman, Henk A. Schols, Alphons G.J. Voragen, Johannis P. Kamerling, and Johannes F.G. Vliegenthart. Studies on the structure of a lithium-treated soybean pectin: characteristics of the fragments and determination of the carbohydrate substituents of galacturonic acid. *Carbohydrate Research*, 328:539–547, 2000.

[78] Ranee A. Stile, Thomas A. Barber, David G. Castner, and Kevin E. Healy. Sequential robust design methodology and x-ray photoelectron spectroscopy to analyze the grafting of hyaluronic acid to glass substrates. *J. Biomed. Mater. Res. A*, 61:391–398, 2002.

[79] John F. Moulder, William E. Stickle, Peter E. Sobol, and Kenneth D. Bomben. *Handbook of X-ray Photoelectron Spectroscopy: A Reference Book of Standard Spectra for Identification and Interpretation of XPS Data.* Perkin-Ellmer-Corp., 1992.

[80] Charles D. Wagner, Alexander V. Naumkin, Anna Kraut-Vass, Juanita W. Allison, Cedric J. Powell, and John R. Rumble Jr. *NIST X-ray Photoelectron Spectroscopy Database.* National Institute of Standards and Technology (NIST), http://srdata.nist.gov/xps/.

[81] *The ExPASy (Expert Protein Analysis System) proteomics server of the Swiss Institute of Bioinformatics (SIB).* http://www.expasy.ch/.

[82] Kevin L. Prime and George M. Whitesides. Adsorption of proteins onto surfaces containing end-attached oligo( ethylene oxide): A model system using self-assembled monolayers. *J. Am. Chem. Soc.*, 115:10714–10721, 1993.

[83] Sascha Herrwerth, Wolfgang Eck, Sven Reinhardt, and Michael Grunze. Factors that determine the protein resistance of oligoether self-assembled monolayers - internal hydrophilicity, terminal hydrophilicity, and lateral packing density. *J. Am. Chem. Soc.*, 125:9359–9366, 2003.

[84] Kester, Duedall, Connors, and Pytkowicz. Artificial seawater, wikipedia. *http://en.wikipedia.org/wiki/Artificial_seawater.*

[85] Yapeng Fang, Saphwan Al-Assaf, Glyn O. Phillips, Katsuyoshi Nishinari, Takahiro Funami, Peter A. Williams, and Liangbin Li. Multiple steps and critical behaviors of the binding of calcium to alginate. *J. Phys. Chem. B*, 111:2456–2462, 2007.

[86] Isabelle Braccini and Serge Perez. Molecular basis of $Ca^{2+}$-induced gelation in alginates and pectins: The egg-box model revisited. *Biomacromolecules*, 2:1089–1096, 2001.

[87] Ivan Donati, Synnove Holtan, Yrr A. Morch, Massimiliano Borgogna, Mariella Dentini, and Gudmund Skjak-Braek. New hypothesis on the role of alternating sequences in calcium-alginate gels. *Biomacromolecules*, 6:1031–1040, 2005.

[88] A. P. Haag. *Mechanical properties of bacterial exopolymeric adhesives and theri commercial development. In: Biological Adhesives.* Springer: Berlin, 2006.

[89] Alexis J. de Kerchove and Menachem Elimelech. Calcium and magnesium cations enhance the adhesion of motile and nonmotile pseudomonas aeruginosa on alginate films. *Langmuir*, 2008.

[90] Anthony S. Clare, Ronald F. Thomas, and Daniel Rittschof. Evidence for the involvement of cyclic amp in the pheromonal modulation of barnacle settlement. *J. Exp. Biol.*, 198:655–664, 1995.

[91] Hishashi Yamamoto, Akiko Tachibana, Wakana Saikawa, Manami Nagano, Kiyotaka Matsumura, and Nobuhiro Fusetani. Effects of calmodulin inhibitors on cyprid larvae of the barnacle, balanus amphitrite. *J. Exp. Zool*, 280:8–17, 1998.

[92] Alexis J. de Kerchove and Menachem Elimelech. Formation of polysaccharide gel layers in the presence of ca2+ and k+ ions: Measurements and mechanisms. *Biomacromolecules*, 8:113–121, 2007.

[93] M. Wloka, H. Rehage, H.-C. Flemming, and J. Wingender. Rheological properties of viscoelastic biofilm extracellular polymeric substances and comparison to the behavior of calcium alginate gels. *Colloid Polym Sci*, 282:1067–1076, 2004.

[94] Gero Decher and Joseph B. Schlenoff, editors. *Multilayer Thin Films: Sequential Assembly of Nanocomposite Materials.* WILEY-VCH, 2003.

[95] Donald L. Elbert, Curtis B. Herbert, and Jeffrey A. Hubbell. Thin polymer layers formed by polyelectrolyte multilayer techniques on biological surfaces. *Langmuir*, 15:5355–5362, 1999.

[96] Sung Yun Yang and Michael F. Rubner. Micropatterning of polymer thin films with ph-sensitive and cross-linkable hydrogen-bonded polyelectrolyte multilayers. *J. Am. Chem. Soc.*, 124:2100–2101, 2002.

[97] Jian Ji, Jinhong Fu, and Jicong Shen. Fabrication of a superhydrophobic surface from the amplified exponential growth of a multilayer. *Adv. Mater.*, 18:1441–1444, 2006.

[98] Michael T.Thompson, Michael C.Berg, Irene S.Tobias, Michael F.Rubner, and Krystyn J.Van Vliet. Tuning compliance of nanoscale polyelectrolyte multilayers to modulate cell adhesion. *Biomaterials*, 26:6836–6845, 2005.

[99] Yanqing An, Miao Chen, Qunji Xue, and Weimin Liu. Preparation and self-assembly of carboxylic acid-functionalized silica. *Journal of Colloid and Interface Science*, 311:507–513, 2007.

[100] C. Picart, Ph. Lavalle, P. Hubert, F. J. G. Cuisinier, G. Decher, P. Schaaf, and J.-C. Voegel. Buildup mechanism for poly(l-lysine)/hyaluronic acid films onto a solid surface. *Langmuir*, 17:7414–7424, 2001.

[101] Ludovic Richert, Philippe Lavalle, Elisabeth Payan, Xiao Zheng Shu, Glenn D. Prestwich andJean Francois Stoltz, Pierre Schaaf, Jean-Claude Voegel, and Catherine Picart. Layer by layer buildup of polysaccharide films: Physical chemistry and cellular adhesion aspects. *Langmuir*, 20:448–458, 2004.

[102] Jeeyoung Choi and Michael F. Rubner. Influence of the degree of ionization on weak polyelectrolyte multilayer assembly. *Macromolecules*, 38:116–124, 2005.

[103] James F. Schumacher, Nick Aldred, Maureen E. Callow, John A. Finlay, James A. Callow, Anthony S. Clare, and Anthony B. Brennan. Species-specific engineered antifouling topographies: correlations between the settlement of algal zoospores and barnacle cyprids. *Biofouling*, 23:307–317, 2007.

[104] Dirk Schwendel, Reiner Dahint, Sascha Herrwerth, Matthias Schloerholz, Wolfgang Eck, and Michael Grunze. Temperature dependence of the protein resistance of poly- and oligo(ethylene glycol)-terminated alkanethiolate monolayers. *Langmuir*, 17:5717–5720, 2001.

[105] John A. Finlay, Sitaraman Krishnan, Maureen E. Callow, James A. Callow, Rong Dong, Nicola Asgill, Kaiming Wong, Edward J. Kramer, and Christopher K. Ober. Settlement of ulwa zoospores on patterned fluorinated and pegylated monolayer surfaces. *Langmuir*, 24:503–510, 2008.

[106] Soeren Schilp. *PhD Thesis (In Preparation)*. PhD thesis, Ruprecht-Karls Universitaet Heidelberg, 2008/2009.

[107] Maureen E. Callow, Alice R. Jennings, A. B. Brennan, C. E. Seegert, Amy Gibson, Leslie Wilson, A. Feinberg, R. Baney, and J. A. Callow. Microtopographic cues for settlement of zoospores of the green fouling alga enteromorpha. *Biofouling*, 18:237–245, 2002.

[108] A.J. Scardino, E. Harvey, and R. de Nys. Testing attachment point theory: diatom attachment on microtextured polyimide biomimics. *Biofouling*, 22:55–60, 2006.

[109] A. S. Clare and J. A. Nott. Scanning electron microscopy of the fourth antennular segment of balanus amphitrite. *J Mar Bio Assoc UK*, 74:967–970, 1994.

[110] H. Glenner and J. T. Hoeg. Scanning electron microscopy of cypris larvae of balanus amphitrite (cirripedia: Thoracica: Balanomorpha). *J Crustacean Biol*, 15:523–536, 1995.

[111] Larry D. Unsworth, Heather Sheardown, and John L. Brash. Protein resistance of surfaces prepared by sorption of end-thiolated poly(ethylene glycol) to gold: Effect of surface chain density. *Langmuir*, 21:1036–1041, 2005.

[112] Alexis J. de Kerchove and Menachem Elimelech. Impact of alginate conditioning film on deposition kinetics of motile and nonmotile pseudomonas aeruginosa strains. *Appl. Environ. Microbiol*, 73:5227–5234, 2007.

# Acknowledgment

After the four years intensive and fascinating work on this PhD thesis, I would like to express my great gratitude to the people who have offered me a lot help in many ways.

First of all I would like to thank Prof. Dr. Michael Grunze for offering me the chance to do this research work in his group as a PhD student and his supervision of my study and work during the four years. Thanks to Prof. Dr. Motomu Tanaka for being the referee of my thesis.

Special thanks to my supervisor Dr. Axel Rosenhahn. I am deeply grateful for his steady and continuous support throughout the course of this work. His constructive suggestions and discussions help me a lot.

Thanks to Prof. James Callow from the University of Birmingham for organizing the AMBIO project. My PhD work is mainly supported by this project and I have learned a lot of interesting and useful knowledge through the collaborations with the other partners in this project. Many thanks to the partners who made the biological evaluations for the surfaces that I prepared.

During the course of my PhD work, I have got a lot of invaluable help from the nice colleagues in our group. Many thanks to Dr. Mikhail Zharnikov, Günter Meinusch, Peter Jeschka and Reinhold Jehle. Without their amazing work, our old XPS machine MAX200 can never work so well. Thanks to Florian Staier for taking care of the vaccum system of MAX200 and his super negotiation in buying the vacuum oven. Thanks to Dr. Patrick Kölsch for reparing the ellipsometer and constructing the instrument for contact angle measurements. Thanks to Dr. Alexander Küller and Sören Schilp for taking good care of the chemistry lab and the SEM instrument. Thanks to Christof Christophis for designing the glass holder for spray coating, which greatly improves the preparation efficiency. Thanks to Albert Georg for the Si-wafer supply.

I am also grateful for the help from Frank Leisten (University of Hannover) for the AFM measurements and Patrick Horn (Otto-Meyerhof-Center, Heidelberg) for the cell adhesion test. Sincerely thanks to Prof. Dr. Jian Ji and Dr. Jinhong Fu (Zhejiang University, China) for giving us the idea in the field of polyelectrolyte

multilayers.

Matthias Heydt introdued the JabRef to me and Dr. Ruth Barth introduced LaTeX to me. Both tools work very well in organizing my literature and constructing the text of my thesis. In the final phase of my thesis writing, Florian Wode, Sebastian Weisse, Dominique Verreault and Dr. Ruth Barth did a wonderful job in the proof-reading of my thesis and Christina Leinweber gave me a big help in the German version of the abstract, die Zusammenfassung. I am greatly grateful to them.

Some former colleagues gave me a great help in the beginning of my PhD work. Special thanks to Dr. Svetlana Stoycheva and Dr. Jacques Blümmel for the introduction of the XPS instrumant MAX200 and Dr. Jörg Fick and Dr. Marco Maccarini for the introduction of the ellipsometer.

Besides the persons mentioned above, I would like to say thanks to Dr. Reiner Dahint, Dr. Martina Schürmann, Fanny Liu and many other current and former colleagues. The period in this group is not only filled experiments, spectra and scientific discussions, but also a pleasant period with plenty of wonderful cake-times, BBQ-times and ice-times and a lot of fun.

Finally, I dedicate my deepest gratitude to my parents and my sister who always stand by my side.